LOW COST PRINTED, FLEXIBLE, AND ENERGY AUTONOMOUS VAN-ATTA AND CARBON-NANOTUBES-BASED MM-WAVE RFID GAS SENSORS FOR ULTRA-LONG-RANGE UBIQUITOUS IOT AND 5G IMPLEMENTATIONS

A Dissertation
Presented to
The Academic Faculty

By

Jimmy G.D. Hester

In Partial Fulfillment
of the Requirements for the Degree
Doctor of Philosophy in the
School of Electrical and Computer Engineering

Georgia Institute of Technology

August 2019

LOW COST PRINTED, FLEXIBLE, AND ENERGY AUTONOMOUS VAN-ATTA AND CARBON-NANOTUBES-BASED MM-WAVE RFID GAS SENSORS FOR ULTRA-LONG-RANGE UBIQUITOUS IOT AND 5G IMPLEMENTATIONS

Approved by:

Dr. Manos M. Tentzeris, Advisor
School of Electrical and Computer Engineering
Georgia Institute of Technology

Dr. Andrew F. Peterson
School of Electrical and Computer Engineering
Georgia Institute of Technology

Dr. Gregory D. Durgin
School of Electrical and Computer Engineering
Georgia Institute of Technology

Dr. Herve Aubert
Micro and Nanosystems for Wireless Communication group
Laboratory for Analysis and Architecture of Systems

Dr. Suresh K. Sitaraman
School of Mechanical Engineering
Georgia Institute of Technology

Date Approved: April 22, 2019

We're blind to our blindness. We have very little idea of how little we know. We're not designed to know how little we know

Daniel Kahneman

To my parents, Bob and Kiki, whose total, unconditional, and unwavering love and support has been the stable foundation upon which to build my life, happiness, and accomplishments

ACKNOWLEDGEMENTS

I would, first, like to thank Prof. Manos Tentzeris for his friendship, his advice, and his mentorship. Manos works tirelessly to provide his students with the support and the opportunities we need to grow humanly and professionally. His trust in his students, second to none, has given me the freedom to pursue the research described in this thesis and to drive its direction and scope, while spending some of the most transformative, rich, and happy years of my life. The list of people deserving of an acknowledgement no doubt extends further than this page can fit and that the reliability of my memory would allow me to list without fault. Connections in life are often characterized and memorized through shared experiences and I will, therefore, like to acknowledge accordingly. If you understand the "Sent from my Iphone" pleasantry, or Charles' failed Apollo 13 joke, if you know and love Lolo's yogurt cake, if Ellie and Don hold a special place in your heart, or (more importantly) if Pingu is your favourite animal, then I want to acknowledge you and dedicate this work to you.

TABLE OF CONTENTS

LIST OF TABLES

LIST OF FIGURES

LIST OF SYMBOLS AND ABBREVIATIONS

2DFFT	2 Dimensional Fast Fourier Transform
AMS	Austria MicroSystems
AMT	Additive Manufacturing technologies
AoA	Angle of Arrival
BLE	Bluetooth Low-Energy
CDF	Cumulative Distribution Function
CNT	Carbon NanoTubes
CWA	Chemical Warfare Agent
DGPS	Differential Global Positioning System
DMF	Dimethylformamide
DMMP	Dimethyl methylphosphonate
DMSO	dimethyl sulfoxide
EIRP	Equivalent Isotropic Radiated Power
FET	Field-Effect Transistor
FFT	Fast Fourier Transform
FMCW	Frequency-Modulated Continuous Wave
FT	Fourier Transform
FWHM	Full With at Half Maximum
GaAs	Gallium Arsernide
GNP	Gold NanoParticles
GO	Graphene Oxide

HFA	HydroFluoro Alcohol
HPBW	Half-Power BandWidth
IFFT	Inverse Fast Fourier Transform
IoT	Internet of Things
LO	Local Oscillator
MIMO	Multiple-In Multiple-Out
PCB	Printed Circuit Board
PEDOT:PSS	poly(3,4-ethylenedioxythiophene) polystyrene sulfonate
PET	PolyEthylene Terephtalate
QCM	Quartz Crystal Microbalance
QPSK	Quadrature Phase Shift Keying
RCS	Radar Cross Section
RF	Radio Frequency
RFID	Radio Frequency IDentification
rGO	reduced Graphene Oxide
RH	Relative Humidity
RTLS	Real-Time Localization System
RX	Receiving
SAW	Surface Acoustic Wave
SNR	Signal to Noise Ratio
SOTA	State Of The Art
STFT	Short-Time Fourier Transform
SWCNT	Single-Wall Carbon NanoTubes
TX	Transmitting
UWB	Ultra-Wide Band
WISP	Wireless Identification and Sensing Platform

SUMMARY

Has the concept of "smart wall" or "smart surface" ever come through your mind? That is unlikely. Indeed, our interactions with the digital world—the universe predominantly stored and crated by data centers, connected through the internet—is generally mediated by discrete, dedicated, and recognizable components: your phone, your laptop, your smartwatch, or even your TV. This state is not the product of a lack of interest, need, or imagination. Indeed, the concept of "digital twin"—the virtual alter ego of a physical object—has started to make its way into Internet-of-Things-powered products and services. Rather, it is the consequence of hardware's inability to keep up with the exponentially-increasing demands and capabilities of software. The work presented in this thesis presents significant hardware developments, on the path leading towards the ubiquitous presence of intelligence, and the permeation of the physical into the digital. More specifically, the work reported in this document describes the creation of an approach that enables the addition of intelligence unto any surface, for the low-cost, real-time, and ubiquitous sensing of chemical agents. This outcome is the product of reported advances enabling the design and demonstration of fully-printed skin-like devices that can be precisely located and can fully-autonomously sense and transmit, at long range, in real time, part of the make-up of their chemical environments. These results were achieved through the combination of additive-manufacturing tools and technologies, nanomaterials-based sensing, and ultra-low-power mm-wave ($24\,\mathrm{GHz}$ to $28\,\mathrm{GHz}$) retrodirective communications schemes and signal processing. Notably, the work describes (to our knowledge), the longest-ranging chipless RFIDs and unamplified monostatic backscatter RFIDs–at the time of their publication—and the first ever fully-inkjet-printed organophosphorus nerve agent in the literature.

CHAPTER 1
INTRODUCTION AND BACKGROUND

1.1 Motivations

This thesis presents work driven by the development of a new class of ambitious and disruptive technologies for ubiquitous sensing applications for homeland security-enhancing airborne-chemicals hazard alert systems. Ubiquity of the required applications very quickly rules out any physically-connected systems (a.k.a. "wired) from the onset.

While it is possible to implement wireless optical sensing systems using passive infrared (IR) imaging [1], remote standoff detection [2] and different spectrophotometric approaches [3], these suffer from either very low sensitivities or ranges or are restrained to detecting gas levels in areas confined within the narrow beam of a laser, at the end of which a reflector needs to be installed and are , in addition, quite expensive optical systems. These same limitations hold true for lower frequency (radar) systems [4]. For these reasons, solutions involving local sensing nodes offer the broadest and most promising perspectives in this context. While optical nodes are, in principle, applicable to such solutions, the greater maturity and lower cost of electrical systems motivates the use of electrical nodes for the applications at hand.

After this brief identification of the optimal system type, an identification of the of the ideal properties of such a system can be undertaken. The quintessential ubiquitous chemical sensing system needs to display the following characteristics:

- **Inconspicuousness:** Any dense constellation of sensing nodes could quickly become aesthetically and functionally invasive if not constituted of devices whose form factor and appearance allow them to readily blend into their environment.

- **Low cost per node:** The aforementioned technological solution would rely on the

assembly of thousands of nodes and therefore require a proportionally high capital investment for their acquisition and installation. In order to offer an affordable system, these per-device costs need to be kept as low as possible.

- **Energy autonomy:** It is necessary, in order to implement the ubiquitous detection of gases in spacious environments, to mount a significant (if not dominant) subset of the nodes in areas that are of difficult access. These operations involve time-consuming and life-threatening work which can contribute to high labor and liability costs which may often dwarf the acquisition cost of the installed nodes. While this may hardly be avoidable during initial set-up, the regular repetition of such operations for maintenance purposes over the life-span of the nodes can tremendously increase the lifetime cost of the system. The need for high nodes density further amplifies that issue. As a consequence, non-energy-autonomous devices which require regular battery-change maintenance operations are ill suited for such applications: energy autonomy needs to be achieved.

- **Real-time operation:** Extended delay times between the emergence of chemical threats, and their detection and communication to a central system by means of their wireless interface, could entirely nullify the benefits of its implementation. Systems with aggressive duty-cycles—generally used to limit their average power consumption—cannot therefore be adopted.

- **Long reading range:** As can be seen with the challenges generally associated with state-of-the-art passive RFID solutions, a short reading range–whether it is with reference to a base-station or the nearest dedicated reader–quickly translates to often unbearably high infrastructure costs. Naturally, such expenditures are amplified by the necessity to draw communications and power cables to each of the readers of the network, in addition to testing them individually after installation. Enabling a single reader—or a limited set of readers—to service large areas requiring coverage would

therefore provide a much more appealing and adequate technology.

- **Capability to detect nerve agents:** While this may appear as a self-evident requirement, the detection of chemical warfare agent (CWA) gases is a challenging but remarkably active field of academic and governmental research [5].

This last analysis oriented the selection of a specific set of approaches and technologies to achieve the targeted performance. These, respectively listed in the following, form the backbone of the work and, therefore, of this thesis:

- Implementation of thin, flexible electronics systems as nodes. Such device can now be fabricated using the capable and quickly-maturing tools of the modern printed electronics revolution, as will be expanded upon in section 1.2.

- Substrate can often constitute the highest contributor to the overall cost of a wireless system, especially if its antenna is built upon it. Adoption of the low-cost electronic substrates compatible with the tools used for flexible and hybrid electronics can therefore contribute to meeting the aforementioned stringent per-device cost constraints.

- Energy harvesting can be implemented from independent or simultaneous contributions from sources such as solar, RF, vibrations, and thermal gradients [6]. Nevertheless, with the notable exception of solar in high-lighting outdoor conditions, none of these sources provide large enough power densities to enable the powering of devices with average power consumption levels exceeding several tens of $\mu\mathrm{W}$. Major progress has been made within the last decades to bring the power of embedded micro-computing units down under these level. Nevertheless, active wireless transceivers still require power levels on the order of mW during communications and therefore cannot be used for real-time data transmission. Bluetooth Low Energy (BLE), which is the current reference for low power communication systems can provide average power consumption levels on the order of $100\,\mu\mathrm{W}$ with a low refresh

rate on the order of $0.5\,\mathrm{s}$ and at limited maximum ranges (less than $100\,\mathrm{m}$) due to the high bit rates of $1\,\mathrm{Mbps}$ adopted to allow short transmission times [7]. It, therefore, seems necessary for alternative, lower-power communications approaches to be adopted. In that respect, chipless schemes reign as the undisputed champions—with a power consumption equal to exactly zero—closely followed by physical backscatter approaches requiring an operating power south of $300\,\mathrm{nW}$ [8]. These were, therefore, adopted for this work.

- As we will see in section 1.4.3, the communications approaches selected following the considerations of the previous paragraph have, traditionally, displayed quite limited interrogation ranges. One of the main contributions of this work, as we will see, is to introduce systems and approaches which empower them with extended reading ranges.

- Form factor and cost specifications greatly bound the domain of applicable sensing technologies. However, in addition to allowing consistency of the required fabrication tools, printed thin-film gas sensors can answer all of these requirements. These reasons motivate their adoption and exploration in this work.

1.2 Additive manufacturing: a primer

Since the inception and widespread adoption of the circuit board since the middle of the 20$^{\text{th}}$ century, the general form of what is understood as a printed circuit board (commonly referred to as PCB) has not seen radical changes. Most human inhabitants of the earth, either through first-hand experience or via exposure to popular media would readily recognize the object of fig. 1.1 as a piece of electronics, and are likely never to directly encounter anything other than the characteristically green shades of the solder mask that coats the board's flame retardant (FR-4) yellow substrate. However, new fabrication trends are veering electronics technologies into directions that may, within a few decades, demote these

familiarly green PCBs as an artifact of an all but forgotten past.

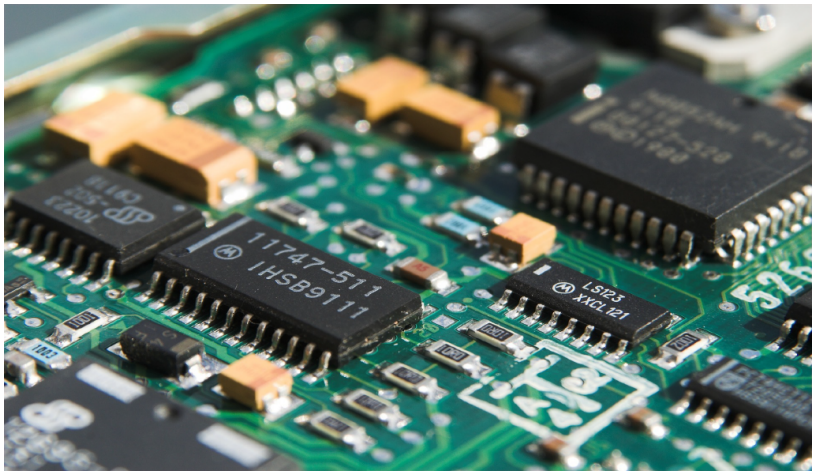

Figure 1.1: Image of a commercial PCB

Additive manufacturing technologies have risen during the last decades of the twentieth century, enabled by the radical new capabilities developed during the nanotechnology revolution, and are quickly rising in capabilities and technological maturity and readiness. These approaches offer a profoundly new way of developing, prototyping and producing electrical systems and components that can not only meet the remarkably dynamic economical and ecological standards of the modern world, but can also fundamentally transcend the common boundaries of electronics applications and integration.

1.2.1 An evolution in fabrication

As made self-evident by the term used to refer to them, additive manufacturing technologies (AMTs) are a subset of fabrication approaches that exclusively (or predominantly) rely on the addition of materials along the fabrication process. During the current standard electronics fabrication processes chain (shown in fig. 1.2), an entirely-copper-clad piece of substrate is etched to remove generally more than 80% of its cladding and leave behind the traces forming the conductive circuitry. In a later stage, an analogous process is applied for the characteristically-green solder mask layer, which is first thoroughly spread onto the surfaces of the PCB before its negative pattern is etched away. These etching and removing

steps are the cause for large material wastes, resulting in increased costs and the generation of large amounts of hazardous chemical wastes which are, ideally, properly removed and recycled.

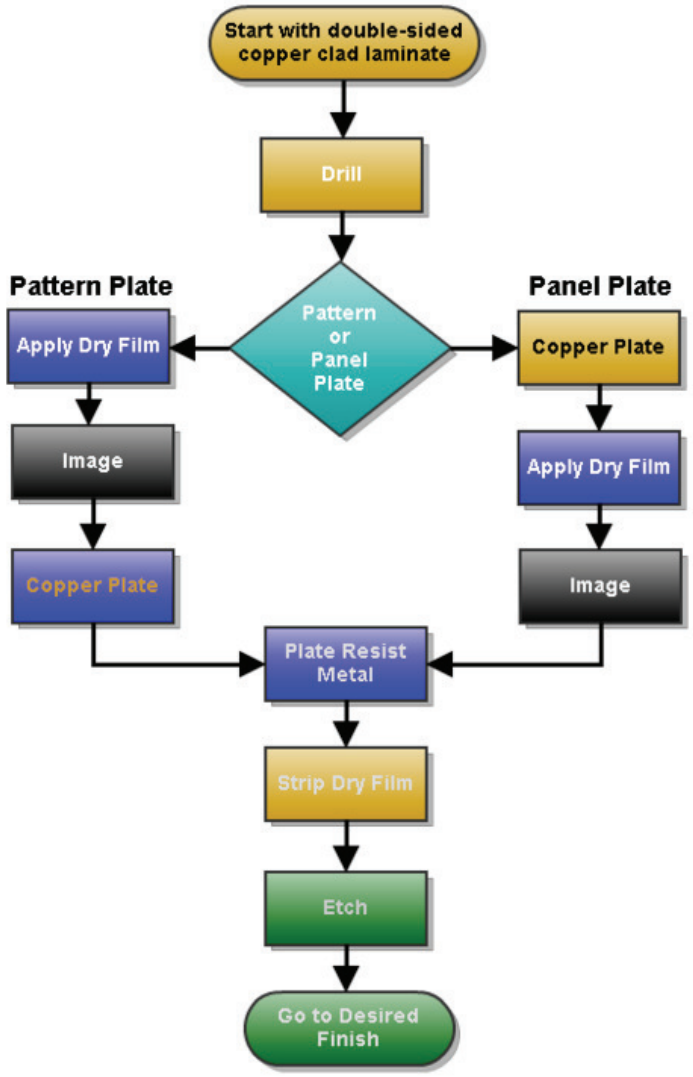

Figure 1.2: 2-layer PCB standard manufacturing process flow chart [9]

Additive manufacturing, on the other hand, focuses on the addition of materials and therefore does not necessitate the use of more materials than that to be deposited. Consequently, this class of approaches enables much more environmentally-friendly production and, in principle, much lower materials costs. A generic term such as AMTs naturally encompasses a wide range of technologies with varying specifications and operating prin-

Table 1.1: Additive manufacturing techniques compared [10]

Additive Technique	Materials	Features size (µm)	Benefits	Drawbacks	Commercial Examples
Material Extrusion	• Thermoplastics	100-1000	• Ultra low-cost • Good integration with other AM technologies • High volumetric deposition rate	• High surface roughness • Mediocre feature size • Anisotropic parts • Unknown material production standards	• Stratasys • 3D Systems • Ultimaker
Stereolithography	• Photopolymers	1-100	• Fine features size • Low surface roughness	• RF Lossy materials • Difficult to directly integrate with other technology • Expensive	• Materialise • 3D Systems
Material Jetting	• Photopolymers • Waxes • Binders	10-100	• Fine features size • Good surface roughness • Potential integration with inkjet metals	• RF Lossy materials • Poor integration with other AM technologies • Expensive	• Objet (Stratasys), • 3D Systems
Aerosol Jetting	• SNP inks • Photopolymer resins	10-100	• Fine features size • Low surface roughness • Multi-material	• Only thin layers • Low volumetric deposition rate • Poor integration with other AM technologies • Expensive	• Optomec
Inkjetting	• SNP inks • Photopolymer resins	10-100	• Low-cost • Fine feature size • Multi-material • Low surface roughness	• Only thin layers • Low volumetric deposition rate	• Dimatix (Fujifilm)
Syringe Pump	• SNP inks • Any other paste	100-1000	• Low-cost • Multi-material • Good integration with other AM technologies • High volumetric deposition rate	• Mediocre feature size	• nScrypt/Sciperio

ciples. In table 1.1 is listed a subset of the AMTs, including several of their differentiating characteristics.

It should be briefly noted that inkjet-printing stands out due to its combination of high resolution, low-cost, materials diversity, and direct file-to-print rapid prototyping capability

for the design, development, and fabrication of 2D devices on flexible substrates. As is shown in fig. 1.3, its PCB manufacturing process differs substantially from its standard counterpart—as shown in fig. 1.2—by its simplicity and, more importantly, by its lack of need for the environmentally-impacting chemical etching of material ; its process is completely additive.

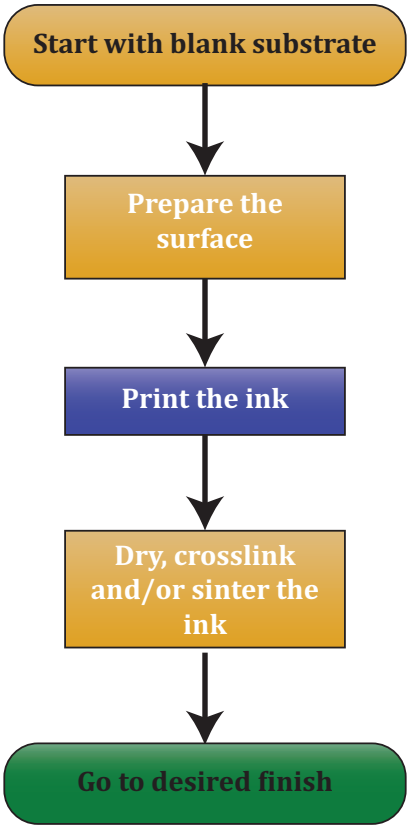

Figure 1.3: Inkjet-printed PCB manufacturing process flow chart

For these reasons, this manufacturing technology was selected for the work described in this thesis.

1.2.2 A leap in integration

In the previous section, I argued that additive manufacturing technologies (AMTs) allowed for reductions in the cost and environmental impact of the fabrication of electrical components and systems. Although important a development, AMTs offer much further-ranging

and unique properties. Indeed, printing AMTs are compatible with a far wider variety of substrates, that are wholly unusable with the chemically and thermally challenging procedures of conventional fabrication. By contrast AMTs offer conductor-depositing approaches that only require substrates to withstand sintering temperatures as low as $120\,^{\circ}\mathrm{C}$, and either be insoluble in water or in mild organic solvents. As a consequence, substrates as diverse as polyeyhylene (PET), Polystyrene (PS), paper, Polytetrafluoroethylene (PTFE), and even cork [11] have been demonstrated for use. This range extends the design trade-off space far beyond the boundaries currently constraining standard fabrication techniques, and allows the manufacturing of ultra-low-cost skin-like compact devices that can readily and inconspicuously be integrated onto surfaces and items, or into flexible pieces of clothing, for instance. The combined appeal of low cost and convenient sticker-like form factors have already been compelling enough in cost-driven markets such as that of passive radio frequency identification (RFID) tags to motivate and cause the rapid adoption of such manufacturing approaches as standard, as shown through the example of now-familiar rolls of RFID with printed antennas.

1.2.3 An electronics revolution

The semiconducting revolution initiated in the middle of the twentieth century has set the stage for the formation of the now $400B semiconductor industry, and developed the standards for the fabrication of active electronics integrated circuit (IC) devices and components. The fabrication of a standard IC generally starts with a rigid monocrystalline semiconductor wafer which is built upon by repeating a process consisting of its full coating using vapor-deposited thin material films followed by or preceded with the masking of a pattern using a lithographically-shaped photoresist, finally followed by etching. Again, in the same manner as with standard PCB production, substractive and quite pervasively waste generating steps are required.

AMTs are slowly creeping into the picture and starting to challenge the hegemony of

traditional approaches by enabling the fabrication of low-cost active electrical components. An area particularly receptive to the advantages of AMTs over standard manufacturing is solar elements manufacturing, where printed organic semiconductors-based photovoltaic elements are demonstrating power conversion efficiencies outclassing that of commercial amorphous silicon solar cells [12], with the added advantages of ultra-low-cost R2R manufacturing compatibility and flexible form factors. Further research on the reliability of such panels over extended periods of use is still required before widespread adoption can become possible.

The advent of printable displays is chasing capabilities similar to that driving the development of flexible photovoltaic devices. Indeed, in addition to the obvious appeal of low-cost and "green" manufacturing, new form factors are sought after for the facile and aubiquitous integration of bendable, foldable or moldable displays. Since Sony launched its eleven inch OLED-TV in 2007, organic light-emitting diodes have become extremely common for thin, flat TV displays and even have grown to be somewhat of a standard for displays in the smartphone industry. Although generally not printed nor flexible, these displays are their quick adoption has set the market and technological stages for the emergence of their printed counterparts. Indeed, companies such as FlexEnable have already started proposing commercial flexible and partially-printed AMOLED and OLCD displays for integration into wearable and automotive technologies, among many others.

In addition to the remarkable recent progress of photovoltaic roll-to-roll printable wall papers, impressive leaps in the complexity and capabilities of printed active systems are regularly reported and are even leading to the commercialization of devices whose birth can still tread the realms of science fiction for most. Thinfilm, a Norwegian company, is now commercializing *fully-printed* Near Field Communication (NFC) RFID tags that incorporate a memory, a logic interface, a $13.56\,\mathrm{MHz}$ rectifier and antenna combination, a segment display and temperature sensors, as shown on fig. 1.4.

The scientific literature now reports, as well, fully-printed inverters, ring oscillators,

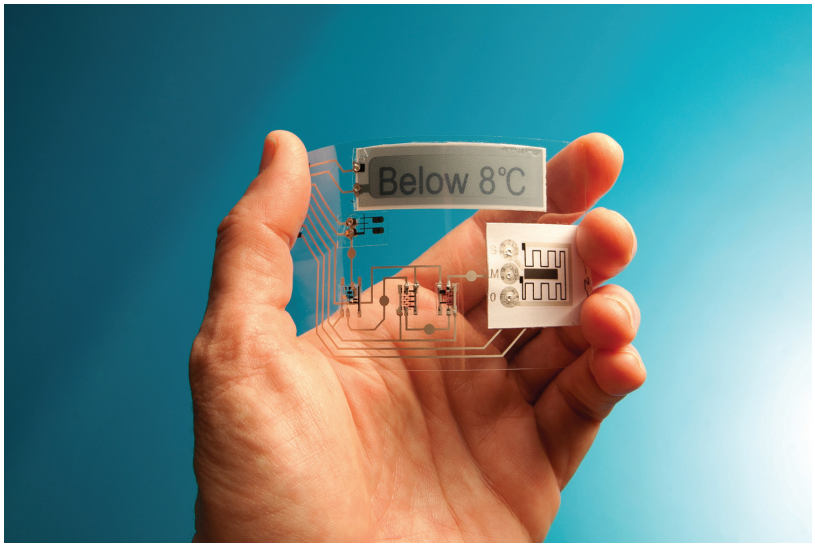

Figure 1.4: Image of a fully-printed tag sold by Thinfilm [13]

logic gates, frequency dividers, shift registers and decoders, amplifiers, digital to analog converters, and RFID systems [14].

I will now focus on inkjet printing, a particular additive manufacturing method that lies at the center of this thesis, and on the sub-area of printed and additively-manufactured radio frequency (RF) and mm-wave components and systems.

1.3 Inkjet-printing

As previously mentioned in section 1.2.1, inkjet printing is one of the many fabrication approaches that fall under the category of additive manufacturing technologies. As shown on fig. 1.5, it consist in the sequential deposition of consistently-sized droplets onto a substrate which is moving relative to the nozzle. The process can be executed in two main ways, qualified as continuous printing (CP) on the one hand—where the drops are constantly generated and caught or not by a gutter in order to individually select their deposition onto the substrate—or through a drop-on-demand approach in which the drops are only jetted over the areas where their deposition is required. This printing technology stands out for three main reasons:

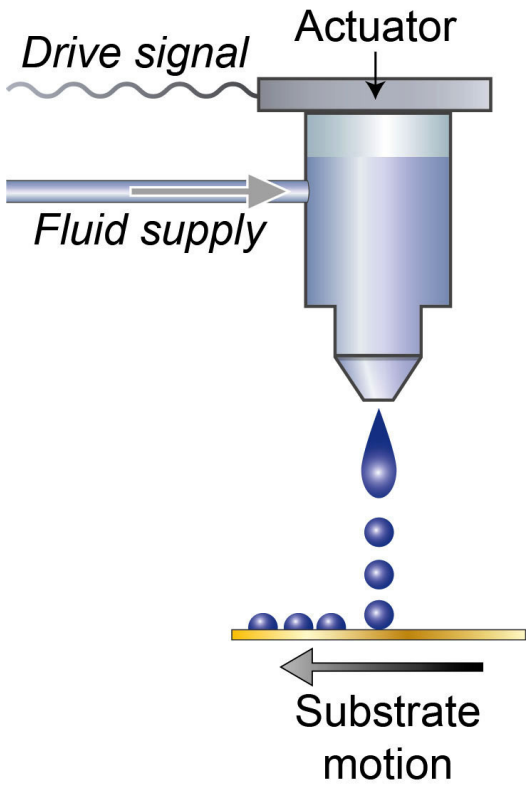

Figure 1.5: Schematic of the inkjet-printing process

- **Direct file-to-print approach:** Contrary to rather widespread techniques such as gravure and screen printings, inkjet does not require the design and fabrication of any intermediate hardware—a stencil or roll, for instance—in order to carry out the printing. A device goes directly from an abstract digital file to a concrete print. This makes inkjet, along with other technologies such as aerosol jet, stand out for its rapid prototyping ability.

- **Compatibility with an uncountable large variety of printable materials:** In order to deposit a material through inkjet-printing, this material only need be soluble or dispersable into a solvent. As a consequence, all materials that can be dissolved into a solution (such as salt, for instance), that can exist in liquid phase in conditions close to that of standard temperature and pressure, or which can be dispersed into a solvent–such as nanomaterials particles (carbon nanotubes, graphene and other 2D materials nanosheets, etc.)–can be deposited using that process.

- **Wide substrate compatibility:** With techniques such as gravure printing or screen printing, a direct contact takes place between a stencil or a roll and the substrate surface. With inkjet and aerosol printing, the ink is ejected from a nozzle and goes into free fall before hitting the substrate; no direct contact can occur between the printer and the substrate. These later techniques can therefore accommodate non-planar substrates for the fabrication of printed circuitry, within certain limitations. Indeed, once the inkjet-extruded drop hits the substrate, its drying is required to deposit the material carried by the solvent. In the case of sharply-slanted surfaces, an inkjet droplet might slide downwards before this deposition occurs. In that respect, aerosol-jet printing has recently been gaining traction due to its ability outperform inkjet-printing by ejecting $\mu\mathrm{m}$ sized droplets that dry virtually upon impact.

The auspicious picture of inkjet-printing that was just painted (or dare I say printed) needs to be somewhat counterbalanced with some mention of the main drawbacks of the technique. They are the following:

- **Slowness:** Unlike gravure and screen printing which are essentially parallel processes, inkjet is generally (although not necessarily) a sequential scheme, where the nozzles move above the substrate in a row-by-row fashion to deposit the ink. As a consequence, it is greatly outperformed in velocity by its aforementioned cousins. State of the art industrial systems like the Gross Sunday 3000 offset printer can reach speeds of $3000\,\mathrm{ft\,min^{-1}}$

- **Narrow range of acceptable ink properties:** In order to be properly jettable, an inkjet ink needs to have properties that fall within the printable region mapped on fig. 1.6 for varying values of the Reynolds (Re), Weber (We) and Ohnesorge (Oh) numbers, defined as a function of, ρ, the density of the , η, the dynamic viscosity, γ, the surface tension of the ink, v, the characteristic length, and a, the radius of the

droplet by the following relationships:

$$Re = \frac{v\rho a}{\eta} \tag{1.1}$$

$$We = \frac{v^2\rho a}{\gamma} \tag{1.2}$$

$$Oh = \frac{\sqrt{We}}{Re} = \frac{\eta}{\sqrt{\gamma\rho a}} \tag{1.3}$$

For a typical Fujifilm Dimatix DMP2800 printer, this translates to a required viscosity of $9\,\mathrm{cP}$ to $12\,\mathrm{cP}$ and $28\,\mathrm{dyn\,cm^{-1}}$ to $32\,\mathrm{dyn\,cm^{-1}}$.

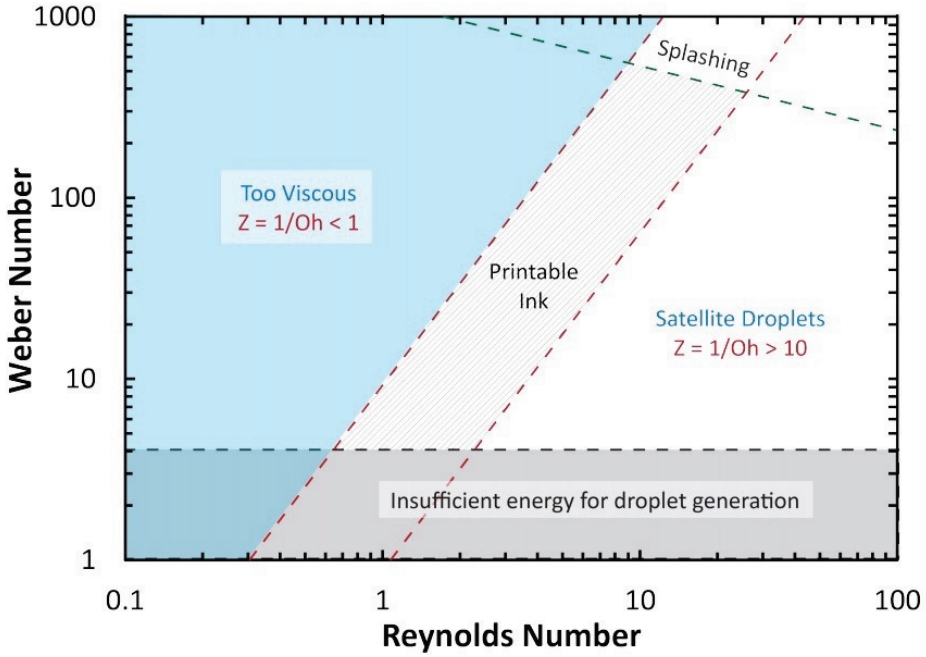

Figure 1.6: Mapping of the acceptable properties required for inkjet inks [15]

From an electronics prototyping point of view the relative strengths of inkjet-printing far outweigh its drawbacks, in the light of its rich materials versatility, its low cost, and its high patterning resolution on the order of $20\,\mu\mathrm{m}$ to $50\,\mu\mathrm{m}$. For these reasons, this tool was

adopted for the work described in this thesis.

1.4 Printed components for wireless sensing electronic systems

After setting the technological stage for the work described in this thesis, through the introduction of the emerging and revolutionary printed and flexible hybrid electronics industry and by the selection and characterization of the inkjet printing fabrication technology, this section paints the current state of the art of the printed components of the wireless gas sensing systems whose development constitute the basis for the work synthesized in this thesis.

1.4.1 Printed chemical sensors

This section will focus on giving an overview of the state of the art in printed or printable sensor technologies, used for the detection and concentration tracking of a range of chemical agents of significant practical importance. Due to the broad extent of their current and potential application contexts in food and perishables monitoring, occupational hazard detection, and environmental surveillance, the development of chemical and biological sensors holds a particular importance in sensor technology research. Two major types of sensors can be distinguished: gas, and liquid-phase sensors. This chapter will only cover electrical components-based technologies that are compatible with flexible substrate. Therefore, optical characterization techniques which require complex and power-hungry interfacing electronics, or piezoelectric-material-based techniques, such as quartz crystal microbalance (QCM) and surface acoustic waves (SAW) methods, that require the use of non-flexible piezoelectric substrates will not be covered. Flexible-substrate-compatible sensors usually function according to two main principles, whose implementations generally are those shown in fig. 1.7.

- **Amperometric and potentiometric sensors** fundamentally rely on the current induced by an ongoing chemical reaction with the targeted analyte [16], or the mea-

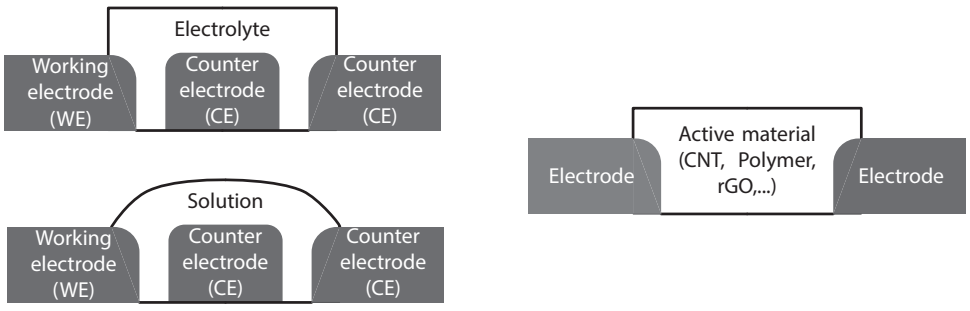

(a) (b)

Figure 1.7: Cross section structure of typical (a) structural or solution electrolyte potentiometric/amperometric and (b) resistormetric sensors

sured equilibrium potential of an electrochemical cell [17], respectively. These sensors, whose general structure is shown in fig. 1.7a, already have a widespread use in a number of industries ; many glucose or pH sensors in the market, as well as the majority of automotive exhaust fumes analysis equipment are based on the use of such technologies. Both techniques rely fundamentally on the electrical behavior of an electrochemical cell and therefore require the use of electrolytes. This characteristic has major consequences on these sensors' ease of fabrication for low cost printed flexible sensor systems, for gas or liquid-phase detection. Such implications will be expanded upon in the next subsection.

- **Resistometric/conductometric/impedometric** sensors use a measured change of resistivity (or complex impedance) of the sensing component, as a consequence of the exposure to the gas analyte. While some amperometric sensors are often considered resistometric, as the measurement of a current, at fixed bias voltage, can be considered to be equivalent to a change in conductivity, the underlying mechanism is quite different. Indeed, the observed change in conductivity of an impedometric sensor is the product of variations of intrinsic physical properties (electronic energy levels, Schottky barrier heights [18], intrinsic capacitance [19, 20]) of the conducting, di-

electric and semiconducting materials and/or structures ; not that of carriers added to the system as a product of redox chemical reactions. A major consequence of this, of great interest here, is the lack of requirement for the use of electrolytic materials. These components generally have an extremely simple structure that is comprised of two conductor (generally metal) electrodes connected by an active-material, as shown in fig. 1.7b. Impedometric (mostly resistometric) sensors have a rather long history, with the first proof-of-concept demonstrations dating back to Bell labs in the 1950s [21]. However, the modern rise of nanotechnologies has breathed a new life into this sensor technology, especially for their use in low cost flexible printed systems, for three main reasons:

- The fundamental importance of a high active material surface area for enhanced performance was quickly recognized. This was later implemented—not only through the use of semiconductor nano-crystallites or nano-wires with, indeed, significant performance improvement [22]—but mostly with semiconducting and conducting 2D nanomaterials and conjugated molecules, which gave rise to a range of new implementations with extremely high surface area and unprecedented performance.
- New nanomaterials, such as graphene, carbon nanotubes, and conjugated molecules and polymers can very easily be printed on virtually any surfaces, without requiring any subsequent high temperature sintering.
- These new materials greatly expanded the chemical and physical diversity of the active-gas-sensing-materials spectrum, allowing for the effective detection of a greater range of analytes.

Another important class of this broad impedometric sensor family is that of permittivity-tunable (or, conceivably, permeability-tunable) RF structures, where the entire RF device acts as both the sensor and the tag, taking advantage of electromagnetic prin-

ciples [23]. For example, polyimide, used as a RF substrate, can provide an easily detectable resonant frequency detuning, thanks to its relative-humidity-dependent dielectric permittivity.

Both of the above technologies have been implemented for the (sometimes fully-printed) fabrication of a broad range of chemical sensors. Gas-phase and liquid-phase sensors will be discussed separately, as they provide different opportunities and challenges, and are generally results of the efforts of distinct research communities.

Gas sensors

Gas sensors have the ability to track the concentration and/or detect the presence of specific gas-phase chemical agents present in their environment. Solid-state potentiometric and amperometeric gas sensors, have a number of properties that make them of challenging use for the purposes described in this chapter. Indeed, these types of structures require electrolytes for gas sensing, which can either be in solution or solid form. Solution or gel electrolytes are quite challenging from a printing and packaging perspective, while most of solid electrolytes require the use of highly crystalline films which, even though their material can be deposited using printing methods [24], require firing at temperatures in excess of $1000\,^{\circ}\mathrm{C}$, and generally require high operating temperatures, above $150\,^{\circ}\mathrm{C}$; such heating (unless in a high-temperature environment) would increase the power consumption of these sensors to unacceptably high levels for the configurations considered in the present context. Nevertheless, viable printable electrolytic materials are slowly coming into play, with efforts reporting the use of carefully-packaged ionic gels or liquids [25], as well as plain or doped polymer matrices [26], which can be printed even on flexible substrates [27]. However, not much work has yet been done on the integration of such gas sensors into printed far-field wireless systems [28].

Resistometric and impedometric sensors, whose fabrication is not constrained by the necessary use of electrolytic materials, have, on the other hand, been implemented (and

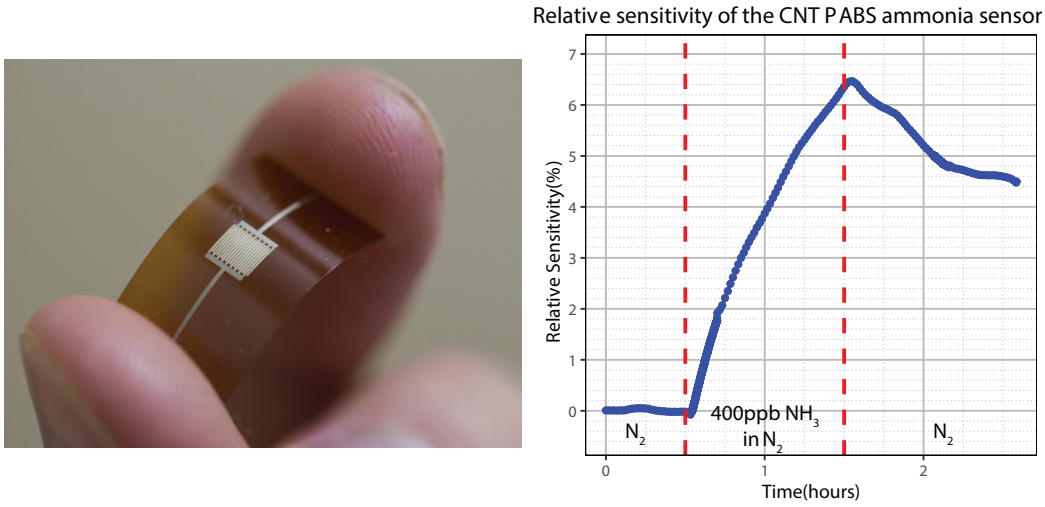

(a) (b)

Figure 1.8: (a) Picture of a fully inkjet-printed CNT-PABS-based resistometric flexible ammonia sensor and (b) its response to exposure to 400 ppb of ammonia

characterized at DC [29] and RF [30]) in many occasions as fully-printable flexible vapor sensors, usable at ambient temperatures. Indeed, the properties previously mentioned have enabled the design and fabrication of high performance sensors for a wide range of gases, a subset of which are listed in table 1.2. An example of a SWCNT-PABS ultra-sensitive ammonia sensor, fully inkjet-printed on polyimide substrate, and its response to 400 ppb of ammonia, is shown in fig. 1.8.

The sensors listed in table 1.2 were mostly manufactured with different sensing materials, which endowed each one of these devices with particularly high sensitivity to their associated analyte. Nevertheless most of those sensors are (to a certain degree) sensitive to many other chemical compounds. This lack of chemical selectivity is one the main challenges for this technology. Nevertheless, such a problem can be addressed by assembling several of these different sensors into an array [40, 41, 42], and taking advantage of their collective response to the same chemical excitation ; a properly chosen set of sensors can then provide a response that can be uniquely associated to a given chemical environment (in concentration and composition).

Table 1.2: List of notable resistometric gas sensors, and their sensing materials and performance

Ref.	Analyte	Lowest detected concentration and associated sensitivity	Sensing materials
[31]	H_2	30% at 3 ppm	SiNW/Pd
[32]	CO_2	10% at 10 ppm	Graphene
[33]	NH_3	60% at 10 ppb	PANI-PSS NP
[34]	NO_2	0.5% at 500 ppb	rGO
[35]	NO_2	5% at 100 ppt	CNT-PEI
[36]	CO	2.2% at 10 ppm	MWCNT
[37]	CH_4	1% at 6 ppm	SWCNT-Pd
[38]	DMMP	150% at 1 ppb	SWCNT
[39]	Nitrotoluene	1.5% at 54 ppm	SWCNT

Liquid-phase sensors

The conditions of liquid phase sensing are quite different, when considering electrochemical sensors. Indeed, the presence of a liquid bridging the electrodes of the sensor cell removes the necessary use of printable room-temperature-operating electrolytic bridge. As a consequence, the sensor structure is effectively reduced to mere electrodes, which can then be functionalized in order to sense the targeted analytes. Given the additional appeal and the low cost of printing methods, it is therefore no surprise that the literature abounds of reports of such sensors [43]. In addition, the range of demonstrated detectable analytes is extensive, both in the areas of biological [44] and chemical sensing. The area of wireless liquid-phase sensing nodes has not drawn as much attention as gas sensing applications have. One of the reasons for this is the relative incompatibility between liquids (especially water) and RF structures. Indeed, a radiating structure immersed in water, over the frequency range compatible with maximum practical dimensions for long-range-radiating wireless sensor nodes, is electromagnetically isolated from its environment. Nevertheless, interfacial configurations (such as floating nodes) or and in-air moisture absorbent devices could very well be considered.

1.4.2 RF flexible and printed electronics

This section explores the state of the art, recent advances and challenges associated with the printing of flexible RF electronics systems. Of course such devices would likely include sensors, logic, passives, RF passive elements such as antennas, and RF non-linear components such as switches or amplifiers. Here, I will singularly focus on the active ans passive RF components of such systems and analyze them from an additive manufacturing standpoint.

The printing of passive RF, mm-wave, and even THz components has been demonstrated for longer than a decade [45]. Using the alternative printing dielectric and metal-nanoparticle-based conductive layers, these can take the shape of single layer dipoles (for RFID applications, for instance [46]), as well as multi-layers antenna arrays [47], high-frequency-compatible inkjet [48] or 3D [49] printed lumped components with self-resonant frequencies in excess of $4\,\mathrm{GHz}$, or even substrate-integrated waveguide (SIW) structures [50]. Yet, much still has to be explored from a materials standpoint, in order to allow the birth of low-cost, reliable, resilient and high-performance devices. With this goal in mind, research on the optimization of the RF electrical properties (conductivity, loss tangent, etc,) of printed materials is underway [51].

The field of printed active devices, by contrast, is at a far lower level of maturity but is rapidly gaining speed. Indeed, printed active RF electronic require, of course, the deposition of high-performance semiconducting electrical films. Additive-manufacturing-compatible semiconducting materials include organic semiconductors such as P3BM and PBTTT, but these are generally deemed unsuitable for RF applications due to their limited charge-carrier mobilities (less than $10\,\mathrm{cm^2\,V^{-1}\,s^{-1}}$ [52]). On the other hand, carbon-based nanomaterials such as graphene and carbon nanotubes (CNT) offer a much greater appeal due to their incredibly-high measured mobilities [53] of $200\,000\,\mathrm{cm^2\,V^{-1}\,s^{-1}}$ [54] and $50\,000\,\mathrm{cm^2\,V^{-1}\,s^{-1}}$ [55], respectively. However, once in printed film form and interfaced with printed electrodes, these materials suffer from orders of magnitude degradations in

their carrier mobilities ($90\,\mathrm{cm^2\,V^{-1}\,s^{-1}}$ [56] and $9\,\mathrm{cm^2\,V^{-1}\,s^{-1}}$ [57], respectively) due to, on the one hand, the topology of the printed channels that are constituted of an aggregate of individual nanoparticles whose interfacing breaks the crystalline symmetry responsible for the originally remarkable mobility values of these materials, and on the other hand by carrier injection issues due to high contact resistance between the printed electrodes and the semiconducting film [58]. These limitations, along with their associated trade-offs, are currently limiting the implementation of oscillators for operation at frequencies grater than $800\,\mathrm{kHz}$ [59]. Nevertheless, recent progress has opened a path towards the emergence of fully-printed GHz-compatible carbon-nanotubes-based RF switches [60]. While it seems possible for printed RF transistors to be developed within the upcoming decade, low-frequency-compatible printed circuitry is already implemented in products and a pathway for the commercialization of printed RF switches within the next decade seems to be visible in the distance. These last components are sufficient for the assembly and design of fully-printed backscatter front-ends, but not for their active counterparts which systematically require a RF high-speed local oscillator.

This fairly detailed review of the state-of-the-art of printed RF active electronics may seem somewhat out of place given the specific topic of this thesis. However, its goal is to make the following point: Currently non-"chipless" fully-printed wireless electronics systems exclusively rely on backscatter communications schemes, and will likely continue to do so (even for much higher frequencies) in the foreseeable future.

1.4.3 Printed wireless devices and systems for ubiquitous sensing

As demonstrated in section 1.4.2, the current state of the art in flexible printed electronics provides a strong motivation to direct our focus exclusively towards backscatter-communications-enabled or linear wireless systems. These are also known as passive and semi-passive RFIDs, and chipless RFIDs, respectively.

Additional features of these communications approaches contribute towards building

an even stronger case for them. Indeed, backscatter schemes (first proposed by Stockman [61]) are well known for their ability to operate using orders-of-magnitude less power than their active transceiver counterparts such as current IoT BLE, ZigBee, or LoRa transceivers. For this reason, backscatter tags can be powered by only using power generated by a nearby readers—these are the "passive" and most common type—or can be powered using energy harvested in their environment. This approach is thereby uniquely suited for the implementation of battery-free Smart Skin nodes for ubiquitous sensing.

The next sections will first introduce the concept of backscatter communications, before presenting a brief state of the art of its application into wireless sensing systems, and outline their limitations.

Backscatter communications

Fundamentally, active wireless systems such as the one schematized on fig. 1.9 are limited in their power consumption frugality by their requirement for a high frequency carrier-generating local oscillator which will, in optimal scenari, require $300\,\mathrm{nW}$ of power, and more than $1\,\mathrm{mW}$ for entire transceivers [62].

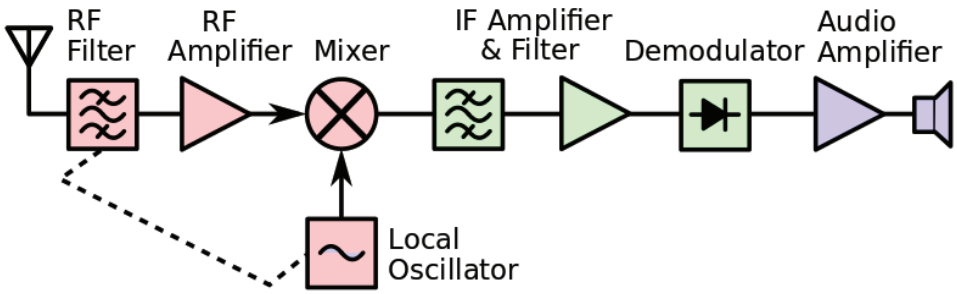

Figure 1.9: Diagram of a typical active transmitter [63]

One may wonder if it might be possible to generate a carrier externally and distribute it wirelessly to remote devices for their communications use. In essence, this is what backscatter communications enable. The process used to implement this far-fetched concept is the one drawn on fig. 1.10

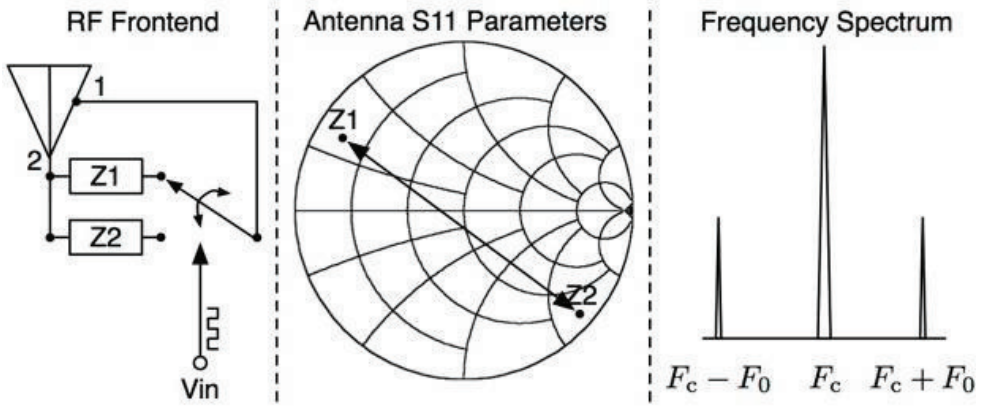

Figure 1.10: Schematic showing an implementation of backscatter communications [64], ©2014 IEEE

An impinging carrier signal of frequency f_c—sent by a dedicated source that can be co-located with the reader in standard backscatter implementations, or generated by local independent electromagnetic emitters in the case of ambient backscatter approaches [65]—is received by the antenna before being alternatively routed to one of two loads Z_1 and Z_2 (continuous sets of loads have also been used [8], but are outside of the scope of this work), corresponding to two distinct reflection coefficients Γ_1 and Γ_2 which modulate the phase and magnitude of the signal reflected towards the antenna before being subsequently re-emitted. Modulation between those loads renders the system non-linear, thereby creating detectable harmonics, as shown on fig. 1.10 in the case of the alternative switching between the two loads at a constant frequency f_0. The modulation creates two harmonics, $f_c + f_0$ and $f_c - f_0$ whose magnitude, as received by the reader, can be shown to be proportional to the complex distance $|\Delta\Gamma| = |\Gamma_1 - \Gamma_2|$ between those two reflection coefficients [66]. It should be noted that the entire front-end can be implemented using the mere switching of a single transistor, which can be driven (in the case of an FET) using as low power as a few hundreds of nW.

Passive RFID systems

RFID systems can either be passive, semi-passive or active. These different categories correspond to powering and communication scheme combinations. Active tags require an internal power source (a battery, usually) and use this power to generate RF waves for communication, as well as for running other operations (sensing, data collection and processing, etc.). Semi-passive tags are also internally-powered but rely on backscatter of the impinging reader-generated wave for communications ; other processes are dependent upon the power source. Finally, passive tags also use backscatter for communication, but also rely solely on harvesting of the impinging reader wave to power their operation. Furthermore, because of the focus on long range applications and the extremely small range (typically less than $1\,\mathrm{m}$) of lower frequency configurations, only UHF (around $900\,\mathrm{MHz}$) implementations will be discussed. The literature offers numerous examples of the use of off-the-shelf UHF passive RFID chips for sensing purposes, ranging from humidity sensors [67, 68] to ammonia [69, 70] and touch [71] sensors.

A passive tag is constituted of an RFID chip, and an antenna. In the first phase of the reading cycle, the reader sends a continuous wave towards the tag, which will then be harvested in order to power the chip. The minimum amount of power (radiated by the reader antenna) required to turn the tag on can be calculated by [72]:

$$P_{min} = \frac{4\pi}{\lambda}\frac{R^2 P_{th}}{G_t G \rho \tau} \tag{1.4}$$

,where λ, R, P_{th}, G_t, G, ρ, τ are, respectively, the wavelength, the reading distance, the chip power threshold sensitivity, the gain of the reader antenna, the gain of the tag antenna, the polarization efficiency, and the impedance matching coefficient between the tag chip and antenna. By being integrated into the radiating or matching structure, sensing components/films can, here, be used to induce changes in τ upon sensing. Therefore, for a known distance and configuration (which can be determined by the use of a reference tag [71]),

a remote determination of the lowest reader-emitted power required in order to receive a response from the tag indirectly gives τ, which can then be related to the properties of the sensor, and, finally, to the sensed parameter. As previously mentioned, the advantage of this mechanism is that it can be used with off-the-shelf, high-performance passive RFID chips. However, there are a few drawbacks that need to be resolved before a widespread implementation can take place. Indeed, the integration of sensor elements is not necessarily straightforward. For example, high resistance (more than $1\,\mathrm{k}\Omega$) resistometric sensors cannot effectively be integrated into the structure (without the addition of active components) without greatly negatively impacting the reading range. Furthermore, the reading range of these systems (similarly to all other systems that exclusively rely on instant-power RF energy harvesting) is limited by radiated-power regulations. Indeed, the maximum reading range can be expressed as:

$$R_{max} = \sqrt{\frac{\lambda}{4\pi}\frac{P_{EIRP}G\rho\tau}{P_{th}}} \tag{1.5}$$

, where P_{EIRP} is the maximum equivalent isotropic radiated power allowed by regulations. With state-of-the-art RFID chips, and current regulation values for these parameters, reading ranges are confined, in optimal cases, to values below $12\,\mathrm{m}$.

Semi-passive backscatter systems

Unlike the systems presented in the last section, the devices described here are not commonly built around the typical off-the-shelf passive RFID chip architecture. However, because of their power-efficiency, backscattered communication schemes can easily be used in those architectures. Their typical structure is shown in fig. 1.11, and includes an active circuit, one or several sensors, an antenna, a backscatter front end, and one or multiple energy harvesters (such a solar cell and a RF harvesting circuit). The most basic systems of this type are typically build around low power oscillators that are used to simply modulate in amplitude the signal during backscatter. This subcarrier frequency can then be received

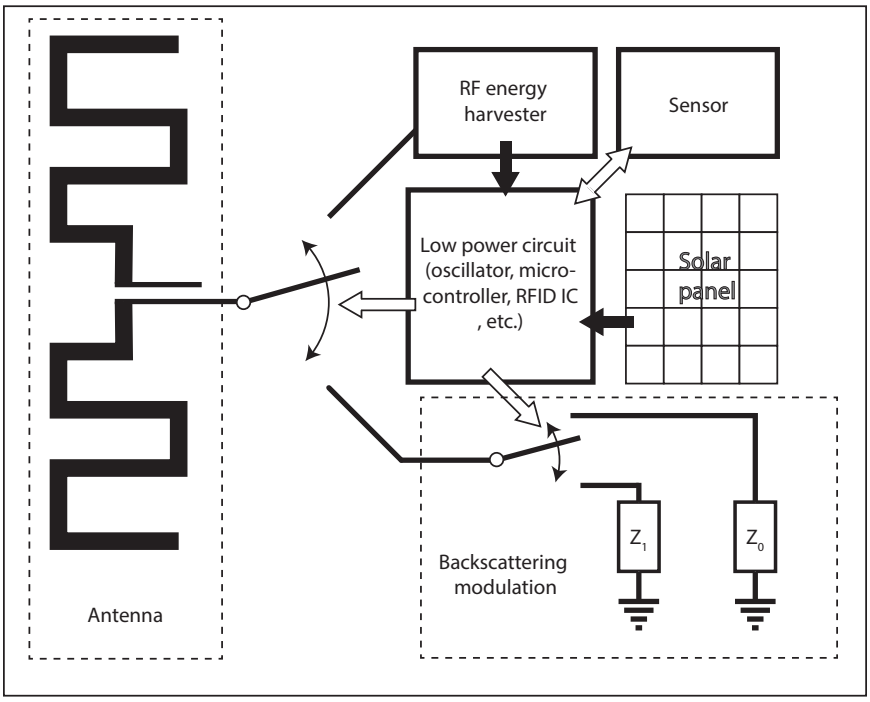

Figure 1.11: Schematic of a typical backscatter-communication low-power circuitry sensor structure

by the reader, and be correlated to a sensing component response and therefore encode the sensing data. Such a system prototype has already been implemented on a partially printed structure for ammonia sensing [73]. The Wireless identification and sensing platform (WISP), first introduced in [74], has been popularized by its compatibility with RFID EPC protocols and its flexibility, as a general purpose architecture. Its architecture is comprised of an RF energy harvester, powering a low-power microcontroller which conducts sensor measurements and controls communications, through backscatter modulation. Nevertheless, this system—being essentially a passive RFID on a board, with an added sensor interfacing capability [75]—is more power consuming than highly optimized off-the-shelf passive RFID tags. As a consequence, its equivalent P_{th} (with reference to eq. (1.5)) is higher, inducing a shorter maximum theoretical reading range of less than $2.5\,\mathrm{m}$. In parallel, integrated sensing-enabled passive RFID systems have also been developed, such as in [76], where both temperature and light sensors were integrated into a passive RFID architecture. Commercial versions of these chips with internal temperature sensor and external

sensor pins, such as the SL900A, from Austria MicroSystems (AMS), are now available. Nevertheless, they also suffer from the same cause for range limitation as that previously mentioned, and can only be read at maximum theoretical ranges of up to $2.8\,\mathrm{m}$ [77]. As a consequence of the fundamental limitations of RF energy harvesting for the powering of these devices, subsequent efforts have focused on higher energy density sources, such as solar [78, 79] or multi-form combinations of several harvesting sources [80]. The range of the WISP configuration was, in such a way, extended by a 6-fold, to $24\,\mathrm{m}$ [79]. Even though the use of currently used photovoltaic components can dramatically increase the cost of such devices, current trends in the development and cost-reduction of printed organic solar cells might bring commercial viability to such systems [81, 82].

1.4.4 Chipless technologies

As demonstrated in the last section, chips and backscatter-communications-enabled systems can provide autonomous solutions for wireless sensing, at ranges up to $4.5\,\mathrm{m}$ and $25\,\mathrm{m}$ by relying exclusively on RF and solar energy harvesting, respectively. Nevertheless, such systems rely on quite high performance electronic chips and components, which yet prevent them from being fully printed, and increases their unit cost. Indeed, even though very rudimentary fully-printed RFID systems have been demonstrated at HF ($13.5\,\mathrm{MHz}$), limitations in the mobilities of printed semiconductor materials, as well repeatability issues, and limitations in the minimum length of printable transistor channels are still preventing the emergence of fully-printable UHF RFID tags [83]. As a consequence, much attention has been given to structures that are usually referred to as chipless RFID's. As described by their epithet, such tags do not require chips in order to operate, and therefore solely rely on their passive interaction with, and reflection of, impinging reader electromagnetic waves. Therefore, such systems are passive and, therefore, do not require any power source: they are "zero-power". Furthermore, due to their lack of active components, such devices are generally fully-printable, and extremely low cost. However, their electrical structure

is therefore time invariant (if not for the presence of environment-modulated sensing elements). Hence, no modulation can be applied on a signal for communication purposes, and different schemes need to be utilized for information encoding. These schemes can generally be classified into two methods: frequency and time-domain-based.

Ultra Wide Band (UWB) Time-Domain Interrogation Approaches

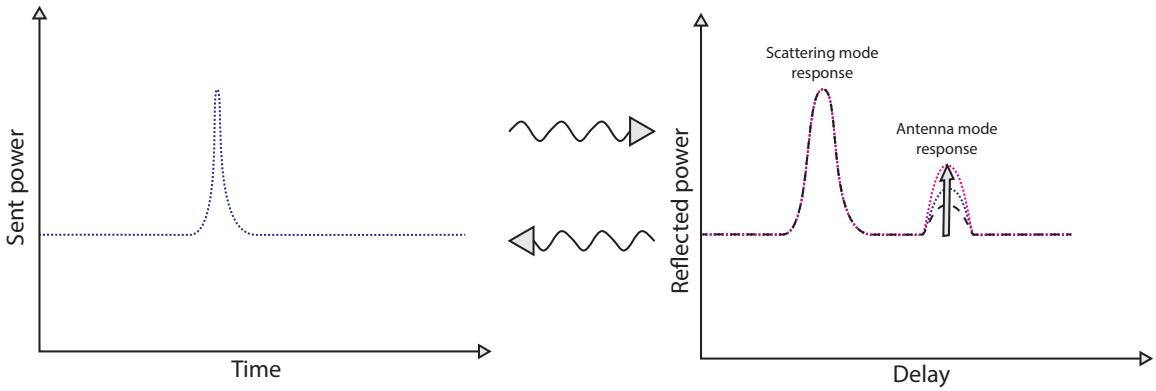

Figure 1.12: Principle of the UWB time-domain wireless sensor interrogation process

The main challenge to achieve an acceptable detectability of wireless RF sensing components lies in the interference from the environment. Indeed, a signal emitted from a wireless reader will propagate in numerous directions, being reflected by the environment. Subsequently, the signal measured by the reader is a combination of several components that include noise, interfering reflections from the environment, interference from nearby RF sources, an interfering reflection from the antenna's structure (the structural mode), and an information-enclosing (the signal) antenna mode. The physical difference between those two modes can be partially understood by considering a standard patch antenna. At any frequency, a metal patch can be considered a metal plate which, as a metallic object, reflects electromagnetic waves in a way that is controlled only by its structural shape. However, at its resonance frequency (and within its bandwidth), the structure also behaves as an antenna, absorbing a part of the signal (in its antenna mode), which can then be re-emitted. Refer to [84, 85] for a more detailed and rigorous description.

A major challenge for these strictly linear devices is therefore to isolate, in reception, the information-enclosing antenna mode signal from the interference. A standard modulator makes this process quite straightforward by modulating the antenna mode, and therefore allowing a differential measurement to be conducted. Chipless time-domain methods, which cannot rely on modulation, instead isolate different modes and interference by taking advantage of the (time-domain) phase delay, as seen in fig. 1.12. The encoding of data is achieved by connecting the tag antenna to a delay line that is terminated with a load whose impedance changes upon sensing. In the most common reading method using UWB readers, a short pulse is sent, and the response is time-gated, allowing for a precise detection of the variations in phase and magnitude of the received reflected antenna-mode wave, which can then be correlated to changes in sensor impedance and, therefore, in sensed parameters. Another commonly used interrogation method uses a frequency modulated continuous-wave (FMCW) radar system whose spectral output can be correlated to the delay and magnitude of the reflected signal. UWB and FMCW systems have been demonstrated for ethylene [86], pressure [87], and temperature [88] sensing, but could be easily extended to many other chemical and physical parameters, using the sensors described in section 1.4.1.

The main advantage of this technology is its ability to extract, even in some practical environments, very precise magnitude and phase information associated with the sensor antenna mode. Nevertheless, such readings are theoretically very sensitive to interference from objects at similar ranges (and therefore delay) as the sensor. As a consequence, even though those sensors are generally demonstrated in echoic environments, special attention is paid to place them away from nearby interferers (items are never placed on a wall, for instance). Furthermore, because of the short time-pulses that are necessary for UWB applications, the required absolute bandwidths are generally in order of more than $3\,\mathrm{GHz}$. At the relatively low operation frequencies of the demonstrated prototypes (usually centered around $3\,\mathrm{GHz}$), this represents a very wide relative bandwidth, which occupies much of the

spectrum. The use of these devices at higher frequencies could relax these UWB hardware and spectral occupation constraints, but this offers challenges of its own.

Frequency-Domain resonance interrogation approaches

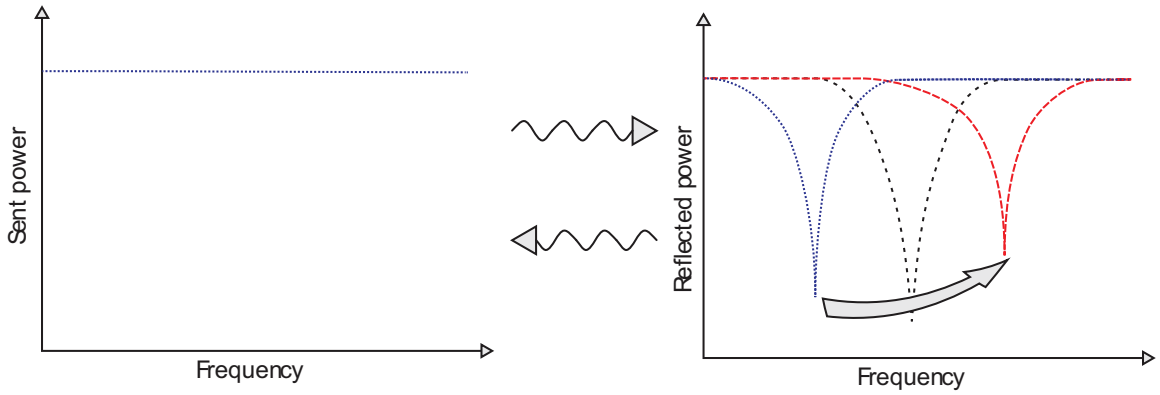

Figure 1.13: Principle of the typical frequency-domain-based wireless sensor interrogation process

In contrast with the time-domain-based technologies described in section 1.4.4, frequency-based sensing relies on spectral resonances to encode information; the reader scans through the frequency band, and measures the magnitude of the reflected signal at different frequencies. Because of its ease of use and manufacturing, this technology has attracted much attention, and has been utilized for carbon dioxide [89], and humidity [90] sensing. Nevertheless, it cannot easily differentiate between the useful antenna-mode signal response and that of the interference signals without proper use of gating. A clean signal, as the one shown on fig. 1.13, is typical of measurements in anechoic environments. While it is possible to gate the received signal, using precise enough gating to isolate the useful signal (especially from the device scattering mode) would require, similarly to the time-domain-based method, the use of large frequency bands. As a consequence, these devices are consistently demonstrated either at up to $2\,\mathrm{m}$ ranges in anechoic chambers, or at tens of centimeters, away from possible interferers, in practical environments. Recent improvements have, nevertheless, been demonstrated with the use of cross-polarizing structures [91].

The work undertaken during the course of the Ph.D. studies that generated the approaches and results presented in this document strived to push the boundaries of the art on several fronts, in order to cut part of the path towards the realization the devices described in section 1.1, and to light the rest of the way towards this objective. The reported work consists of efforts in three distinct but essential components of this project. In chapter 2, progress achieved in the understanding and achieved performance of ultra-low-cost fully-printed sensors for the detection of organophosphorus nerve agents is reported. The content of chapter 3 provide a theoretical argument for the use of mm-wave retrodirective architectures to develop ultra-low-cost chipless wireless tags featuring reading range more than one order of magnitude greater than that of the existing art, before demonstrating and analyzing such a system. The work described in chapter 4 translates the learning of the efforts in reported in chapter 3 to a backscatter system—along with an architecture that allows the immediate integration of the sensors presented in chapter 2—to report a new class of ultra-low-cost, low-profile and energy-autonomous backscatter tags for long-range real-time gas monitoring. In chapter 5, the work conducted in order to extend the reading range and enable the localization and spatial multiplexing of the mm-wave backscatter nodes of chapter 4 is described, before a description of the novel contributions of the presented work and its potential future directions are described in chapter 6, as a conclusion.

CHAPTER 2
CHEMICAL SENSORS

The ability to manufacture printed chemical sensors for nerve agent detection would provide effective solutions for the implementation of nerve agent alert systems over large and difficult-to-monitor indoor and outdoor environments. Nevertheless, no such sensor had previously been reported in the literature. This direction therefore offered a largely open research area, ripe for quick progress. Nevertheless, several challenges, inherent to the additive manufacturing of carbon nanomaterials-based chemical sensors were still to tackle. These included the intra and inter-batch consistency of fabricated sensors, as well as their achievement of sensitivities at levels sufficient for their envisioned applications.

2.1 Preliminary results

The determination of adequate materials and functional compounds for the optimal detection of a targeted analyte lies at the center of the quest for highly-sensitive gas detection elements. Unfortunately, the choice of such materials does not lend itself to effective straightforward theoretical selection, and a great deal of trial and error is often necessary. Due to the advantages described in section 1.4.1, 2D nanomaterials were adopted.

Preliminary, baseline, sensors built according to the work previously reported in [92] were printed and tested for their ability to detect ammonia and DMMP, a nerve agent simulant. These sensors were printed on a $125\,\mu\mathrm{m}$ thick polyimide Kapton HN film from Dupont. All the printing was done using a Dimatix 2831 inkjet printer with DMC-11610 $10\,\mathrm{pL}$ cartridges.

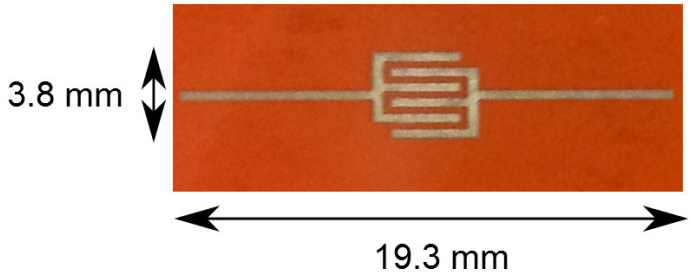

Figure 2.1: Fully inkjet printed carbon nanomaterial-based sensor on Kapton HN flexible polymer substrate

2.1.1 rGO sensor

GO ink

The graphene oxide ink was prepared by dispersing nano graphene oxide powder ($90\,\mathrm{nm}$ diameter flakes) from Graphene Supermarket (Reading, MA, USA) and commercially available negatively charged (carboxyl-terminated) polystyrene nanospheres into water. Glycerol was used as a co-solvent to increase the viscosity to about $10\,\mathrm{cP}$, in the range of optimal viscosity values for inkjet inks. The ink was then sonicated to ensure good dispersion of the particles in the solvent.

Surface modification of the polyimide film

The Kapton was first surface modified, with the process described in [92], in order to make the surface more hydrophilic and therefore improve the printing quality of water based inks. This was done by introducing a layer of positively charged particles (such as amine groups) on the surface of the film and then utilizing a layer-by-layer dendritic amplification process to increase the density of surface groups. This process was repeated as many times as necessary in order to get high enough charge density at the surface of the polyimide film.

Printing and reduction process

Graphene, itself, cannot practically be printed. GO is an oxidized, vitiated version of graphene that can readily be dispersed into an ink and printed. In order to recover some or (ideally) all of graphene's unique advantages, the GO needs to be reduced into rGO. This is the process that was adopted for the fabrication of the first batch of sensors. Between 5 and 30 layers of the previously described GO ink were then inkjet printed onto the substrate in order to deposit square patches of graphene oxide nanoparticles. The ink was carefully and slowly dried at $90\,^{\circ}\mathrm{C}$ for 5 hours in order to obtain as uniform a particle deposition as possible. The samples were then put in a vacuum oven at $100\,^{\circ}\mathrm{C}$ for 10 hours in order to remove the potentially left-over glycerol. The GO films were subsequently washed with acetone to remove the polystyrene nanospheres before the printed GO flakes were reduced at $300\,^{\circ}\mathrm{C}$ for 1 hour in an atmosphere of 98% of N_2 and 2% H_2 in order to obtain patches of reduced graphene oxide (rGO).

Finally, interdigitated electrodes (IDEs), with $4\,\mathrm{mm}$ long and $350\,\mu\mathrm{m}$ wide fingers separated by $350\,\mu\mathrm{m}$ wide gaps, (Figure 2.1) were fabricated by printing 5 layers of commercial silver nanoparticle ink, from Suntronic, before drying them and sintering the silver nanoparticles in an oven at $110\,^{\circ}\mathrm{C}$ for 3 hours.

Characterization

The sensors were tested for their expected ability to detect ammonia, in order to set a baseline design from which to branch out in search of DMMP detection capabilities. The sensors were tested in the chamber described in chapter A. The sensitivity of a 10 GO-ink-layers rGO sensor is shown in Figure 2.2. This sensitivity is compared with the recorded concentration of a commercial ammonia detector from BW Technologies.

The relative sensitivity of a sensor is defined as

$$S(t) = \frac{R(t) - R(t_0)}{R(t_0)} \tag{2.1}$$

where $S(t)$ is the relative sensitivity of the sensor at time t, $R(t)$ is the resistivity of the sensor at time t and $R(t_0)$ is the resistivity of the sensor at the reference 'starting' time t_0.

On the plot of Figure 2.2, the reference time was taken at $t_0 = 0$. The sensors displayed a maximum response of about 8.5% with a response time of 20 minutes for an ammonia concentration of less than 30 ppm. With more than $2.8\,\%/10\mathrm{ppm}$, this makes it the most sensitive inkjet printed rGO ammonia sensor compared to the state of the art of about $2.1\,\%/10\mathrm{ppm}$ [93]. The absorption rate of the gas by the rGO decreases as more has been absorbed and eventually making the sensitivity saturate at its maximum value for that concentration. The ammonia feeding having been stopped before complete saturation of the sensitivity, the intrinsic maximum sensitivity of the sensor is actually higher than measured here. The responses from the rGO sensor and the commercial sensor are very similar during the first 20 minutes. This shows that the response time of the inkjet printed sensor is very comparable to that of a commercial ammonia sensor. The major difference between the performance of the two sensors is the desorption capability. In this configuration, the rGO sensor does not come back to its original state after sensing, and a second exposure (to about 10 ppm) only induces a small response from its new baseline resistance. Inkjet printed heater solutions are now being developed to heat the sensor after exposure in order to trigger a complete and fast desorption.

Despite their remarkable response to ammonia, the printed rGO sensors displayed a complete lack of sensitivity to our target of interest: DMMP. Another sensing material—CNTs—was, therefore, considered.

2.1.2 CNT sensor

The processes used for the reduction of GO into rGO cannot even come close to fully recovering graphene: they leave behind a stack of carbon sheets that are replete with chemical defects. Furthermore, the flakes—of varying dimensions and states of disfiguration—cannot provide "pure", controlled properties. Pristine carbon nanotubes, on the other hand,

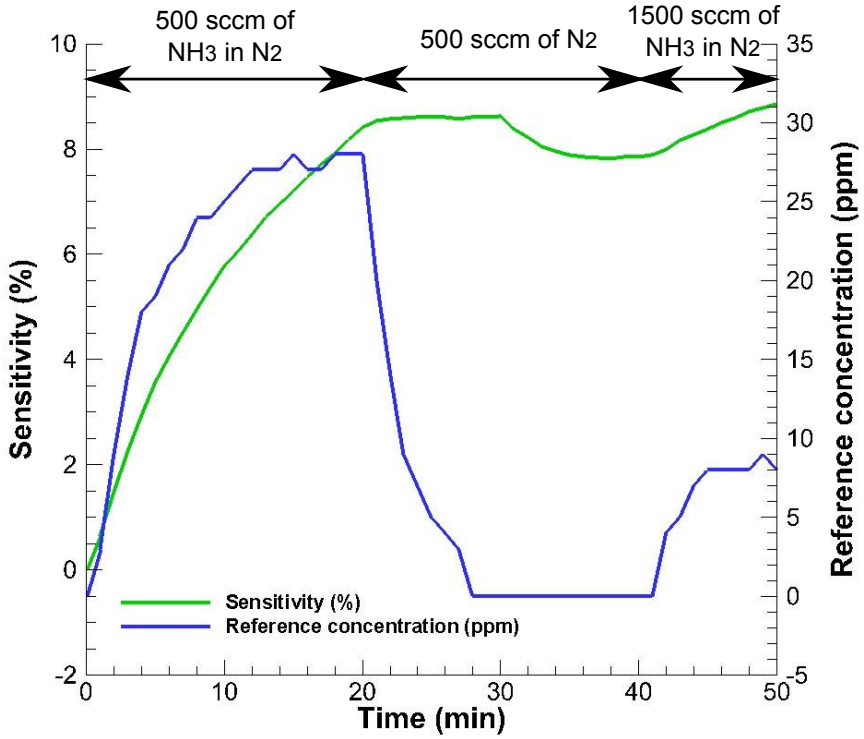

Figure 2.2: Measured sensitivity response of the rGO ammonia sensor (green) and reference concentration measured by a commercial ammonia sensor (blue)

can be dispersed in inks and printed. Also, CNTs can be filtered and separated according to their chirality-driven electrical properties: usually semiconducting on the one hand, and metallic on the other. For these reasons, CNTs were adopted in the rest of the reported work.

CNT ink

CoMoCAT CG300 single wall CNTs (SWCNTs) from SouthWest NanoTechnologies, were dispersed in Dimethylformamide (DMF) and sonicated with a probe sonicator. Increasing concentrations were tested to find the highest concentration that offered good dispersion of the CNT and stability of the ink over time. This maximum concentration, $25\,\mathrm{mg\,L^{-1}}$, was then used in the final CNT-based ink.

Printing and measurements

Between 5 and 30 layers of the previously described CNT ink were then inkjet printed onto the substrate to deposit square CNT patches. The ink was left to dry at room temperature before the samples were put into a vacuum oven at $100\,^{\circ}\mathrm{C}$ for 10 hours to remove the potentially left-over DMF. Measurements were taken with 5 sensors printed with 20 layers of CNTs. None of the printed sensors displayed any sensitivity to DMMP. The next section reports the steps that were undertaken to not only obtain a response, but to amplify that first response by orders of magnitude to obtain the most sensitive fully-printed DMMP sensors ever reported.

2.2 Sensitivity improvements

CNTs have been shown to serve as a conductive template that can then be chemically functionalized to target one specific gas. As a consequence, the use of functional groups to increase the sensitivity and selectivity of CNT-based sensors can be applied to detect nerve agents, or even to form an array composed of differently-functionalized sensors capable of detecting and recognizing a wide range of gases [94].

2.2.1 Chemical functionalization

The fabrication (shown in fig. 2.3) was conducted on a Kapton polyimide substrate, through the inkjet-printing of a custom-made ink, consisting of CoMoCAT CG300 carbon nanotubes, dispersed in Dimethylformamide (DMF). Firstly, inter-digitated electrodes were printed onto the substrate using a silver nanoparticle (SNP) ink. The CNT ink was then printed onto the electrodes and their gaps, in a what-you-print-is-what-you-want pattern approach, before being dried in a vacuum oven at $100\,^{\circ}\mathrm{C}$ for 10 hours. Finally, the inkjet printed CNT films were functionalized with carboxyl, amine or hydroxyl groups or a hexafluoroalcohol (HFA) using a set of reactions previously reported in [95, 96, 97].

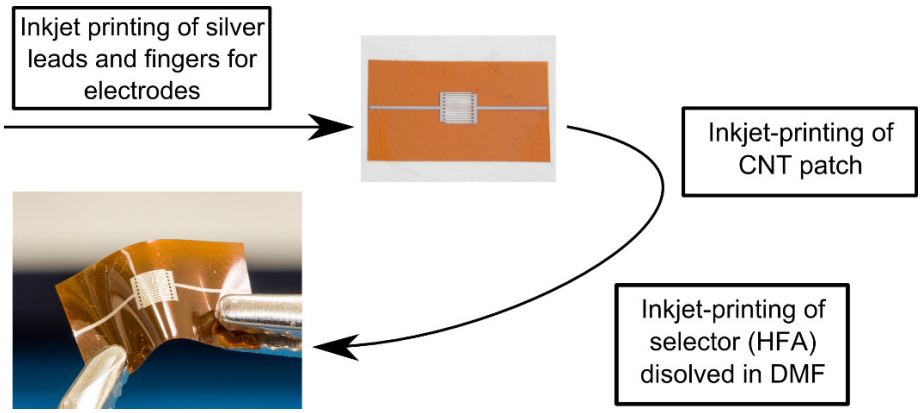

Figure 2.3: Original printing process of the CNT-based DMMP sensors

The measured sensitivity results of the sensors are shown in fig. 2.4. It can be seen that the HFA functionalization provided an increase in the sensitivity of the sensor of more than an order of magnitude compared to pristine and differently functionalized CNTs.

Additionally, an inverse dependency of the sensor sensitivity with the number of layers was also observed. The measurement data of an HFA-functionalized 10 layer sensor is shown on Figure 2.5. At the 15 minutes mark after the beginning of the exposition to DMMP, the 10 layer sensor displayed about a 2.5% sensitivity compared to the 1.2% of the 20 layer sensor. With less than 10 layers, the resistivity of the sensor became too high to measure. This decrease in sensitivity with increasing CNT amount is attributed to the reduced availability of some of the CNTs for interaction with the surrounding gas, as the thickness of the film increases. It is difficult for the gas analyte to interact with the CNTs that are at the bottom of the printed layer. However, these "buried" CNTs still contribute to the conductivity of the film, therefore reducing the overall sensitivity of the resistometric sensor.

This sensor, reported in [98], provided the first demonstration of a fully-inkjet-printed DMMP sensor.

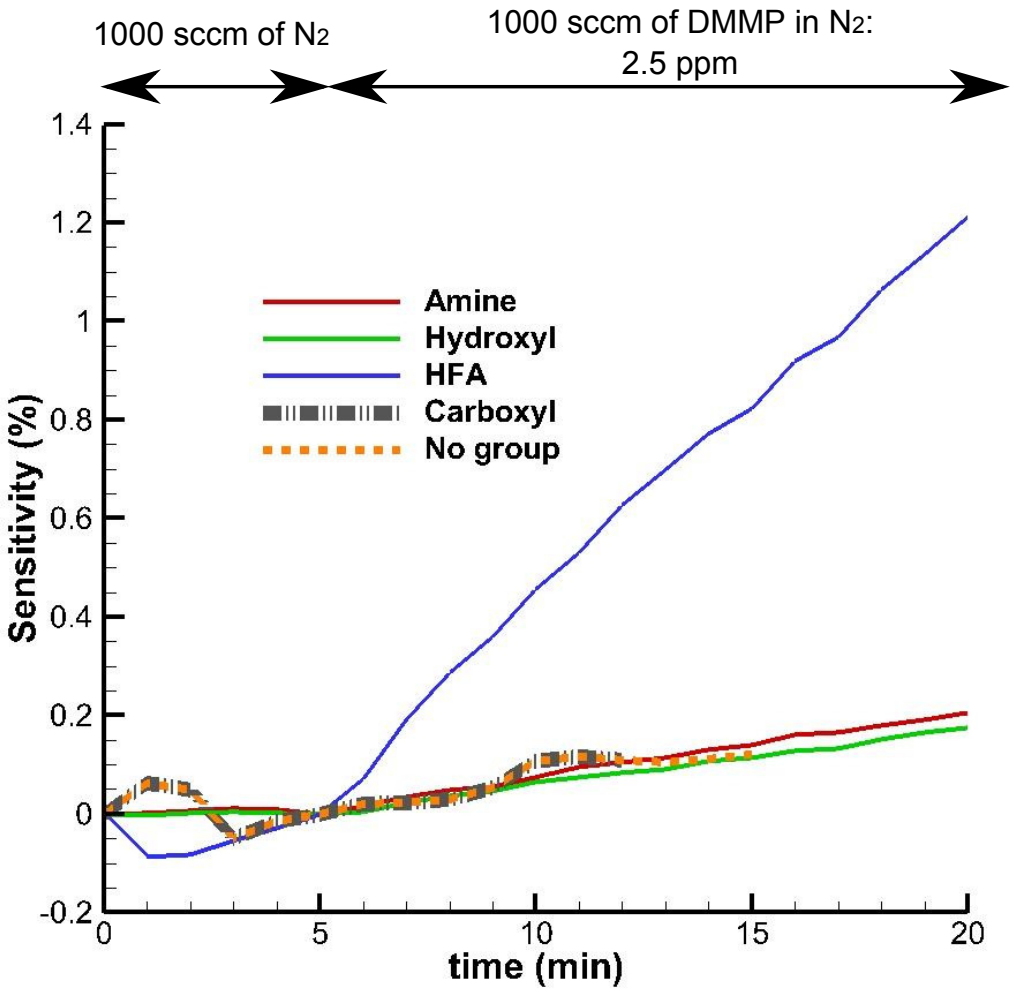

Figure 2.4: Measured sensitivity to DMMP of CNT-based sensors with different functional groups

2.2.2 Electrodes-mediated sensitivity improvements

While functional, the HFA-functionalized sensor whose sensitivity is displayed in fig. 2.4 offered rather poor performance, especially compared to that of SOTA non-printed DMMP sensors such as that reported in [38]. Subsequently, more combinations of materials and fabrication processes were tested, leading to several orders of magnitude of improvement in the sensors sensitivity, as shown in fig. 2.6.

First, a gold nanoparticle (GNP) ink was substituted in place of its SNP counterpart for the printing of the interfacing IDEs, providing an order of magnitude improvement of the

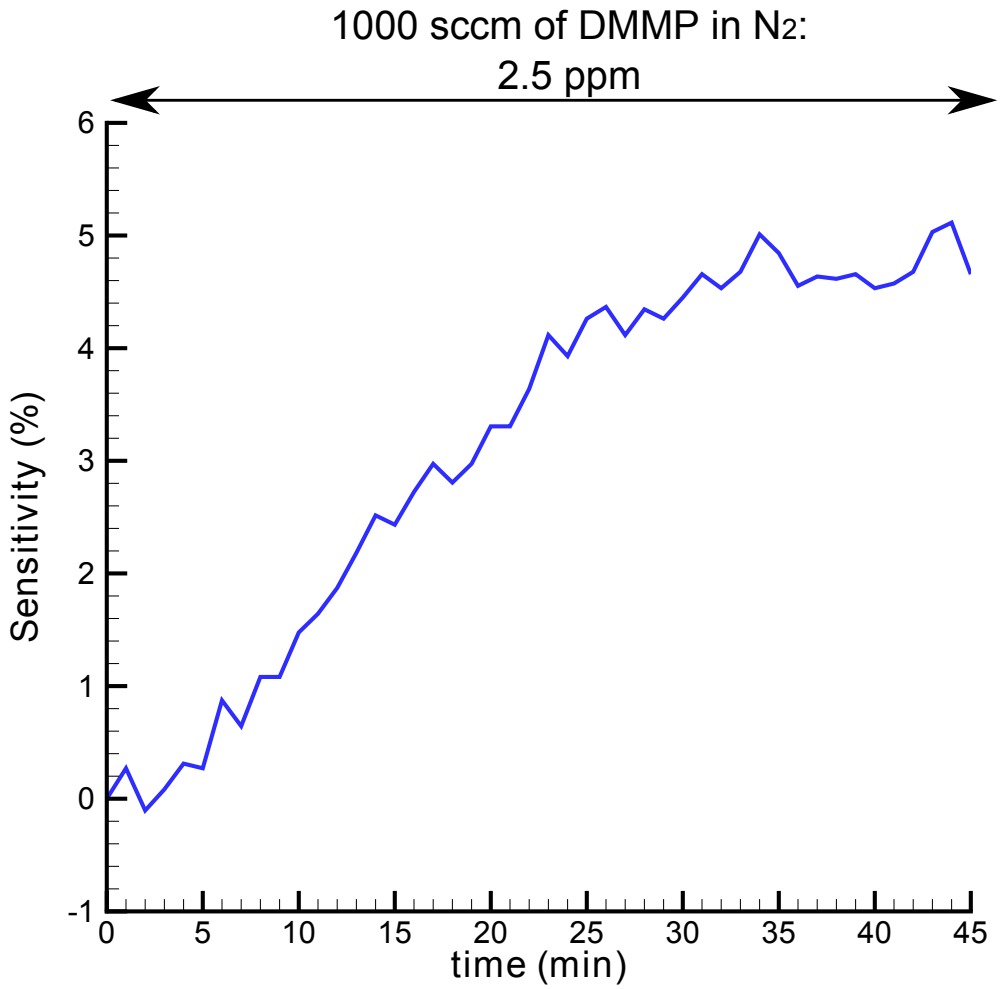

Figure 2.5: Measured sensitivity of an HFA-functionalized 10 layers inkjet printed CNT sensor

sensitivity to DMMP. Then, a new printing method (detailed in section 2.2.3, and shown in fig. 2.7) was implemented, consequently increasing the measured sensitivity by 3-fold. Finally, a change in the drying temperature of the printed electrodes was noticed to provide almost an additional order of magnitude improvement in performance.

These experimental results offer an insight into the fundamental physical phenomena involved in the behavior of printed CNT-based sensors of this sort. Indeed the variations in the performance of the sensors upon a change in the material of the printed electrodes points to a mechanism that involves both the metal electrodes and the semiconducting material: Schottky contact modulation (as already reported in [99]). This hypothesis is also

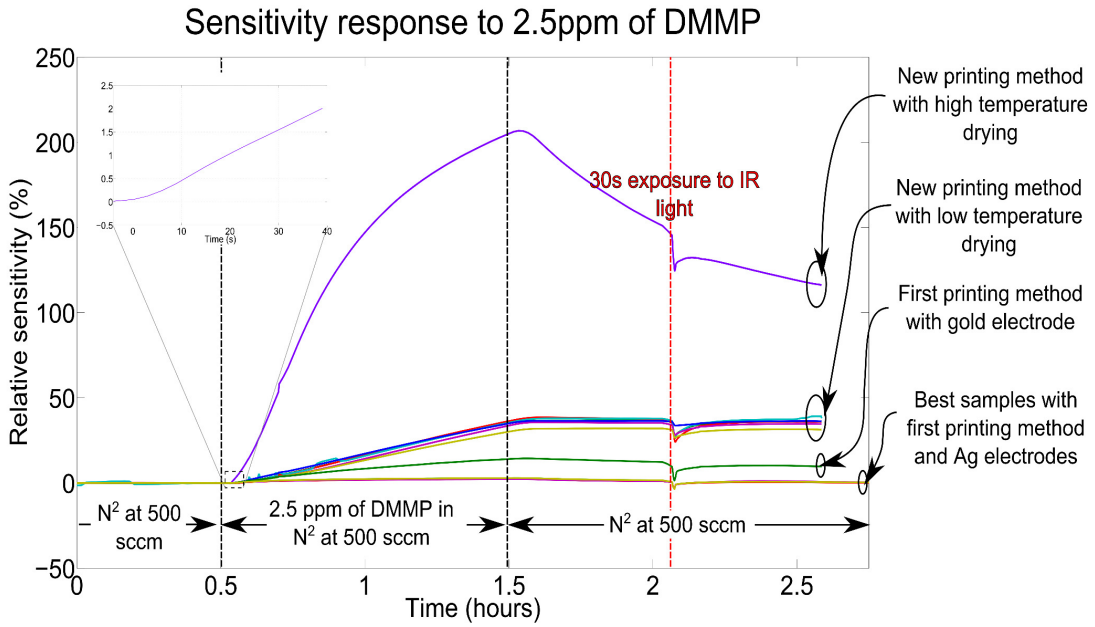

Figure 2.6: Compared performance of fully-inkjet-printed CNT-based DMMP sensors, fabricated with different fabrication processes and materials

.

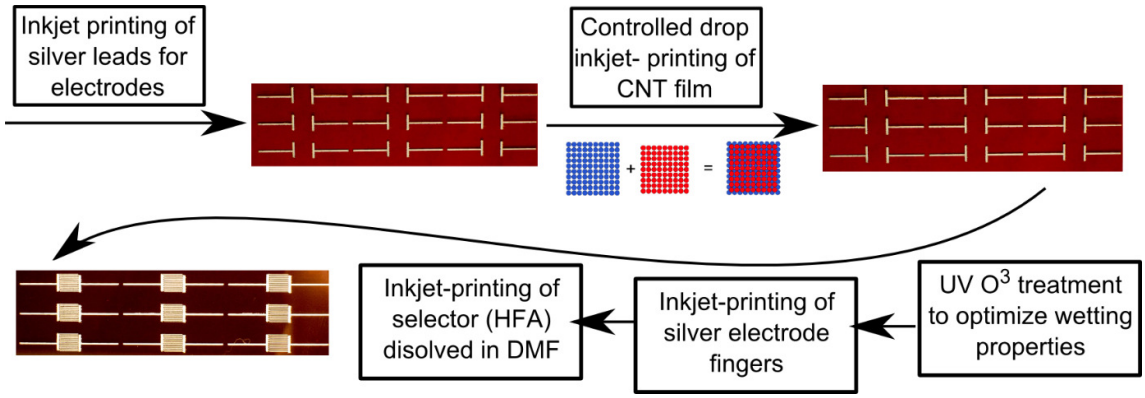

Figure 2.7: New and improved printing process

consistent with the observations made on the topology of the electrodes dried at lower and higher temperatures. Indeed, as can be seen on fig. 2.8 for two samples varying only in their drying temperatures, these show high porosity at high temperature. This effect, therefore, significantly increasing the surface area of exposed CNT/silver interfaces.

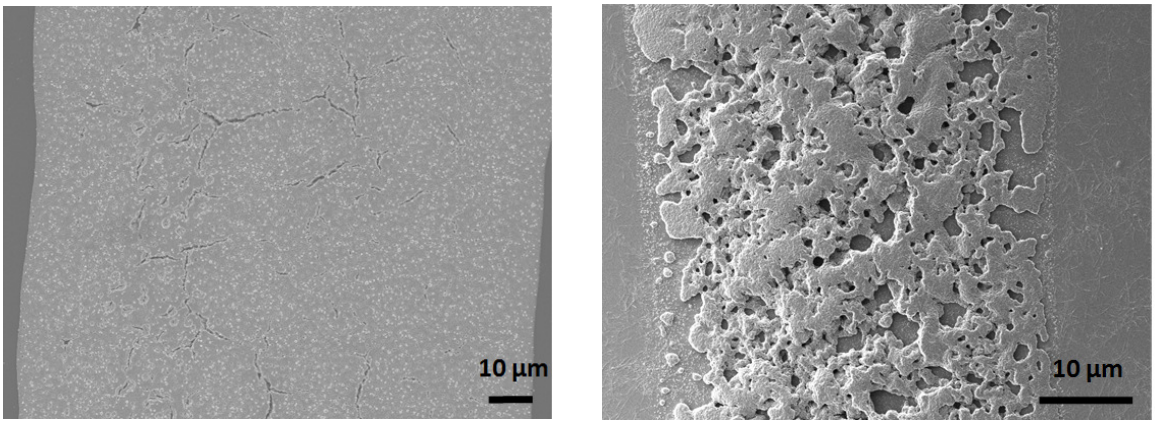

(a) (b)

Figure 2.8: SEM images of the surfaces of the silver SNP electrodes inkjet-printed and then dried at (a) 120 °C and (b) 200 °C.

2.2.3 Printing consistency improvement through sequential printing and patterning

The deposition of particles dispersed into a fluid, through the mean of a wet printing process, involves two main steps: fluid deposition and ink spreading and drying. The fluid deposition process is only influenced (in the inkjet printing process) by the fluidic properties of the ink and small variations in the jetting process (excluding the absence of jetting altogether) are not generally consequential on the quality of the deposition.

Figure 2.9: Image of a sensor, printed using the process shown in fig. 2.3

On the other hand, however, the mechanisms dictating the spreading a drying of the deposited ink onto a given substrate are far more complex, subtle, and consequential ; furthermore, these cannot be optimized for a given ink, independently of the substrate that is printed onto. On polyimide substrate, the wetting properties of CNT-compatible solvents– DMSO, DMF and water with surfactant–are inadequate, and cannot efficiently be improved through the use of low-complexity and low-cost substrate surface modification techniques such as UV-ozone treatments. The consequence of such poor wetting properties can be observed in fig. 2.9, where the uneven ink migration during drying (shown in fig. 2.10) creates a strikingly visible non-uniformity in CNT deposition density. As a consequence, extremely wide variations in the distribution and pattern of deposited CNTs are induced, even between sensors of a same batch ; this lead to several-fold (up to two orders of magnitude) differences in the sensitivities of these sensing elements, which lead to extreme integration and manufacturing yield impediments.

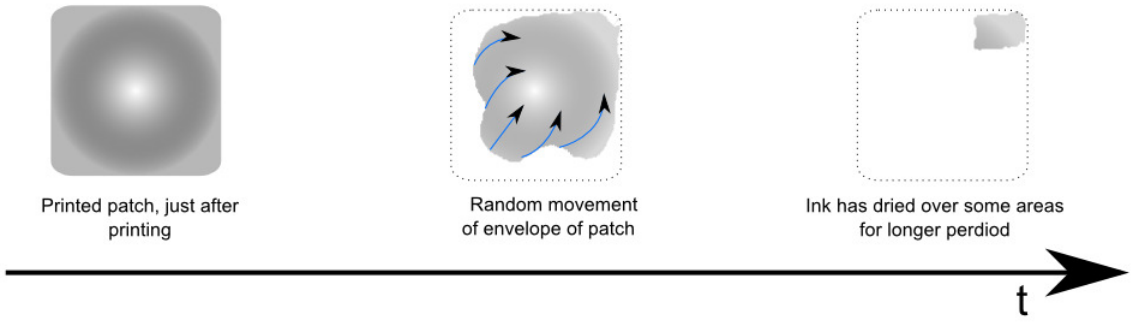

Figure 2.10: Uneven drying and particle deposition process mechanism

In an attempt to tackle this otherwise seemingly unresolvable barrier to uniform and repeatable CNT deposition, the high-resolution patterning properties of inkjet-printing were taken advantage of. The adopted process, displayed in fig. 2.11, consists of two (or more) complementary drop patterns that are printed and dried alternatively.

This scheme does not allow the long-range particle migration that is otherwise observed in complete patches (along the process displayed in fig. 2.10) to occur ; instead, these fluid movements during drying are constrained within each individual drop.

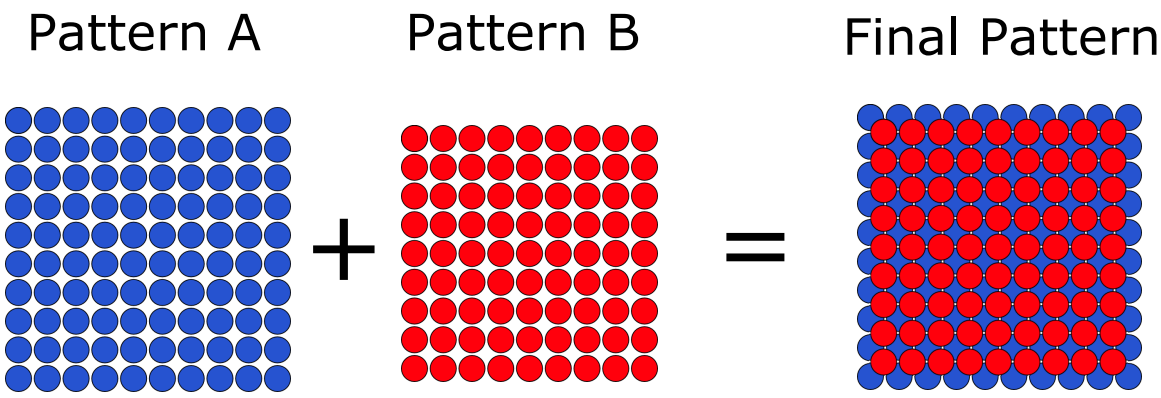

Figure 2.11: Schematic of the complementary-patterns printing scheme

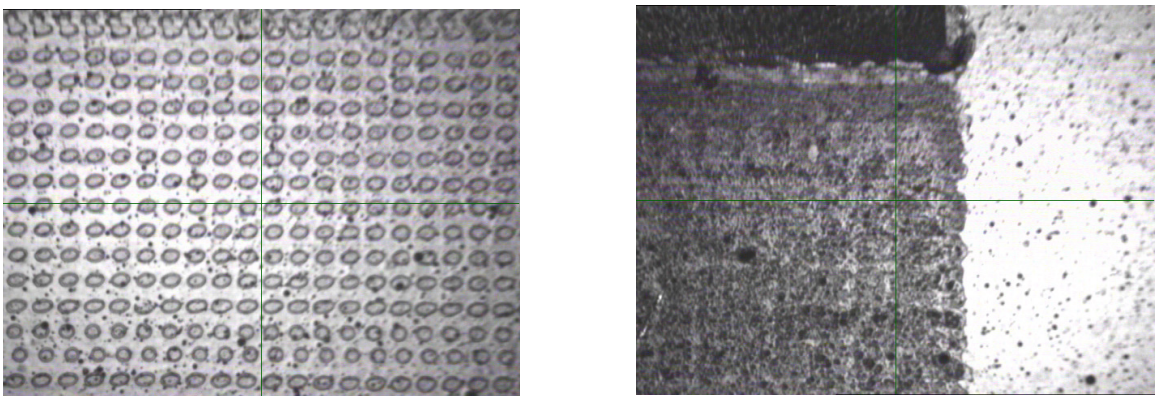

(a) (b)

Figure 2.12: Optical images of (a) one pattern of the printing scheme and (b) the final uniform CNT film

The deposition obtained after repeatedly printing only one of the patterns (shown in fig. 2.12a) shows the expected result, with the deposited CNT being constrained to the support of their individual drop. The final deposited pattern, shown in fig. 2.12b, displays (as expected) a much better uniformity than that of the what-you-print-is-what-you-want approach, the result of which was shown in fig. 2.9.

A new test bench, designed to allow the characterizations of the consistency of printed sensors, was assembled and is shown in . The measurements lead to the conclusion that, as expected, this repeatable printing process allowed the fabrication of batches of sensors that are extremely consistent in sensitivity, as shown on the plot of fig. 2.13.

In conclusion, the work described in this section presents the first implementation of a

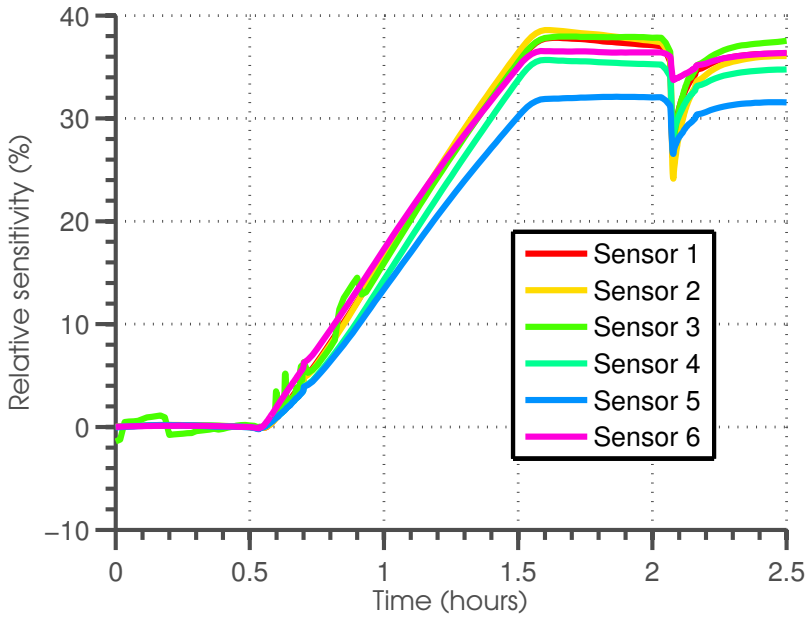

Figure 2.13: Measurement of a consistent batch, tested using the same protocol as with all of the sensors whose testing results are shown in fig. 2.6

fully-inkjet-printed DMMP sensor. Furthermore, in addition, new printing and processing mechanisms and schemes were implemented, allowing much better fabrication yields, and providing an increase in the sensitivity of such sensors by more than two orders of magnitude, compared to their first implementation. The following chapters will describe the mm-wave and systems engineering efforts leading to the integration of such sensors into ultra-low-power long-range sensing skins.

CHAPTER 3

THE FIRST DECAMETERS-RANGE CHIPLESS RFID

This chapter will first describe a piece of insight which has empowered most of the electrical engineering work described in this thesis, followed by how this insight was implemented and leveraged in order to achieve the first decameters-range chipless RFID.

3.1 The case for high frequency Van-Atta structures

3.1.1 The rise to mm-wave-frequency operation

Whether they are applied to identification and/or sensing purposes, passive chipless RFID structures fundamentally rely on their radar cross section (RCS), and its shape, signature and variation over frequency and time delay, to convey information ; the tag operates as a target for a radar-like reader to interrogate and detect. Nevertheless, the response received in the reply to the reader's interrogation signal, in practical environments, is a combination of several components:

- **The signal produced by the antenna mode of the tags:** This signal would be the one varying upon electrically switching properties of the antenna structure, as would be the case for standard passive and semi-passive RFIDs.

- **Interference:** generated by reflections induced by the tag's scattering mode. For a metal-backed antenna tag, the bulk of the contributions to this mode come from the specular reflection onto its metallic ground plane.

- **Interference from the background environment (a.k.a. clutter):** While the environment appears in the form of channel variations over time for non-linear communication systems, its contribution to linear communication approaches such as the one

experienced in chipless RFID situation is that of an interferer;a large fraction of the energy radiated by the reader during the polling is reflected back by the environment, which constitutes the response of interest for standard radar systems.

- **Noise**, originating from the environment or reader equipment.

In the absence of non-linear effects (such as diode-mediated frequency doubling, or modulation), all of these components cover a very narrow frequency band at a given instant, whose width can only be attributed to stochastic contributions of environmental Doppler and electronic jitter. The signal cannot, therefore, be spectrally isolated, with a given excitation, and can consequently easily be drowned in the interference. Naturally, detection and extraction of the tags' responses (i.e. their antenna-mode reflection) is the main challenges in chipless RFID implementations. The following reported work leverages two main strategies to enhance the detectability of chipless RFIDs, thereby allowing their read at extended ranges:

- RCS-based isolation can be used in order to increase the magnitude of the signal, relative to the interference and noise components levels. This can be achieved by, of course, increasing the magnitude of the RCS (making the structure electrically bigger), but also by implementing polarization isolation between signal and interference [100, 101, 102]. In other terms, a target that responds with a high level of signal is, naturally, easier to detect and becomes all the more visible if its response displays polarization effects that are uncommon it its environment. For instance, environmental-clutter-based interference tends to conserve the original polarization of an impinging linearly-polarized electromagnetic wave. A tag that rotates this polarization upon re-emission would therefore generate a very recognizable signature.

- Frequency and time-delay-based isolation can be applied by discriminating between responses that can, in time and frequency, reasonably be attributed (by filtering) to the tag rather than clutter components. Self-interference whereby a subset of the

power sent out the TX channels couples directly to the RX is the main interference source in most readers. In our linear system, this generally drowns the tag response and, therefore, needs to be dealt with. It is standard in the field of chipless RFIDs to apply what is referred to as "envrionmental calibration, where a measurement of the response of the environment in the same configuration as that used during interrogation is taken and used as a reference for later tag detections. While this method presents great performance in anechoic chambers (where it can readily de-embbed) the cross-talk, it fails to account for the variations of the environment and is, therefore, quite limited. A more robust approach consists in the gating of the data, coupled with pattern recognition, as will be described later.

With these elements in mind, higher frequency operation can be shown to offer tremendous gains in signal detectability for several fundamental and practical reasons.

- One can show that, by increasing operation frequencies for given dimensions, better link budgets and, therefore, longer ranges may be achieved. Let us see why. Using $A = \frac{G\lambda^2}{4\pi e_a}$ (where A is the physical antenna aperture, G the antenna gain, λ the wavelength, and e_a the antenna aperture efficiency), and the Friis equation, the power received from a monostatic RCS-based reader system, aiming at a tag target, can be expressed as follows:

$$P_r = P_e e_{a,r}^2 e_{a,t}^2 A_r^2 A_t^2 F_t^2(\Theta) \frac{1}{(\lambda R)^4} \tag{3.1}$$

where R, P_e, P_r, $e_{a,r}$, $e_{a,t}$, A_r, A_t and $F_t(\theta)$ are, respectively, the reading range, the emitted power, the received power, the aperture efficiencies of the reader antennas (assuming identical antennas), the aperture efficiency of the tag/target/sensor antenna, the physical aperture of the reader antennas, the aperture of the tag, and the radiation pattern of the tag. This can also be rewritten as:

$$P_r = P_e e_{a,r}^2 A_r^2 F_t^2(\Theta) \frac{\sigma}{4\pi\lambda^2 R^4} \tag{3.2}$$

where

$$\sigma = \frac{4\pi e_{a,t}^2 A_t^2}{\lambda^2} \tag{3.3}$$

is the RCS of the antenna-mode of the tag.

From a tag perspective, these equations lead to several key conclusions. From eq. (3.2), we can see that the tag is more detectable when the antenna-mode RCS increases. Furthermore, eq. (3.3) shows us that the RCS of a tag, with a given surface A_t and aperture efficiency $e_{a,t}$, increases with f^2, where $f = \frac{c}{\lambda}$ is the frequency. Therefore, all of the other parameters being equal, the detectability of the tag significantly increases with frequency. In addition, eq. (3.1) allows us to draw a conclusion from a system perspective. Indeed, overall received power varies as $A_r^2 A_t^2 f^4$. Therefore, by increasing the operating frequency, a system (reader antenna and tag) with given physical dimensions can achieve a much higher detectability and a system with given detection capability can be made much more compact. These gains can intuitively be understood as the product of two distinct mechanisms. For a given reader antenna aperture, higher frequency enables higher directivity, leading to a higher power density emitted by the reader to the narrower main beam direction where the tag lies. Secondly, the fraction of this energy intersected by the tag (which is a constant of frequency due to the assumption of constant tag antenna aperture) is re-emitted towards the reader with higher directivity as well, reducing the amount of signal that is "wasted in other directions than the reader's. It should also be noted that this first mechanism may not generally be practically fully leveraged due to regulatory limitations in Equivalent Isotropic Radiated Power ($EIRP = P_e G_t = \frac{P_e 4\pi e_a}{\lambda^2}$). However, at constant EIRP, the link budget still scales by a substantial square of the operating

frequency, as $A_r A_t^2 f^2$.

- At higher operating frequencies, clutter removal becomes easier. Indeed, higher gain of the reading antenna has the effect of decreasing the received level of interference originating from the environment outside of the its narrowing (with increasing frequency) main lobe. In addition, range-filtering (as we will see) has a theoretical resolution limited by:

$$\sigma_t \geq \frac{4ln2}{\pi\sigma_f} \tag{3.4}$$

$$\geq \frac{4ln2}{\pi\sigma_{f_r} f_0} \tag{3.5}$$

where σ_t is the range resolution, σ_f is the bandwidth of the narrowest-band element of the system (either tag of reader) of the responses are constrained by $(\sigma_f)_r$ is the relative HPBW and f_0 is the center operating frequency of the Gaussian frequency response.

Nevertheless, high directivity of the tag-structure can come with a high cost for practical applications, as $F_t(\Theta)$ becomes much less isotropic and decreases sharply when the relative direction of the reader moves away from the tag antenna boresight: the angular tag interrogation range hence becomes much narrower. Nevertheless, this problem can very efficiently be tackled through the use of of retrodirective structures such as corner reflectors or Van-Atta reflectarrays [103]. The Van-Atta approach was adopted here due to its compatibility with planar implementations, allowing sticker form-factors.

3.1.2 The Van-Atta reflectarray

Van-Atta reflectarrays, whose principle is shown in fig. 3.1, are constituted of an array of antennas, interconnected in symmetrical pairs (with reference to an axis or center of symmetry, in the middle of the structure).

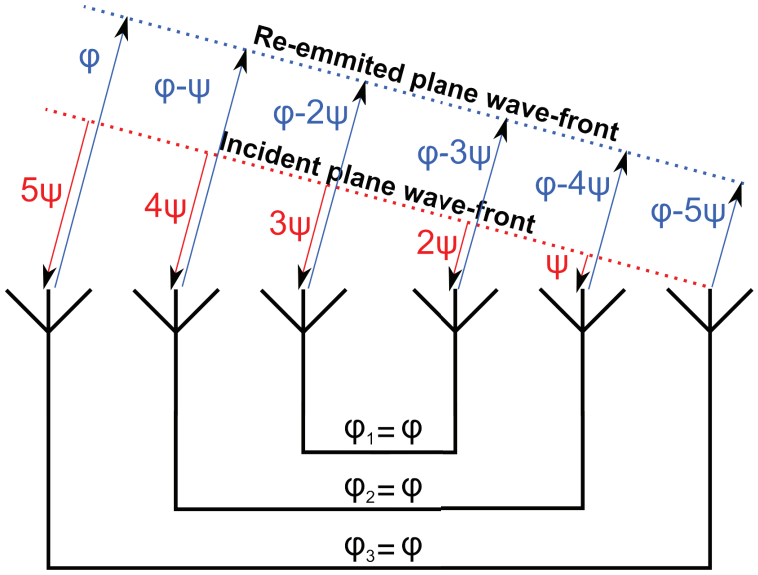

Figure 3.1: Van Atta operation principle schematic

Such structures display remarkable properties, if and only if all its connecting lines are of identical electrical lengths. Indeed, such a configuration induces phase conjugation and the consequent in-phase re-emission of any received wave. In the context of a reader/tag configuration, the boresight of this high gain tag antenna structure is therefore consistently directed towards the reader, regardless of its position, within a wide angular range. This enables the Van-Atta structure with a unique combination of high and theoretically isotropic RCS: the trade-off between high RCS (displayed by large structures) and isotropic RCS behavior (observed in small structures) no longer applies. Moreover practical implementations of cross-polarizing of Van Atta reflectarrays– where the reflected signal is cross polarized with respect to the impinging reader wave–have been demonstrated in the past [100], using two-port rectangular patch arrays. As a consequence, with the considerations of section 3.1.1 in mind, the structure can offer large signal to interference and noise isola-

tion thanks to both high RCS and polarization discrimination, while being detectable from a wide range of directions.

3.2 Inkjet-printed Van-Atta reflectarray design and fabrication

3.2.1 Linear antenna array

One of the aspirations of this effort was to develop a low cost structure, that could easily be printed onto a flexible, low-cost substrate. As a consequence, a minimalist single-layer via-less structure was adopted. First, a one-dimensional microstrip patch antenna array, with two ports (each exciting one of the two cross-polarized degenerate rectangular patch antenna modes), was designed for operation at $30\,\mathrm{GHz}$. The input impedance of each of the patch antennas was tuned to $R_{res} = 178\,\Omega$ to accommodate the requirements of the feeding network. With the selected feeding topology, the input impedance of the linear array was therefore $R_{in} = \frac{R_{res}}{N}$, where N is the number of patch antennas. The number of antennas was then chosen as $N = 5$ in order to maximize the overall gain, while utilizing a very manageable characteristic impedance of $\frac{R_{res}}{5} = 39\,\Omega$ for the connecting network lines. A taper from a $50\,\Omega$ to the $39\,\Omega$ lines was then added for measurement purposes.

One proof-of-concept prototype of this component was fabricated (fig. 3.2) using a Dimatix DMP2830 inkjet-printer and a silver nanoparticle ink from Suntronic, on 5-mil-thick Dupont Kapton HN, a low cost flexible substrate. In order to insure an optimal modeling of the fabricated arrays, the effective permittivity (ϵ_{eff}) of microstrip lines, printed on the Kapton substrate, was measured using a two-line phase-shift method, at 30% relative humidity (RH) and an ambient temperature of $25\,^{\circ}\mathrm{C}$, before the relative dielectric permittivity (ϵ_r) was extracted using the following equation:

$$\epsilon_r = \frac{2\epsilon_{eff} - 1 + (1 + 12\frac{h}{W})^{-0.5}}{1 + (1 + 12\frac{h}{W})^{-0.5}} \tag{3.6}$$

, where h = $125\,\mu\mathrm{m}$, W = $0.3\,\mathrm{mm}$ are the thickness of the substrate and the width of the

Figure 3.2: Inkjet-printed flexible linear antenna array

printed lines, respectively. The results (shown in fig. 3.3) show good agreement with the datasheet values, and displayed losses in the order of $1.17\,\mathrm{dB\,cm^{-1}}$ for the lines.

Finally, copper tape was carefully stuck onto the back of the substrate to create a ground plane. The antenna array was then interfaced with end-launch connectors, from Southwest Microwave, and measured using an Anritsu 37369A VNA. Measurement results, as well as its simulation counterparts, are shown on fig. 3.4. Measurements feature a very good agreement with simulation, with visible differences on the vertical polarization (with reference to a vertically aligned array), attributed to slight imperfections in the $90\,\mathrm{deg}$ microstrip feed turns connecting the port to the associated antenna tree. That being said, the two ports offer a co-matching (two port being simultaneously matched) of better than $-17\,\mathrm{dB}$ at $31\,\mathrm{GHz}$, demonstrating, as a consequence, the readiness of the component for use in the complete Van-Atta array structure.

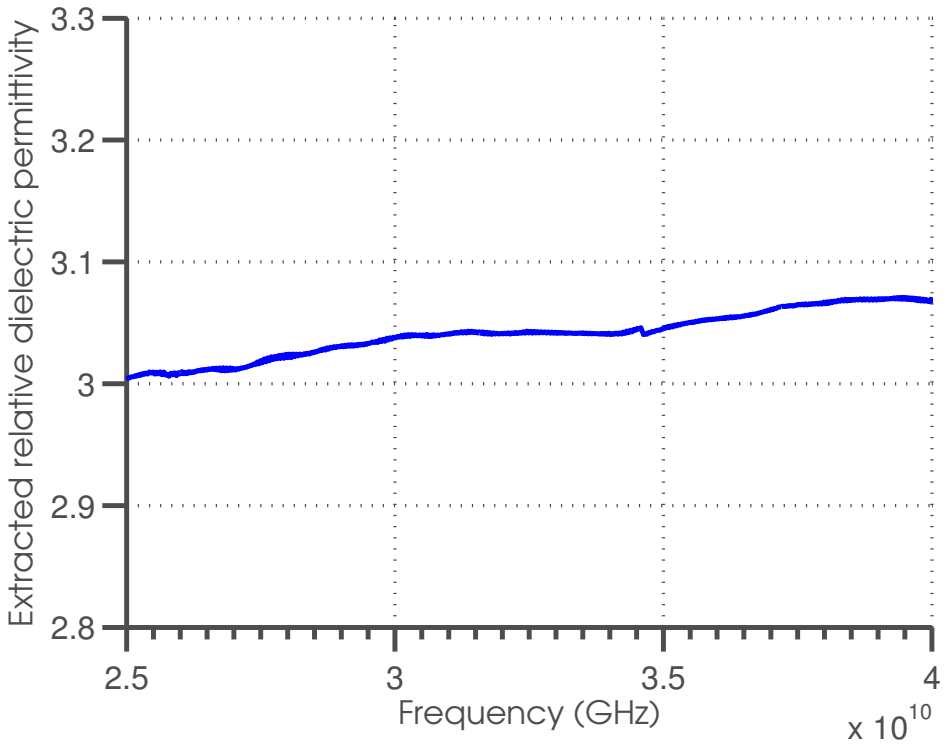

Figure 3.3: Dielectric relative permittivity of 5-mil Kapton HN, extracted from the measured data

3.2.2 Van-Atta reflectarray

A Van-Atta reflectarray structure (fig. 3.5) was designed and fabricated, by placing five of the previously-described series-fed linear antenna arrays side by side, with two of the linear antenna arrays rotated by 180° in order to optimize design compactness, connected in such a way for the re-emitted waves to be in-phase in the direction of the impinging interrogation signal (as described in section 3.1.2), and cross polarized with respect to the impinging wave. This was done by connecting the ports of each linear antenna array to the opposite polarization port of the symmetrical antenna (with respect to the center axis of symmetry of the structure), using microstrip transmission lines of controlled electrical lengths. In the configuration chosen here, half of the linear antenna arrays were flipped relative to those on the other side, in order to reduce the length of line lengths required to connect the antennas. However, as a consequence, vertical polarization feeds on the

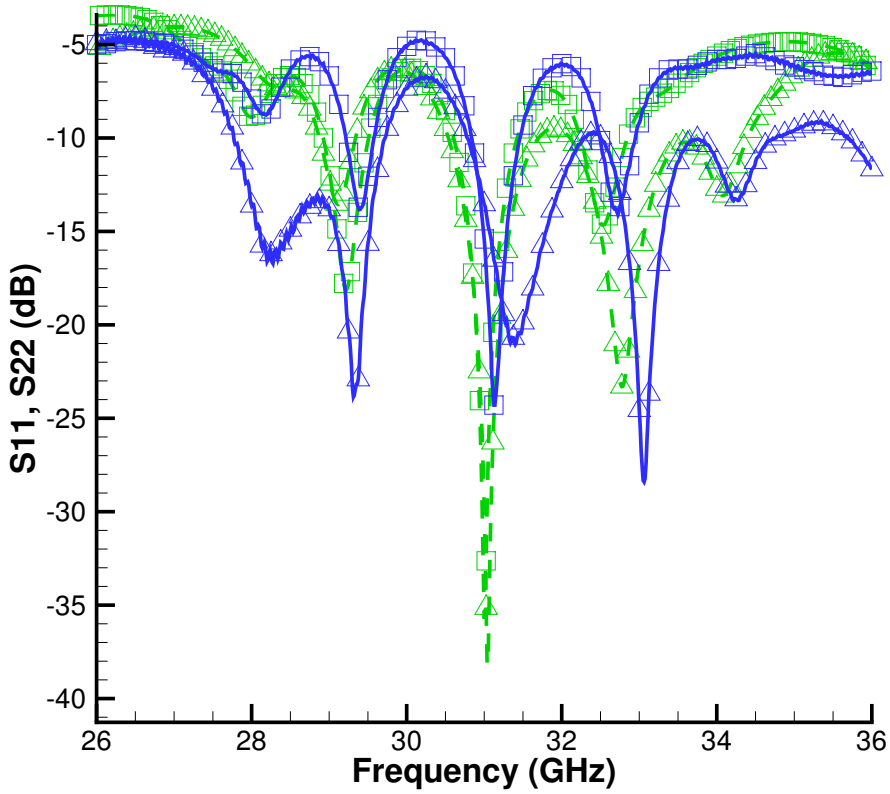

Figure 3.4: Measured (blue solid) and simulated (green dashed) return loss for the horizontal (triangle) and vertical (rectangle) polarization feeding ports of the series-fed patch antenna array

left of the array serve the top of the patches, while those on the right are fed from the bottom. This creates π phase-shift between the waves received by right-side and left-side antennas, in this polarization, while horizontal polarization ports are consistently fed from the same side. The induced π phase shift was therefore compensated for in the connecting network. It should also be noted that this cross-polarizing configuration enables the use of a central, self-connected, linear antenna array, which provides an optimal re-emission efficiency, thanks to its minimal connecting line length.

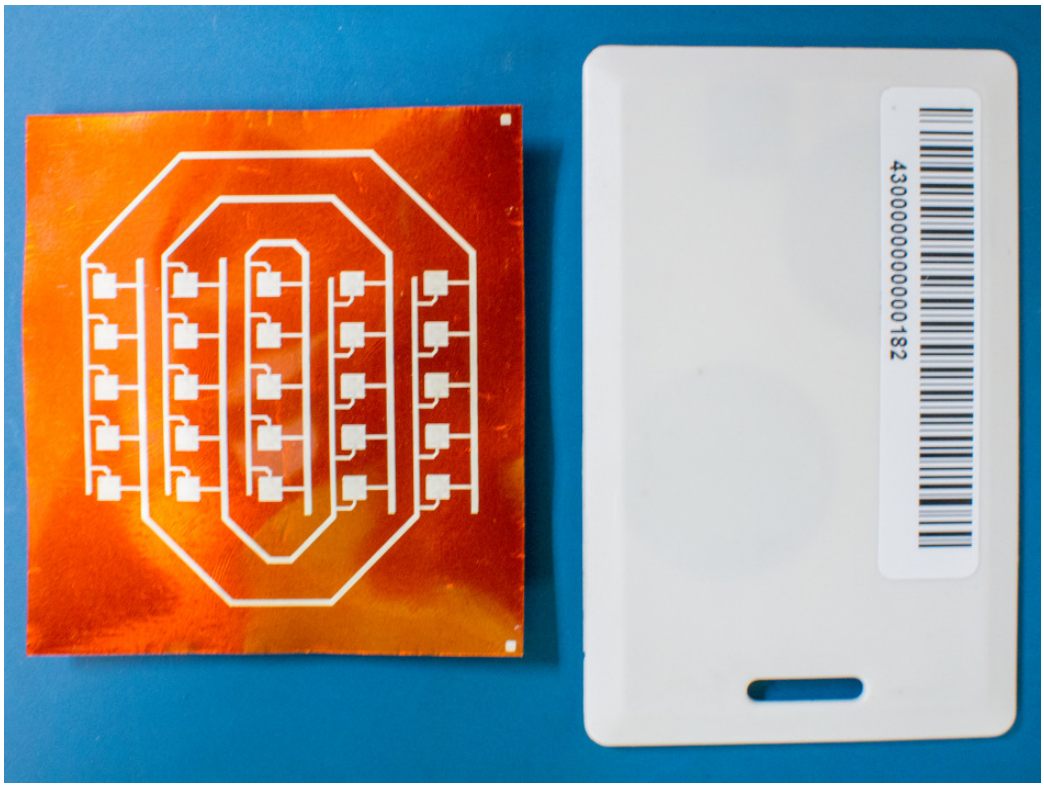

Figure 3.5: Inkjet-printed flexible Van-Atta reflectarray prototype, next to a standard ”credit-card” size RFID tag package

3.3 Characterization of the reflectarray

3.3.1 Planar configuration

Unlike most structures, which offer at least one interfacing waveguide port, reflectarrays can only be characterized by their reflection properties or, equivalently, their monostatic (both emitter and receiver in same position/direction, relative to the tag) or bistatic (emitter and receiver in different directions) RCS. In order to obtain optimal characterization measurements, the reflectarray tag was positioned inside a small anechoic chamber (and therefore backed with pyramidal RF absorbers) and was interrogated from the outside f the chamber at a range of $2.5\,\mathrm{m}$. The received signal of interest is cross-polarized with respect to the emitted signal and the measurement was therefore carried out using two cross-polarized antennas connected on both ports of a VNA. In the case of an anechoic

environment, the measured response is comprised of three major components:

$$y = G\left[s + r_{g,X-pol} + 2 * I_{X-pol} * r_{g,co-pol}\right] \tag{3.7}$$

, where s is the cross-polarized array response and therefore the signal of interest, I_{X-pol} the cross-polarization isolation of the used antennas couple, G the antennas gain, and $r_{g,X-pol}$ and $r_{g,co-pol}$ the cross-polarized and co-polarized responses of the rectangular metallic plane that forms the ground of the device. The factor 2 multiplier of the isolated signal accounts for the main emitted polarization emission signal response received on the secondary-polarization of the receiving antenna, as well as for the secondary-polarization emitted wave received on the main polarization of the receiving antenna. The cross-polarized RCS of a metallic plane is generally far smaller than the RCS response of the array. On the other hand, the same cannot be said about its co-polarized response which can be several orders of magnitude higher. The co-polarized maximum RCS (in boresight) of a rectangular ground plane can be approximated by:

$$r_{ground,X-pol} = 4\pi \left(\frac{WL}{\lambda}\right)^2 \tag{3.8}$$

, where W and L are the width and length of the rectangular metal plane, respectively. Given the device dimensions ($5\,\mathrm{cm} \times 5\,\mathrm{cm}$), this signal can, here, be on the order of $-1\,\mathrm{dBsm}$, which, as we will see, is quite significant. Therefore, high cross-polarization isolation of the antennas used for the measurement is paramount. As a consequence, two conical horn antennas with $19\,\mathrm{dB}$ gain and $40\,\mathrm{dB}$ cross-polarization isolation were used for the reflectarray's interrogation. A $20\,\mathrm{dB}$ gain amplifier was added on the emission channel, to increase signal level, and the monostatic RCS of the tag/array was measured for different angles of incidence, with respect to normal. Finally, a 12-inch sphere was measured in the same configuration (but by rotating one of the antennas in order to measure its co-polarized response), to establish a reference RCS. The link budget of the characterization channel

can be expressed by eq. (3.2) or, if all conditions are kept identical, more succinctly as:

$$P_r = C\sigma \tag{3.9}$$

, where C is a constant in constant conditions. Metallic spheres are remarkable targets, which, due to their spherical symmetry, display a constant RCS, regardless of the impinging-wave's angle of incidence. This RCS can–in the optical limit where $\frac{2\pi a}{\Lambda}$ (about 8200, here) is much greater than 10–also simply be expressed as $\sigma_{sphere} = \pi a^2$, where a is the radius of the sphere. Once the power received by the reader due to re-emission by the sphere ($P_r, sphere = C\sigma_{sphere}$) is measured, the response of the tag can readily be calibrated and its RCS be obtained from:

$$\sigma = \frac{P_{r,tag}}{P_{r,sphere}}\sigma_{sphere} \tag{3.10}$$

It should be noted that the $2.5\,\mathrm{m}$ range was chosen in order to provide high measured signal responses, while allowing the sphere to fit entirely into the reader antennas' main lobes, for adequate calibration. The data was also time-gated to remove any cross-talk between the antennas from the response. The measured RCS of the reflectarray, as well as its simulation counterpart are shown in fig. 3.6. The measured and simulated (achieved using Ansys HFSS) results show very good agreement, and both display the expected Van-Atta behavior. Indeed, the RCS of the tag only changes by, at most, $10\,\mathrm{dB}$ over a range of $140°$ around boresight: the structure displays both a high (up to $-26\,\mathrm{dBsm}$) and interrogation-angle-robust RCS.

3.3.2 Curved configurations

As a flexible conformable mm-wave reflectarray, variations of the tag response with bending can be of concern. The reflect-array was therefore characterized in various bending configurations, starting with uniform bending around cylinders of various radii whose axes

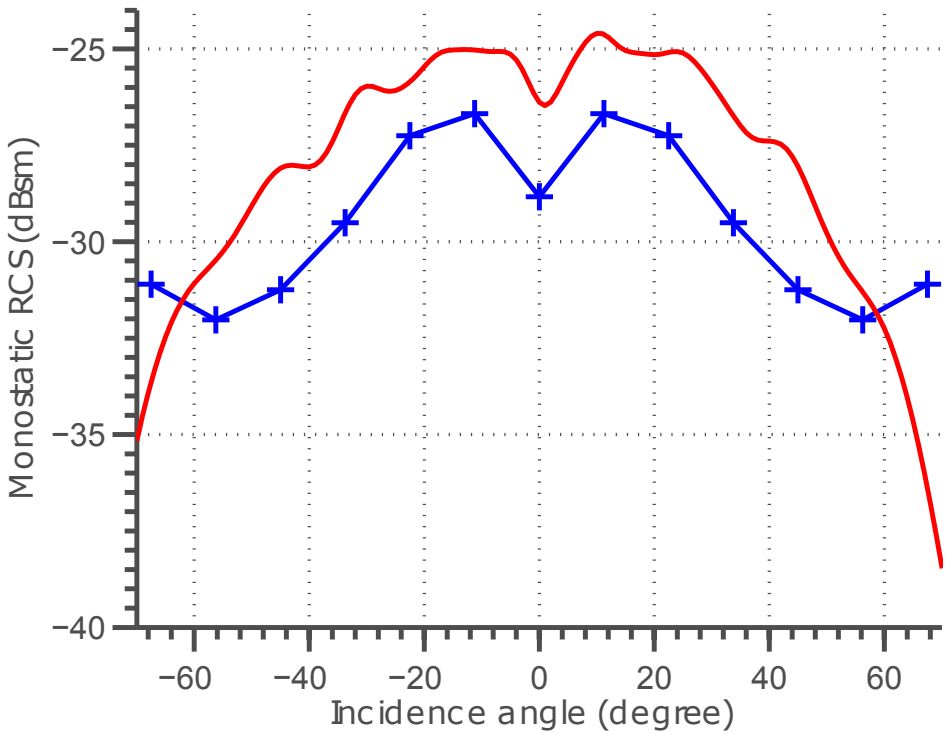

Figure 3.6: Measured (blue +) and simulated (red solid) monostatic RCS of the Van-Atta reflectarray

were kept parallel to the linear antenna arrays of the tag and perpendicular to the axis of rotation used to vary the angle of incidence of the interrogation in what I will later refer to as the "parallel" configuration. In the "perpendicular" characterization configuration, by contrast, the linear antenna arrays of the tag remain perpendicular to the axis of rotation used to vary the angle of incidence of the interrogation but the axis of the various cylinders used to bend the tags are now set perpendicular to the linear arrays.

In the "parallel" configuration, the observed RCS variations (shown in fig. 3.8) are quite modest and are comprised of two effects:

- A slight reduction in the range of Van-Atta retrodirective behavior, with a sharper decrease of the response at angles further away from boresight. The curvature detunes the reflect-array by adding an additional phase shift in the waves received by complementary antennas (with reference to the center of the array). Indeed, by con-

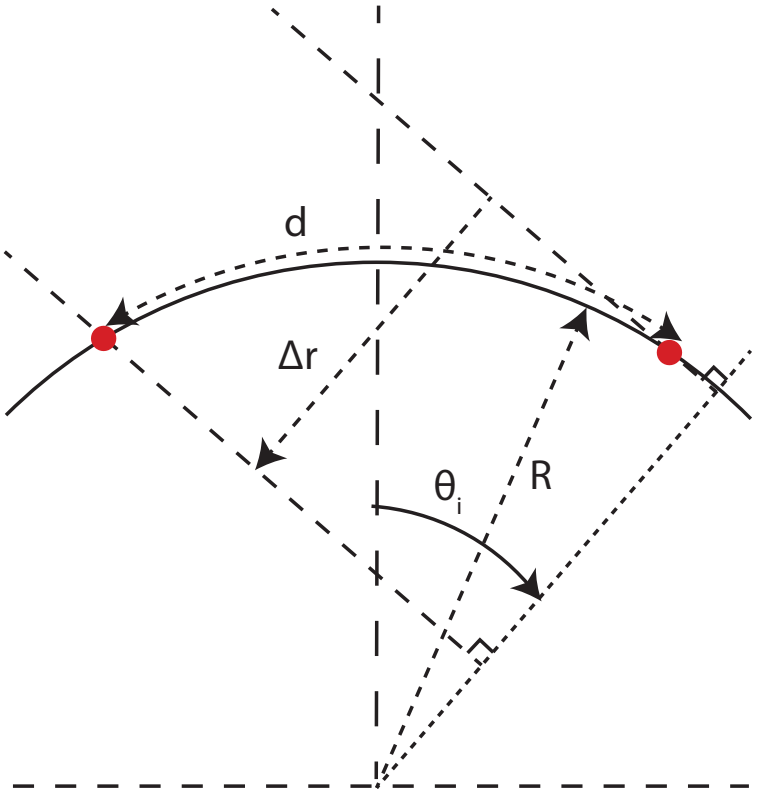

Figure 3.7: Geometrical model considered for curvature-induced phase-shift calculation

sidering point-located antennas, and an array covering no more than a $180°$ angle of the cylinder's surface (as shown in fig. 3.7), it can be found that the difference in path lengths, with an impinging wave arriving with an angle θ_i from normal, can be expressed as:

$$\Delta r = \frac{4\pi R}{\lambda} \sin\left(\frac{d}{2R}\right) \sin(\theta_i) \tag{3.11}$$

, where R is the curvature radius and d the distance (on the planar array) between the connected antenna pair. As a consequence, the phase difference introduced by the curvature (with respect to the flat case) can be expressed as:

$$\Delta\phi = \left(-\frac{2\pi\Delta r}{\lambda} + \frac{2\pi d}{\lambda}\right)\sin(\theta_i) \tag{3.12}$$

$$= \frac{2\pi}{\lambda}\left(d - 2R\sin\left(\frac{d}{2R}\right)\right)\sin(\theta_i) \tag{3.13}$$

, where λ is the wavelength. In the worst case considered here ($R = 7.62\,\mathrm{cm}$) for the outer antenna pair ($d \approx 5\lambda = 5\,\mathrm{cm}$), the maximum phase-shift (at $\theta_i = 70°$) is equal to $\Delta\phi = 0.168\pi$. This value is quite negligible: such a small value does not induce a large change in the array factor, and is also far larger than that introduced for closer pairs and at lower incidence angles.

- A reduction in the overall RCS. This can be explained as a consequence of the angle-dependent gain of the patch antennas that form the reflectarray. The incidence angle direction moves away from the patch antennas boresights as the curvature increases, which contributes in flattening out the RCS response, from the center. This is the main effect observed in fig. 3.8.

In a second experiment, the tag was characterized in the "perpendicular" bending configuration. The results, shown on fig. 3.8, show a remarkably different behavior than that observed in the "parallel" configuration: the overall RCS is reduced by a significant amount, and displays a quite irregular shape. Measurements with such curvature axes also stand out by their particularly high interference floor. This is caused not by the array structure itself, but by its ground plane. Indeed, when curved with an axis on the plane formed by the tag and the interrogation antennas, the currents created on the curved surface of the ground conductor create a large cross-polarized response, which then becomes significant enough to non-negligibly interfere with the measurement capability of the system. That being said, this effect is general to all grounded polarity-rotating designs, and might be resolvable through the use of ground edge patterning techniques.

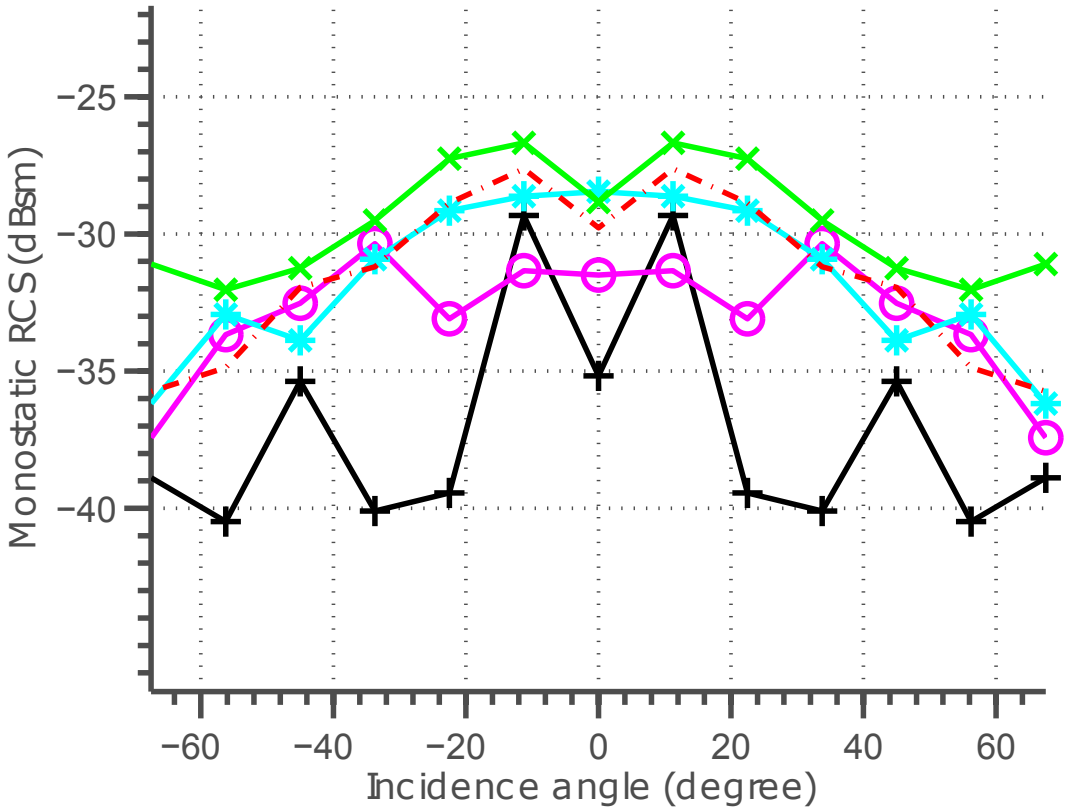

Figure 3.8: Measured RCS for flat (green x), parallel-axis-curved with radii of 5 (red dash point), 4 (blue stars), and 3 inches (magenta circles), and horizontal-axis-curved with 5 inch radius (black +).

The original discussion of section 3.1.1 where the theoretical benefits of higher frequency operation were laid out relied on unknown aperture efficiencies, $e_{a,r}$ and $e_{a,t}$. Using the measurements of this section, we can now calculate the effective link budget gain relative to results reported in the literature, at lower frequencies. Combining eq. (3.2) as well as eq. (3.1) yields:

$$P_r = P_e F_t^2 \frac{A_r^2 e_{a,r}^2}{4\pi R^4} \frac{\sigma}{\lambda^2} \tag{3.14}$$

The relative increase in link budget relative to a lower-frequency-operating identically-sized UHF system can be expressed as:

$$G_{LB} = \frac{\sigma}{\sigma_{UHF}} \left(\frac{\lambda_{UHF}}{\lambda} \right)^2 \tag{3.15}$$

Using the maximum RCS of the array (up to $-26\,\mathrm{dBsm}$), compared with the $-13\,\mathrm{dBsm}$) a UHF RFID folded dipole configuration [104] with about 5 times the aperture of the reported tag, the achieved gain is on the order of G_{LB} = $17\,\mathrm{dB}$.

3.4 Optimal signal processing for long range multi-tag interrogation

In addition to a high performance physical tag structure, which provides an unequaled combination of low cost, flexibility, cross-polarized response, and high and isotropic RCS at millimeter-wave frequencies, high frequency operation enables the implementation of optimal reading schemes, in order to provide high-resolution time-frequency multi-tag long range detectability. This section reports new techniques that were developed for the detection of chipless RFIDs by exploiting the advantages of higher frequency operation described in section 3.1.1.

3.4.1 Data processing scheme for high-performance range and resonant-frequency-based identification

The approach described in the following section relies on the combination of a spectrogram scheme with matched filtering. The response of the tag was first characterized in an interference-modest anechoic environment before the known response was used for its recognition and detection in much more challenging conditions. This matched-windowing spectrogram methodology allowed, for the first time, the localization and adequate signal extraction and detection at long range without the need for environmental calibration. A step-by-step flow chart of the entire data processing scheme can be seen in fig. 3.9. It should be noted that this process does not require a measurement of the background response and its extraction, as is done in many reports, such as [105].

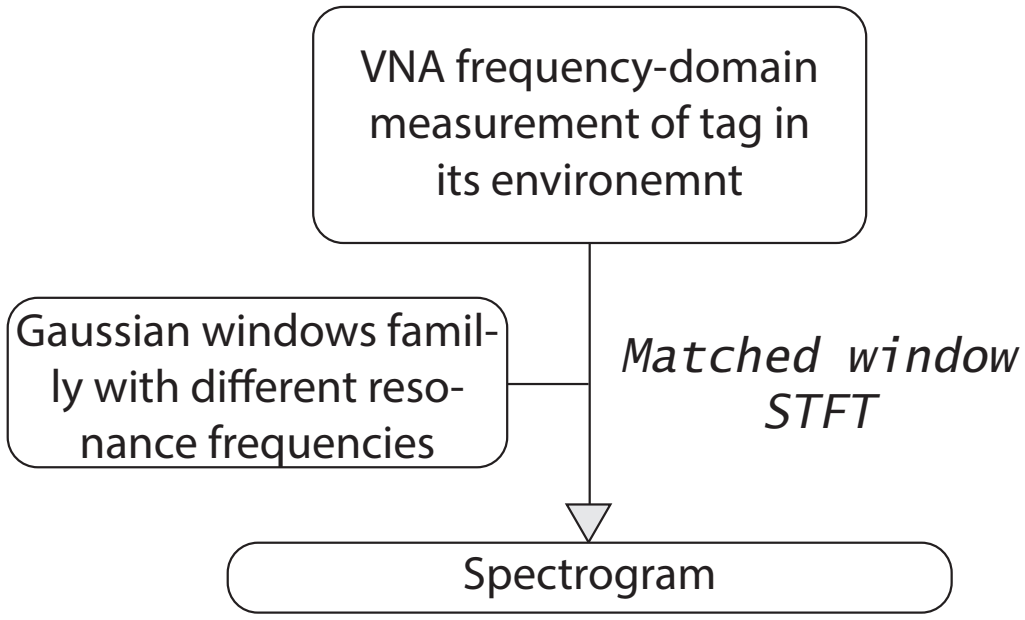

Figure 3.9: Processing steps of the measured data for high-performance resonant frequency and range extraction

For high performance signal extraction in both time and frequency dimensions, a short time Fourier transform (STFT) where the windowing function is identical to the expected signal (as described in [106]), was used to process the received response. In the experiments described later in the section, the reference response was measured in frequency domain, using a VNA, as the S_{21} from the emitting antenna to the receiving (cross-polarized) antenna. The (n_t, n_f, k_t, k_f) used in this section are integer indices that span $[\![1; N]\!]$, where N is the number of measured frequency points. The frequency-response S_{21} complex data vector $r(k_f)$, exported from the measurement equipment, was then processed through a IFFT to extract the time-domain response of the system $r(k_t) = \mathrm{IFFT}\,[r(k_f)]$. Through the IFFT, N discrete frequency points in the (f_{min}, f_{max}) range, with steps Δf, map to a set of time points in the $(t_{min} = 0, t_{max} = N\Delta t)$ range with increment $\Delta t = \frac{1}{N\Delta f}$. A STFT can then be applied in the following way:

$$STFT(n_t, n_f) = \sum_{k_t=0}^{N} r^*(k_t) w(k_t - n_t, n_f) e^{-2i\pi n_f k_t} \tag{3.16}$$

, where $w(k_t, l_f)$ is the time-frequency response of the applied window, $STFT(n_t, n_f)$

the output signal, and $r(k_t)$ the measured data, in time-frequency-domain, which may be modelled as the following combination:

$$r(k_t) = s(k_t) + i(k_t) + n(k_t) \tag{3.17}$$

, where $s(k_t)$ is the Van-Atta tag's response signal, $i(k_t)$ the interference contributed by the environmental clutter and antenna cross-talk, and $n(k_t)$ the noise. In the cases of the experiments described in this chapter, a complex signal was measured in frequency domain, using a VNA. While the magnitude of the signal encloses the frequency information, its phase (though Fourier transform) allows for the retrieval of time-delay information, a feature that will be exploited later on. In this configuration, optimal detection can be achieved through the use of a window function that is identical to the expected signal, $s(k_t)$. In our configuration, we assume a constant relative bandwidth for the Van-Atta array, regardless of its resonance frequency. As a consequence, the absolute bandwidth of the received signal $s(k_t)$ depends on the (unknown) resonance frequency of the array. Therefore, contrary to usual STFT implementations, the window is made frequency dependent: the absolute bandwidth of the filtering window is changed for each different center frequency, while its relative bandwidth is conserved.

In order to find the shape of this optimal window, the intrinsic response of the array, isolated from the environmental interference found in real-world configurations, was characterized. In order to do so, the frequency-response of the array was measured in the anechoic chamber, at close range (about $1\,\mathrm{m}$) for optimal accuracy and fitted with a Gaussian function in frequency domain (shown in fig. 3.10. The time origin and relative bandwidth of the function were shifted to fit the measurement using a least square optimization approach. A family of such functions, with different center frequencies ($f_0(n_f)$) and assuming identical relative FWHMs ($FWHM_r = \frac{FWHM}{f_0(n_f)} = 0.0417$) and identical powers was then created:

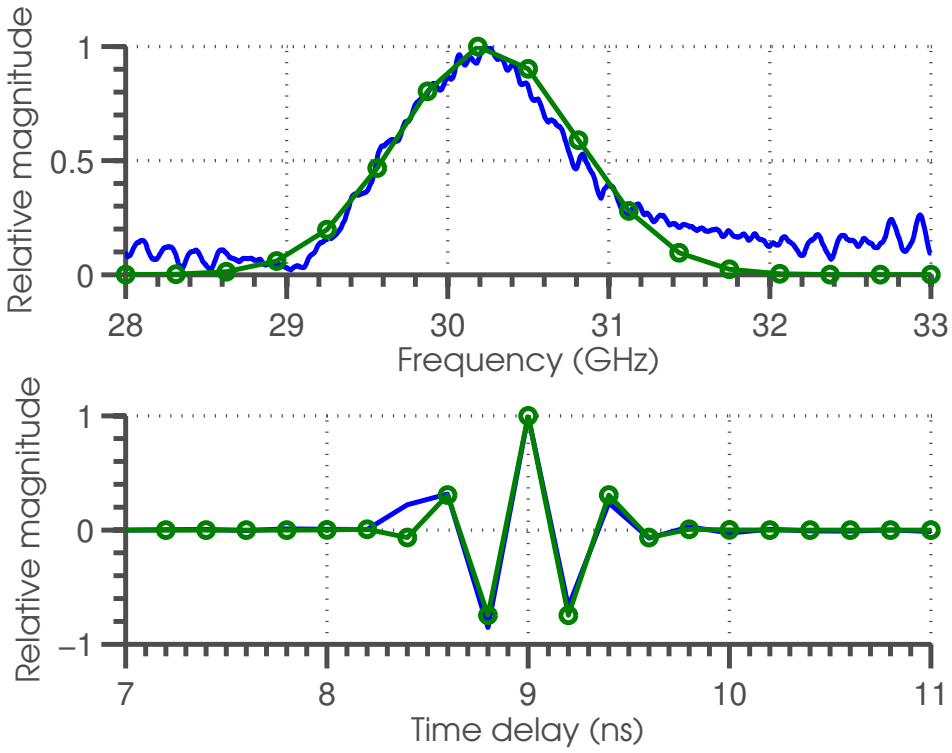

Figure 3.10: Measured array response (blue) and fitted Gaussian used as matched window (green circles), plotted in time and frequency domains

$$W(k_f, n_f) = \frac{1}{\sqrt[4]{\sigma(n_f)^2\pi}} e^{\frac{-\left(f(k_f)-f_0(n_f)\right)^2}{2\sigma^2(l_f)}} \tag{3.18}$$

where

$$\sigma(n_f) = \frac{f_0(n_f) * FWHM_r}{2\sqrt{2\ln 2}} \tag{3.19}$$

$f_0(n_f) = f_{min} + n_f\Delta f$ and $f_0(k_f) = f_{min} + k_f\Delta f$.

The time-domain response of the window was then obtained through IFFT, with

$$w(k_t, n_f) = \mathrm{IFFT}_{\mathrm{k_f}}\left[W(k_f, n_f)\right] \tag{3.20}$$

where '$\mathrm{IFFT}_{\mathrm{k_f}}$' is the inverse fast Fourier transform operation, applied along the dimension of indice k_f.

Then, the summation of eq. (3.16) was applied, before the spectrogram was obtained from the the squared magnitude of the STFT:

$$S(n_t, n_f) = |STFT(n_t, n_f)|^2 \tag{3.21}$$

The result of such a process, applied to the measurement data shown in fig. 3.10, is displayed in fig. 3.11. On the following spectrograms, the response is expressed as a function of range, where the range is extracted from the round trip time $R = \frac{ct}{2}$, where c is the speed of light in vacuum and t the time-delay of the vector point. It is apparent that this processing scheme enables the extraction of both time delay (range) and frequency information from the tag.

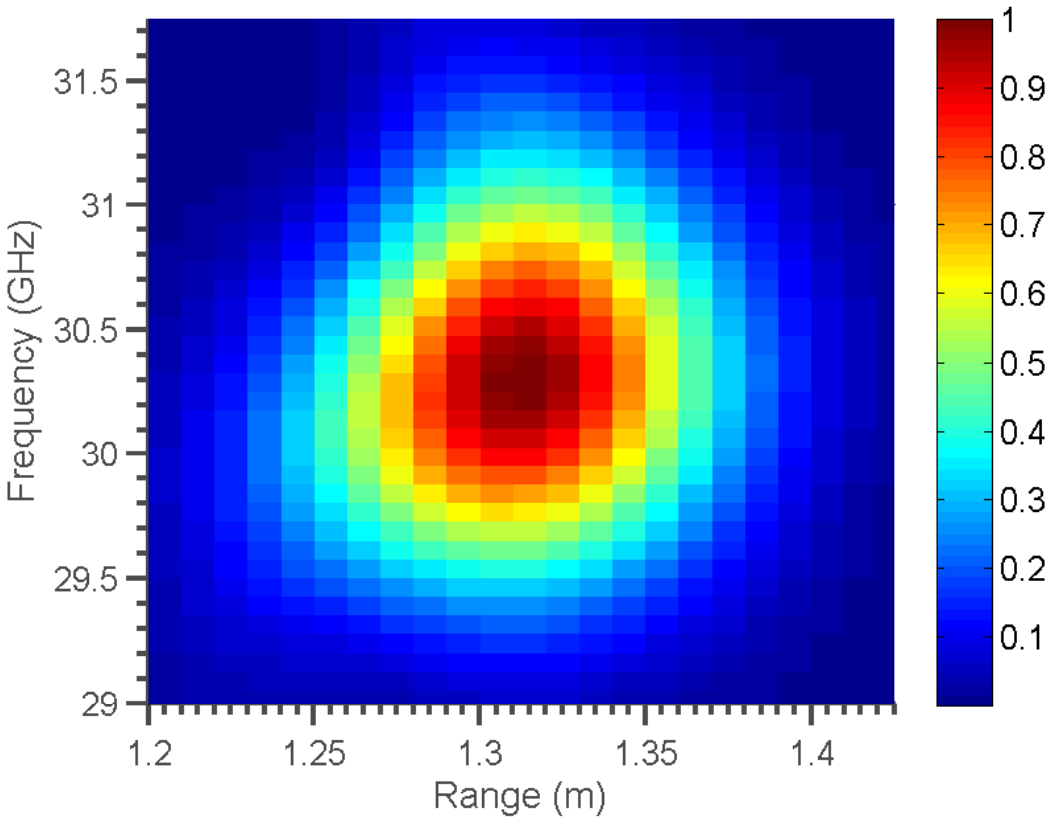

Figure 3.11: Spectrogram of the measurement in the configuration shown in fig. 3.10

3.4.2 Multi-tag detection

As previously mentioned, mm-wave frequencies allow for the ready use of high absolute frequency bandwidths and therefore enable the ability to resolve responses in the time domain (and therefore, range) with high accuracy. Indeed, from a time/frequency resonance detection perspective, the frequency (Δf) and time (Δt) resolutions of a data set (where frequency and time data are related by FFT and IFFT) obey the following constraint:

$$\frac{1}{N} = \Delta t \Delta f \tag{3.22}$$

$$= \Delta t \left(\Delta f\right)_r f_0 \tag{3.23}$$

where N is the number of measured data points, f_0 the center frequency of interest, and $\left(\Delta f\right)_r$ the relative frequency resolution. For a given $\left(\Delta f\right)_r$ (constant for frequency-scaled identical structures) and for a given number of samples, time-resolution increases by an f_0 factor. Not only can a single tag now be located with precision, but this process also opens broad opportunities for multi-sensor and multi-sensing configurations as a result of its ability to resolve tags which may be adjacent in either range of resonant frequency. Indeed, for a usual Gaussian frequency tag response, the measured frequency (σ_f) and time (σ_t) half-power bandwidth (HPBW) of the FT-related responses are constrained by:

$$\frac{4ln2}{\pi} \leq \sigma_t \sigma_f \tag{3.24}$$

$$\leq \sigma_t \left(\sigma_f\right)_r f_0 \tag{3.25}$$

where σ_f and σ_t are the measured frequency and time half-power bandwidth (HPBW) of the responses and $\left(\sigma_f\right)_r$ is the relative HPBW.

$$\frac{4ln2}{\pi} \leq \sigma_t \sigma_f \tag{3.26}$$

$$\leq \sigma_t \left(\sigma_f\right)_r f_0 \tag{3.27}$$

where $\left(\sigma_f\right)_r$ is the relative HPBW. As a practical consequence, the theoretical minimum delay and/or relative frequency differences required in order to differentiate two tags, adjacent in resonance frequency and/or delay, decreases linearly with an increased operation frequency. In the measurement shown on fig. 3.11, these values were measured as $\sigma_t = 0.67\,\mathrm{ns}$ and $\sigma_f = 1.43\,\mathrm{GHz}$, with $\sigma_t \sigma_f = 1.08 \frac{4ln2}{\pi}$, displaying only an $8\,\%$ increase from theoretical ideality.

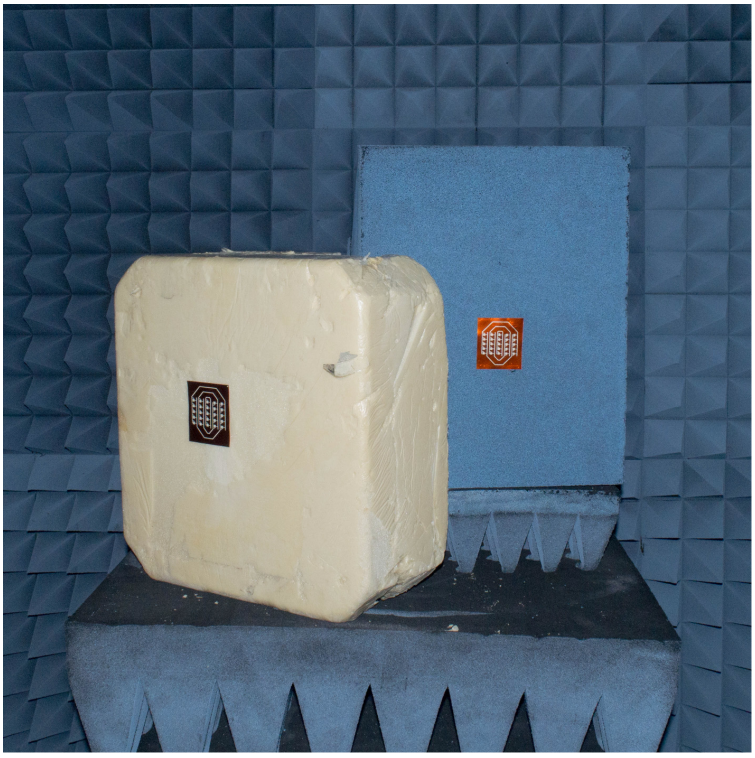

Figure 3.12: Target measurement configuration for dual-tag detection demonstration

In order to demonstrate the multi-tag detection capability of this approach, a second tag, with a $35\,\mathrm{GHz}$ resonant frequency was fabricated. Both tags were then set side-by-side (fig. 3.12) and interrogated with the same configuration as described in section 3.3. The

processed result of this test can be seen in fig. 3.13.

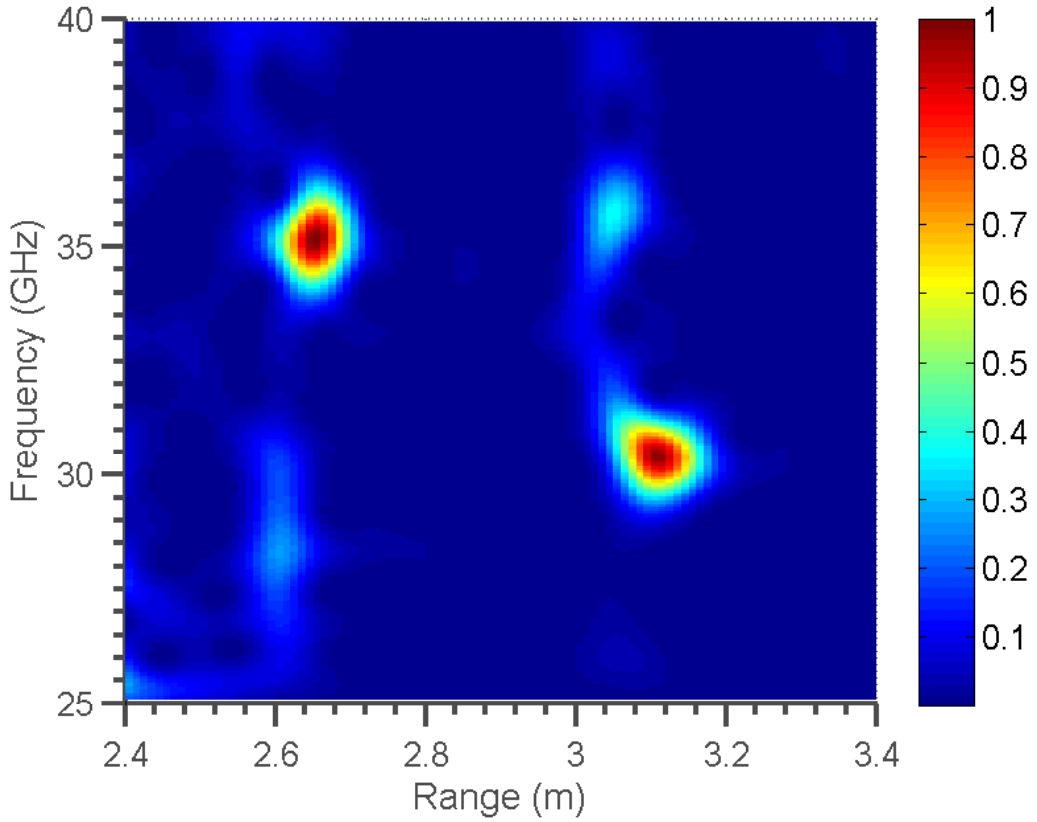

Figure 3.13: Spectrogram of the measurement in the multi-tag configuration shown in fig. 3.12

As expected, both tags are extremely well resolved in time, as well as in resonant frequency. This demonstrates the capability of the system for high-density range and/or frequency divided multi-tag implementations. Unlike any other chipless RFID reported reading methods, this scheme allowed for the individual detection of several tags with identical or otherwise unresolvable resonance frequencies, but positioned at different ranges. Range differences can either be introduced by their different locations or by the use of delay lines in tag structures. The same reasoning, of course, also applies to tags with identical ranges but different resonance frequencies. Therefore, the identity of each tag is encoded in a combination of its resonance frequency, its range, and its direction, whose highly-resolved estimation can be, in principle, enabled by the easily-achieved high directivity of reader

antennas at these higher frequencies. Using the popular bit-by-bit encoding scheme [107], each Van Atta array could be used to encode 1 bit of information. However, while bits are usually spread only over the frequency spectrum, the presented Van Atta implementation allows for their distribution over both time-delay and frequency domains. An assembly of N Van Atta array tags would therefore be able to encode N bits, where each bit is associated with a unique (t_i, f_i) time-delay frequency couple. This therefore allows the implementations of much denser tag constellations using two differentiating physical properties (freqnency and time-delay) versus the single frequency dimension usually relied upon,

3.4.3 Ultra-long-range detection

As extensively argued in section 3.1, one of the main appeals of the proposed device and approach is the high detectability and, incidentally, ultra-long expected range. In order to test this promise, a high performance antenna system, comprised of the same conical horn antennas used for the previously reported measurement, a 300mm-diameter dielectric lens (for high directivity), and an inkjet-printed mm-wave polarizer was assembled, as shown in fig. 3.14.

An amplifier with a gain $20\,\mathrm{dB}$ was added on the receiving channel, in order to increase the signal level. The output power of the Anritsu 37369A VNA used for the measurement was set at $-10\,\mathrm{dBm}$ which, with a theoretical maximum gain of the lens antenna of $G_{max} = \frac{4\pi^2 R_{lens}^2}{\lambda^2} = 39.48\,\mathrm{dB}$ (where R is the radius of the lens), keeps the equivalent isotropic radiated power (EIRP) under $1\,\mathrm{W}$. This reading system was then set-up indoors, in a real environment, and aimed at a Van-Atta target, at a range of $30.5\,\mathrm{m}$ (confirmed with a laser ranging system), in the configuration shown in fig. 3.15, with a link budget, calculated from eq. (3.2), of:

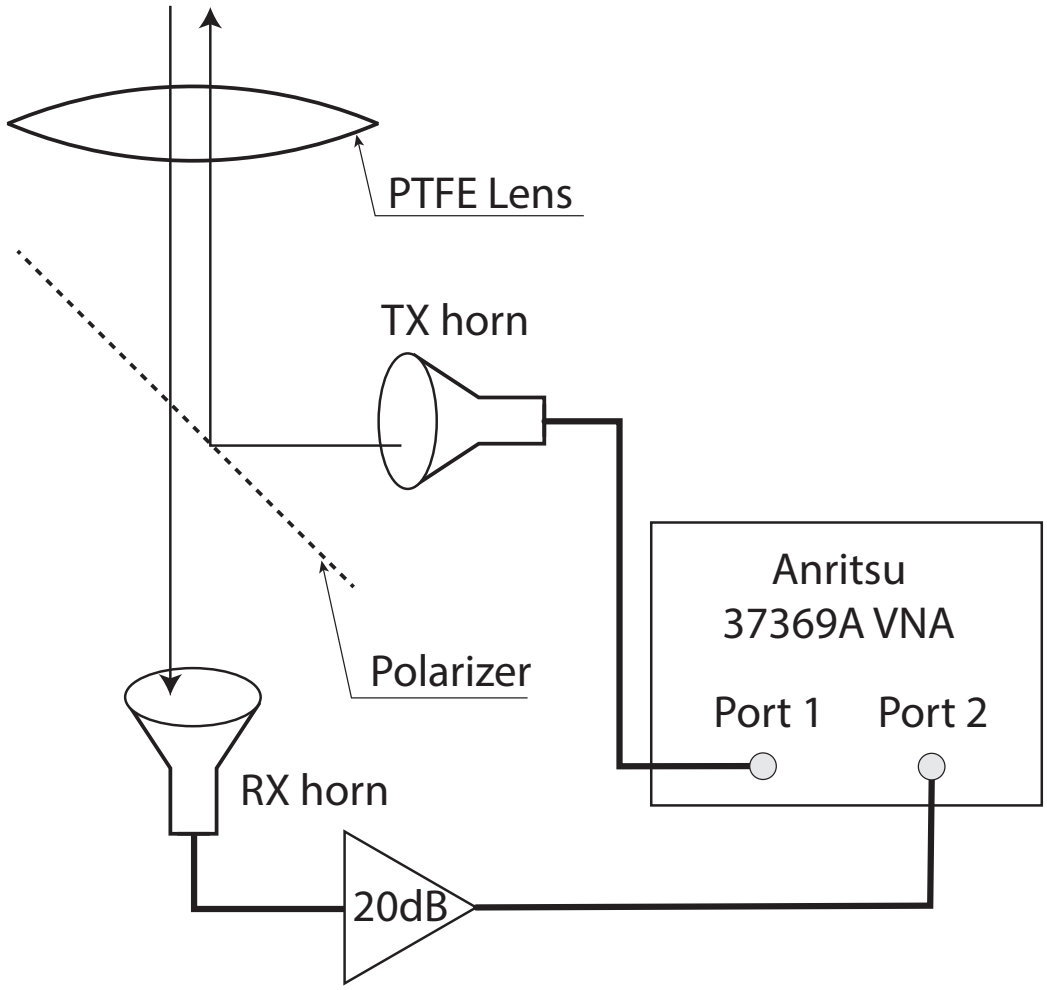

Figure 3.14: Schematic of the reading system used for the measurement shown in fig. 3.15

$$P_r = P_e e_{a,r}^2 A_r^2 \frac{\sigma}{4\pi\lambda^2 R^4} \tag{3.28}$$

$$= -108\,\mathrm{dBm} \tag{3.29}$$

, where $P_e = -10\,\mathrm{dBm}$, $A_r = \pi R_{lens}^2 = -11.5\,\mathrm{dBsm}$ (where $R_{lens} = 15.24\,\mathrm{cm}$), $\sigma = -27\,\mathrm{dBsm}$, $\lambda = 1\,\mathrm{cm}$, $R = 30.5\,\mathrm{m}$, and $e_{a,r} = -9\,\mathrm{dB}$. It should be noted that, at $30\,\mathrm{GHz}$, the atmospheric attenuation is on the order of $0.1\,\mathrm{dB\,km^{-1}}$ [108], and is therefore not included in the calculation. The received signal is then amplified by $20\,\mathrm{dB}$ before reaching the VNA.

The measured data was then processed according to the scheme displayed in fig. 3.9,

Figure 3.15: Measurement configuration at an interrogation range of $30.5\,\mathrm{m}$

and described in section 3.4.1, the output of which can be seen on fig. 3.16. Here, the peak is also easily extracted, and has HPBWs of $\sigma_t = 0.5\,\mathrm{ns}$ $\sigma_f = 1.9\,\mathrm{GHz}$. The lower signal level, noisier and more interference-prone environment contributed towards widening the frequency spread of the detected signal. That being said, the signal is still extremely resolvable; this suggests even longer range capabilities. This demonstrated range represents an improvement of at least an order of magnitude upon that of state-of-the-art chipless RFID devices and approaches.

3.5 Towards low-cost multi-parameter multi-sensor constellations

In section 3.4, the array tag, interrogated with a high performance reading system, and processed with optimal signal extraction methods, demonstrated its capability for long-

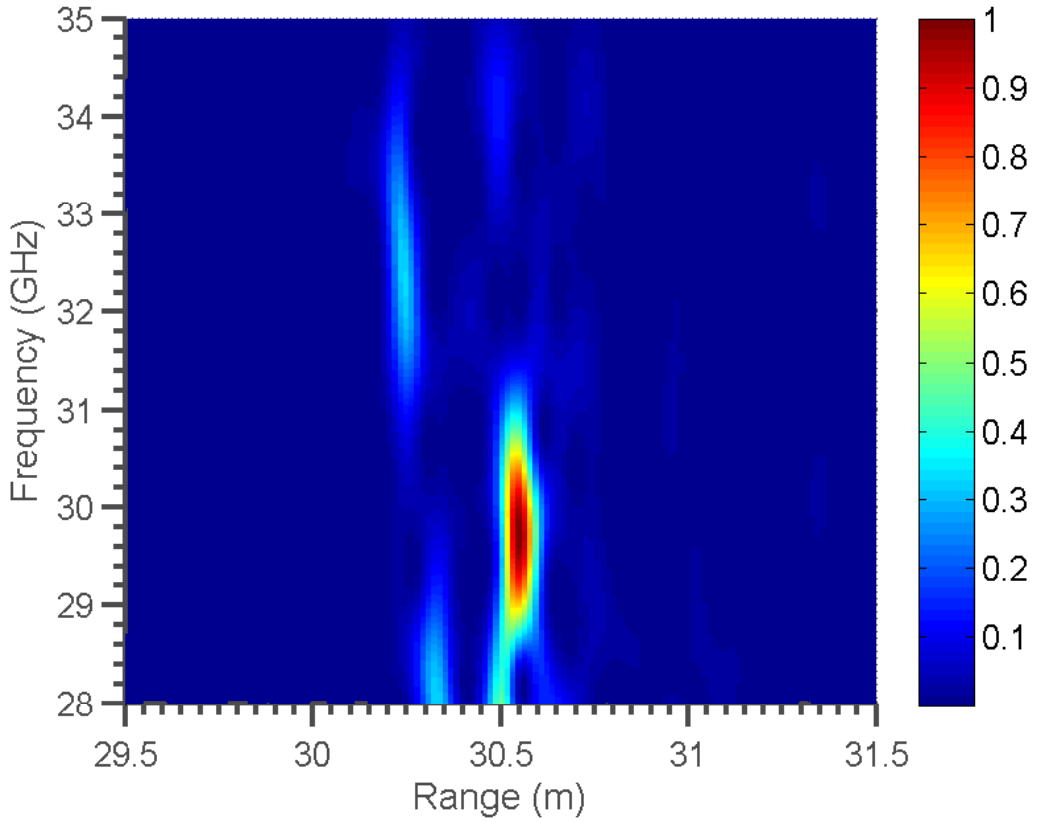

Figure 3.16: Spectrogram of the measurement in the long-range configuration shown in fig. 3.15

.

range high-density multi-device detection implementations in indoor environments. The proposed data processing scheme also allowed for the extraction of both range and resonance frequency information, with high accuracy. As it is, the system has already been demonstrated as capable of being applicable to range finding, as well as to time-delay and resonant-frequency-based tag identification. The capability of interrogating several tags, from a wide range of angles, also enables it with angle measurement capabilities, where the measured delay between two tags, placed on a surface at known distances from each-other, could be associated with an interrogation angle. Nevertheless, one of the main appeals of both time and resonant-frequency extraction lies in the potential implementation of high densities of resonance-frequency-shift-based chemical sensors. As presented in [109], the proposed array can also act as a humidity sensor, thanks to the relative hu-

midity (RH) dependent dielectric constant of the utilized Kapton HN substrate. In the real-environment configuration described in [109], the shift of resonance frequency with RH, reproduced on fig. 3.17, had been measured, and displayed remarkable linearity. The Kapton datasheet, from Dupont, describes the following law for the humidity-dependent permittivity (at $23\,^{\circ}\mathrm{C}$, for an unspecified frequency):

$$\epsilon_r(RH) = 3 + 0.008RH \tag{3.30}$$

, where RH is the relative humidity level, in $\%$. Assuming an array resonant frequency variation proportional to that of its constituting patch antennas $\left(\propto \frac{1}{\sqrt{(\epsilon_r)}}\right)$, the theoretical response of the array was plotted against the measured data (fig. 3.17). Both theoretical and measured responses show good agreement, therefore confirming that the main sensing mechanism relies on the humidity-dependent permittivity of the Kapton substrate. Thanks to its compatibility with additive manufacturing technologies, such as inkjet printing, the proposed sensor design could readily be printed onto other chemi-sensitive substrates, to provide multi-sensor multi-analyte long-range detection capabilities.

Finally it should be noted that the grounded design of the sensor offers two significant advantages for permittivity-based detection:

- The ground completely isolates the behavior of the sensor from potential supporting material influence. As a consequence, such sensors do not suffer from the typical detuning that can be observed with non-grounded structures.

- The electromagnetic field inside of the structure is mostly confined within the substrate. Therefore, any change of its material permittivity has a high impact on the resonant frequency of the sensor tag. Indeed, this configuration displays a relative sensitivity to humidity $\left(\frac{1}{f_0}\frac{\Delta f}{\Delta RH} = 1.41\right)$ that is almost 1 order of magnitude higher than of the state of the art of Kapton-based wireless humidity sensors [110].

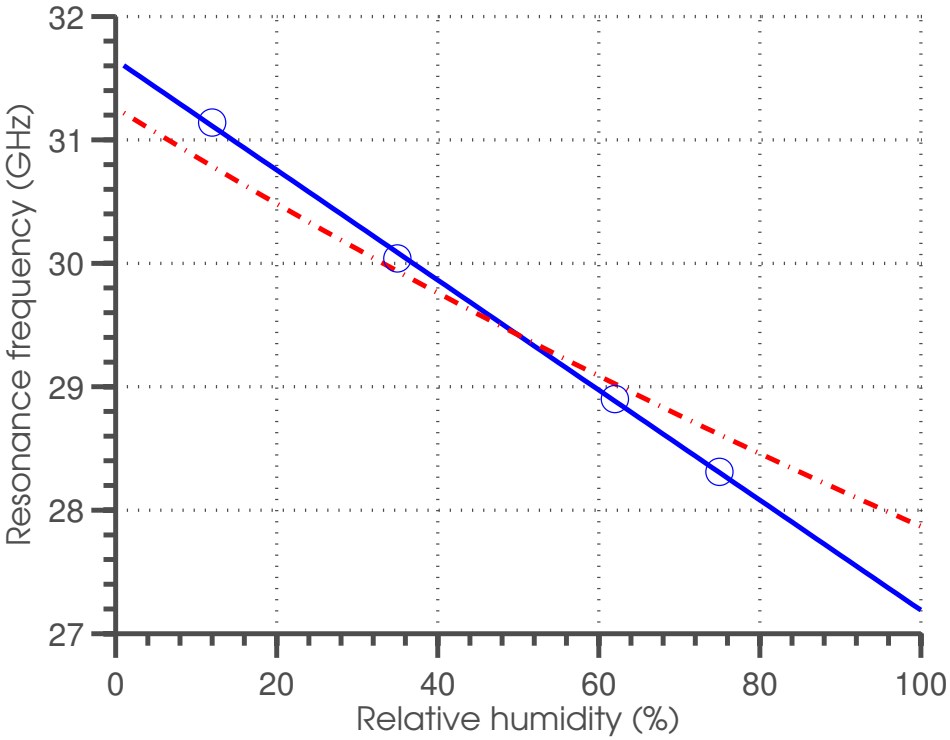

Figure 3.17: Plot of the measured resonance frequency of the inkjet-printed Van-Atta reflectarray as a function of the ambient humidity level (circles), its linear fit (blue line), and theoretical model prediction (red point dash)

CHAPTER 4

AN ULTRA-LONG-RANGE RFID SYSTEM OPERATING AT MM-WAVE BANDS

The work described in chapter 3 presented the use of a particular antenna system—a printed, flexible cross-polarizing Van-Atta reflectarray structure—for the demonstration of a chipless RFID system outperforming its art by more than one order of magnitude in reading range. This feat was a product of the combination of high RCS, polarimetric detection, and of a simple yet high-performance time-delay/frequency pattern detection algorithm.

Remarkably, the system was able to demonstrate this detection without having to resort to environment-calibration techniques, whereby two measurement of the environment—with and without the presence of the tag—are conducted and compared to deembbed all the static (in the terminology of wireless channels) interference created by environmental scattering. The environments in which these pairs of measurements are usually taken do not resemble any contexts encountered by wireless systems in practical operating conditions: these "frictionless" conditions are controlled to create wireless channels that are unrealistically static. Nevertheless, such chipless approaches suffer from limitations, which limit their versatility as wireless nodes and motes for practical applications:

- Even after an order-of-magnitude extension, the range can hardly exceed $50\,\mathrm{m}$ in LOS, even through the use of highly-advanced radar reading systems [111, 112]. This limit greatly increases the density of readers needed to service a given environment, and the associated infrastructure costs.

- The sensing ability stems from the influence of ambient conditions or analytes on the mm-wave properties of the material that constitute the tag. The development of new module for a different target cannot, therefore, rely on existing components whose integration could readily sensitize the tag towards a different analyte. Instead, each

tag needs to be redesigned using one or several materials whose properties at the operating frequency of the tag are known, and whose variations with respect to their exposure to the new analyte are well characterized.

Despite these limitations, it is possible to translate the general approach adopted for the chipless tags to an non-linear system that can display enhanced performance, on the one hand, and allow the mixing of elements operating at different frequencies, on the other. This latter factor opens a rich landscape of commercial and stand-alone sensing components for use in these motes.

4.1 Backscatter modulation

As argued in section 1.4.3, a common way of introducing non-linearities into an antenna structure relies on switching its RCS between two or more states, to modulate the reflected power. The usual environmental calibration technique used in many chipless RFID efforts partially essentially emulates this process by switching creating two states with and without the tag, equivalent (from an antenna-mode perspective) to a fully-reflective state with a given phase and a fully-matched state, respectively. An electrical switching between those two states would not only allow this process to occur without an impractical human intervention, but would also allow for the de-embedding of the structural mode of the tag. The Van-Atta reflectarray presented in section 1.4.4 relies on the connections between antenna pairs to enable its retrodirective behavior. The disappearance or sectioning of these connecting lines would result in the signal received by each polarization each of the antennas to be reflected back and re-emitted. The consequence of such a process would be to prevent coherent re-emission of the signal in the direction of the reader—except in some very specific circumstances, for a single, specific direction—and to, therefore, reduce significantly the RCS of the tag. In addition, the re-emitted EM-wave would have a orthogonal polarization than that expected by the reader's receiver. This would, therefore, allow the creation of a second state akin to the matched condition used in standard RFIDs, where the RCS of

the tag is significantly decreased or, even, resulting in a signal below the noise floor. Such a backscatter system could take advantage of the benefits of high operating frequencies that were demonstrated for its chipless counterpart and could potentially find its place along the plethora of 5G and IoT devices whose development is currently underway. Nevertheless, unlike all of its active counterparts operating in these bands, the device could display orders-of-magnitude less complexity, cost (depending on manufacturing scale), and power consumption. This perspective was adopted, thereby naturally resulting in the choice of one the 5G bands for its design. Due to its relatively lower frequency, the $28\,\mathrm{GHz}$ 5G band was selected.

4.1.1 Switch

In an effort to create a low-cost circuit for the switching of the antenna structure used in section 1.4.4, the design of a switch using a single-transistor was undertaken. A transistor compatible with this application required both low-power consumption, cost, and a compatibility with frequencies of operation in excess $24\,\mathrm{GHz}$. Such requirements were met by GaAs FETs manufactured by California Easter Laboratories. At the time of the writing of this thesis, the CE3524K3 is the most capable and latest version of this family of components. These FETs, used for amplification applications, translate through their packaging the expectation of common-source operation. Indeed, their Micro-X and SMD packages present two antipodal source pins, as shown in fig. 4.1. In order to avoid design complexities associated with the combination of the two ports in direct transmission configurations—as a way to present a serial "open" and "short" on the transmission lines—a stub-based reflective switch architecture was adopted.

The design of the switch uses the GaAs FET to switch the length of a stub—placed in parallel with the line connecting two antennas of the array—between $\frac{\lambda_g}{4}$ and $\frac{\lambda_g}{2}$ (where λ_g is the wavelength in the transmission lines used for the stubs), presenting either a virtual short or open, respectively.

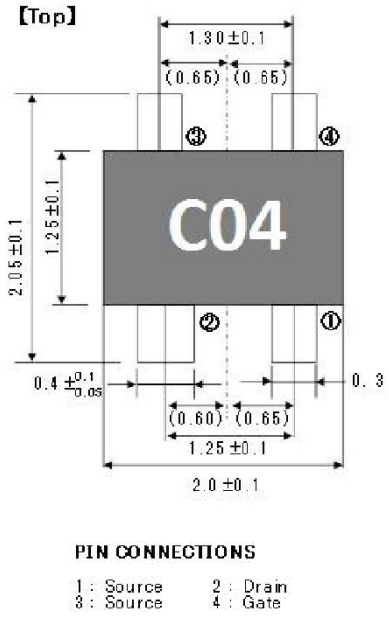

(a)

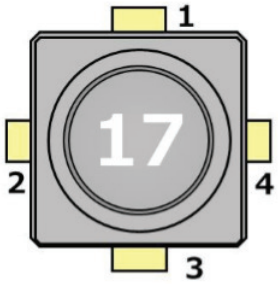

Pin No.	Pin Name
1	Source
2	Drain
3	Source
4	Gate

(b)

Figure 4.1: Pin configurations of the (a) SMD and (b) Micro-X packages of the CEL CE3524K3

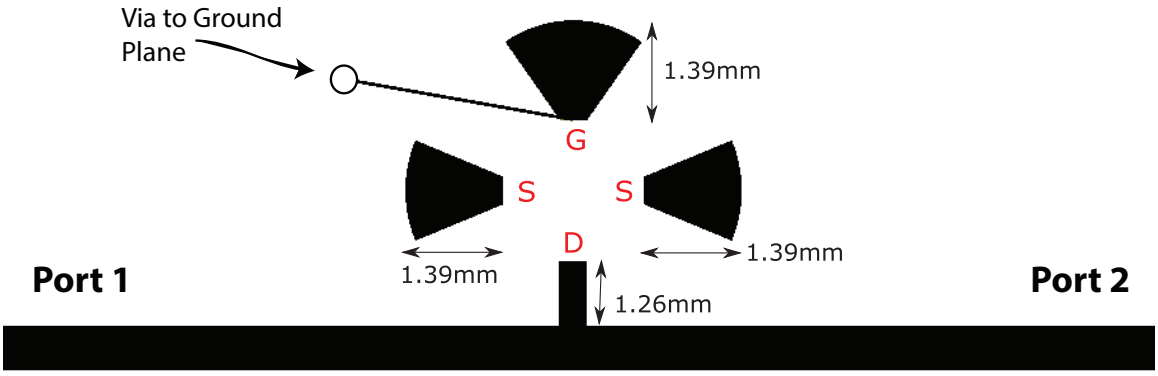

Figure 4.2: Schematic of the layout of the switch design used for a backscatter tag

This approach resulted in the design shown in fig. 4.2. The switch was then tested, using two end-launch connectors on the feed lines, and a bias tee to apply the bias on the drain of the FET, while a clip was used to connect the ground plane and, therefore, the

gate. The results are shown in fig. 4.3. The pHEMTs FET is normally 'OFF' and requires a voltage of about $1\,\mathrm{V}$ to be switched 'ON'. Along with its ultra-small capacitance (on the order of a few hundreds of fF), this low switching voltage endows this FET with a an ultra-low switching energy, ideal for backscatter systems. Indeed, the power consumption of a FET-enabled backscatter front-end is the sum of the contribution of a static leakage current through the gate and of the dynamic power used to alternatively charge and discharge the gate capacitor during the modulation. This can be written as:

$$P_{tot} = \frac{1}{2} V_{bias} I_{leakage} + \frac{1}{2} f_{mod} C_{gate} V_{bias}^2 \tag{4.1}$$

With a biasing voltage of $V_{bias} = 1V$, an assumed capacitance of $C_{gate} = 100fF$, a leakage current $I_{leakage} = 400nA$, and a square modulation signal of frequency $f_{mod} = 100$, the estimated power consumption of a single transistor is estimated to be $P_{tot} = 205nW$.

The switch displayed insertion losses of better than $1\,\mathrm{dB}$ and less than $6\,\mathrm{dB}$ in its 'ON' and 'OFF' states, at its design frequency of $28\,\mathrm{GHz}$. It is important to outline that, while not necessarily an impressive attenuation level, the $-6\,\mathrm{dB}$ provides a modulation factor of (phases being very close) $|\Delta\Gamma| = |\Gamma_{ON} - \Gamma_{OFF}| = 0.54$. An excellent attenuation of about $-20\,\mathrm{dB}$ would, by contrast, display a $|\Delta\Gamma| = |\Gamma_{ON} - \Gamma_{OFF}| = 0.78$ and, thereby, only provide a marginal improvement of the link budget of the communications channel. Furthermore, backscatter channels' link budgets vary with an inverse fourth power of the range; the reading range would, therefore, only increase by about 8%, were the attenuation to reach $-20\,\mathrm{dB}$. On a final note, it should be mentioned that, even if these two states are the standard conditions used by passive RFIDs, they do not provide the optimal detectability for passive system, for the reasons discussed in section 1.4.3. Indeed an optimal couple would consist of transmission coefficients displaying as little attenuation as possible and antipodal transmission phases. While such couples are readily obtained in reflective configurations by simply switching between *open* and *short* real or virtual loads, their obtainment in transmission is less straightforward. A solution has been proposed to provide

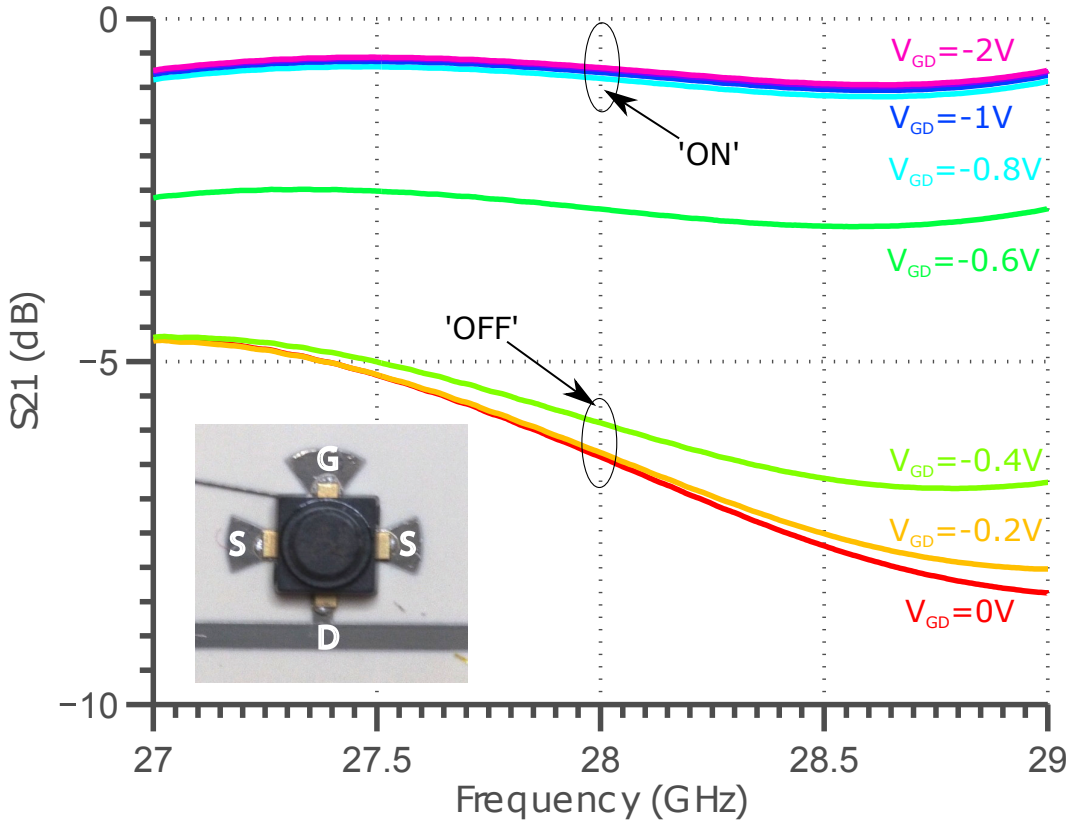

Figure 4.3: Measured transmission loss through the switch presented in fig. 4.3

such features [113], but currently require the use of 2 transistors and of a large coupler. Nevertheless, this architecture, in theory, can improve the link budget by as much as 3 dB and, more importantly, allow the use of more complex modulation schemes such as QAM and QPSK.

4.1.2 Printed mm-wave backscatter tag

The tag whose design and use for chipless RFID applications was presented in chapter 3 relied on the use of Kapton polyimide to acquire humidity sensing abilities. In the context of backscatter tag targeting a given frequency of operation, this feature becomes a defect that needs to be eliminated. In order to do so, the backscatter tags were designed on a flexible LCP substrate, whose humidity absorption level is several order of magnitude lower than that of Kapton HN. The overall design of the tag remained very similar. Its constituting

antenna and its measured matching over the frequency band of operation are shown in fig. 4.4. The antenna was fully inkjet-printed onto a 5-mil-thick flexible LCP substrate and was (fig. 4.4b) shown to provide a matching of better than $-15\,\mathrm{dB}$ for both polarizations.

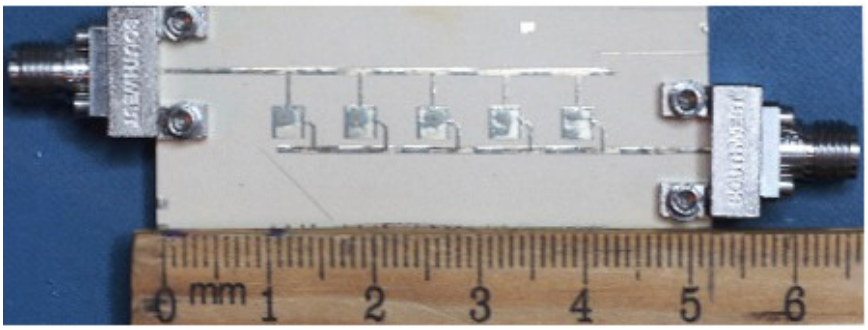

(a)

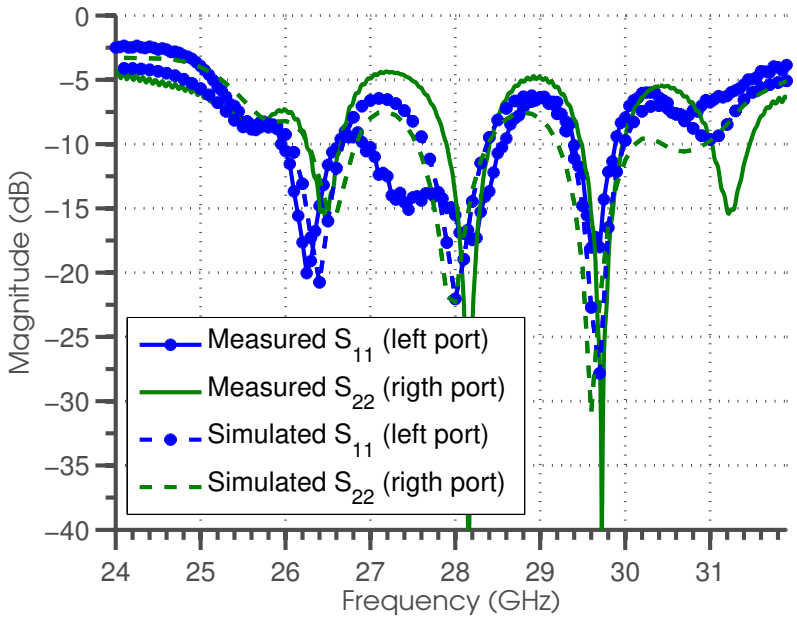

(b)

Figure 4.4: (a) Image and (b) measured S_{11} of the antenna constituting the backscatter tag

Five of these antennas were then connected in couples, in the same way described in chapter 3, with the addition of one of the switches presented in section 4.1.1 for each transmission lines, as shown in fig. 4.5.

The link budget of the backscatter link between the tag and its reader can be shown to depend on its differential RCS [114, 115], which is defined as the magnitude of the differ-

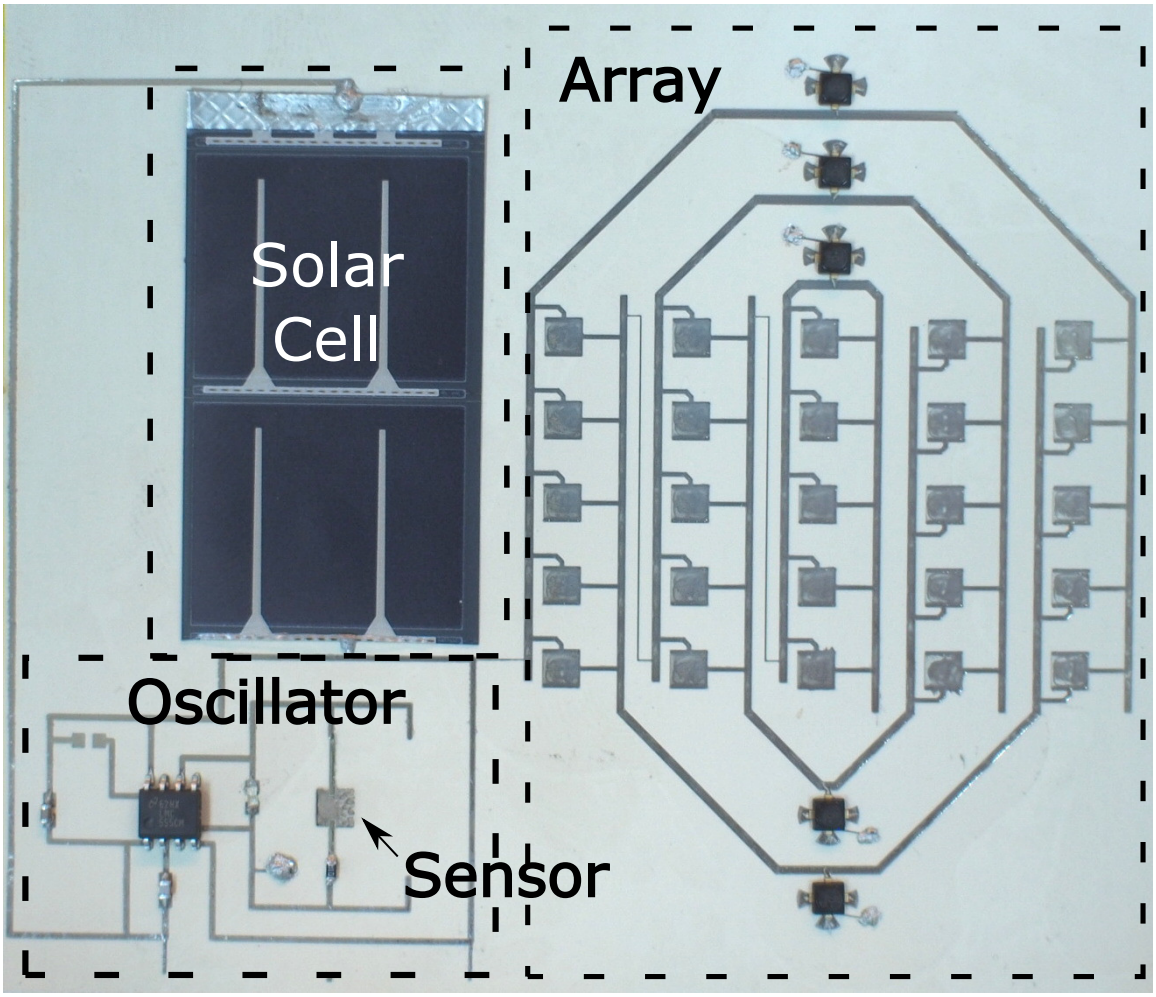

Figure 4.5: Picture of the final flexible, mm-wave inkjet-printed backscatter tag

ence in the complex (phase and magnitude) radar cross section between the two modulation states of the tag. Here, the tag cross-polarizes the wave that is re-emitted in the direction of the reader. Therefore, the cross-polarized RCS is the metric of interest in this context. The cross-polarized differential monostatic RCS of the structure (shown in fig. 4.5) measured in an anechoic chamber, using co-located side-by-side cross-polarized emitting and receiving antennas, and rotating the tag to illuminate it from different angles of incidence. For each angle, the complex transmission coefficient between the two antennas was measured with a VNA. The measurement was done twice: once in each of the configuration states, by changing the bias applied on the front-end of the tag without moving it between measurements in both of the two states. A metal sphere of 6 inches in radius was used as

a reference target, as was the case for the chipless tag of chapter 3. The results of this test, at the measured optimal frequency of $27.978\,\mathrm{GHz}$, are shown on fig. 4.6 and display the typical Van-Atta response. The RCS presented a maximum of $-29\,\mathrm{dBsm}$, and a variation of less than $7\,\mathrm{dB}$ from $-50°$ to $50°$ of interrogation angle: the structure displays a high and largely isotropic cross-polarized monostatic differential RCS.

Figure 4.6: Measured cross-polarized differential monostatic RCS of the active Van-Atta reflectarray prototype

As with all integrated backscatter systems, the tag requires a low-power piece of circuitry in order to provide the baseband signal that is used to control the modulating switches of the front-end. In this particular system, an LMC555 from Texas Instruments was adopted and integrated into the inkjet-printed circuit layout of the tag's baseband. The LMC555 was selected for its low operating minimum operating voltage of $1.5\,\mathrm{V}$, and its ability to generate modulation signals at frequencies up to $3\,\mathrm{MHz}$ while only requiring only rather minimal amounts of current (up to $150\,\mu\mathrm{A}$ with a $1.5\,\mathrm{V}$ supply voltage). Finally, sensing capabilities were added to the tag by integrating a fully-inkjet-printed sensor. The sensor was

fabricated by first inkjet-printing a custom ink, made by dispersing PABS-functionalized single-wall-carbon-nanotubes (P8-SWNT from Carbon Solutions) in water. Once printed using a Dimatix 2800 inkjet-printed, the CNT film was dried at $100\,^{\circ}\mathrm{C}$. Inter-digitated-electrodes (IDEs) were printed with SNP ink onto the CNT film, in order to connect it. The silver ink was then dried an sintered in an oven at $180\,^{\circ}\mathrm{C}$. The resistometric component was then tested in the controlled chamber shown in fig. A.1. The results of this characterization (shown on fig. 4.7), shown a very large relative sensitivity of more than $12\,\%$ after exposure to 2ppm of ammonia for one hour.

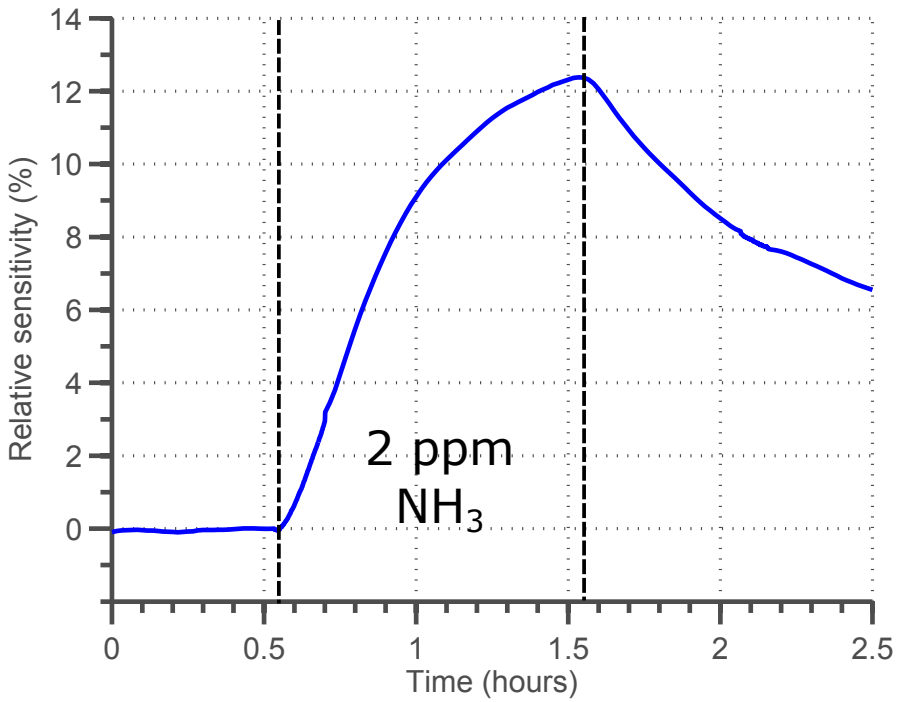

Figure 4.7: Measured relative response of a printed SWCNT-PABS-based sensor to 2ppm of ammonia

The sensor is therefore very much capable of detecting a concentration of 2ppm, which is 25 times smaller than the general OSHA Permissible Exposure Limit (PEL) of 50ppm. As in the work of [64], the oscillating frequency of the LMC555 is related to the value of a resistor by $f = \frac{1}{1.4R_{sensor}C}$, where C and R_{sensor} are the values of external capacitor and resistor used with the timer. Here, a capacitor $C = 1nF$ was selected to ensure an

operation of the tag in the neighborhood of $1\,\mathrm{MHz}$. In order to provide energy autonomy to the system, two of the four cells of a Powerfilm MP3-25 solar element were cut out and attached to the circuit using a combination of double-sided tape and of silver epoxy. Each cell of the solar cell can generate up to their open-circuit voltage of $0.9\,\mathrm{V}$. Under an illumination of $900\,\mathrm{lx}$ and in the absence of ambient ammonia, the completed system displayed an operating voltage of $1.5\,\mathrm{V}$, an oscillation frequency of $1.4\,\mathrm{MHz}$, and a power consumption of $216\,\mu\mathrm{W}$.

4.2 Wireless sensing

The very system shown on fig. 4.5 was set onto a wall, and wirelessly interrogated at a distance of $5\,\mathrm{m}$ using a custom reader (shown on fig. 4.12) whose IF output was measured using a RSA3408A spectrum analyzer. For this test, the array was fed through a power supply, as the indoor lighting conditions were not sufficient in order to provide enough voltage for the system that was optimized for outdoor operation. In this configuration, the sensor was then exposed to a short illumination of pure anhydrous ammonia, which was then allowed to dissipate in its environment. The exposure to the ammonia changed the resistance of the printed CNT-PABS ammonia sensor, which consequently resulted in the shift in the read backscatter modulation frequency, that is displayed in the real-time spectrogram of fig. 4.8. The result displays an almost instant response of the sensor (and therefore the related backscatter modulating frequency) to the exposure to ammonia, before returning to a stable final state. It should be noted that the new state of the sensor is different from its original resistance. This change of the baseline is not unusual for such sensors when exposed to large concentrations of analytes.

A later experiment, conducted with an upgraded tag operating at $24\,\mathrm{GHz}$ and interrogated using the FMCW reader described in more detail in section 5.2, a printed nerve agent sensor built according to the methods shown in section 2.2.3, was also printed onto the device. The tag was set into a sealed plastic box (about $7\,\mathrm{cm} \times 7\,\mathrm{cm} \times 15\,\mathrm{cm}$ in dimensions),

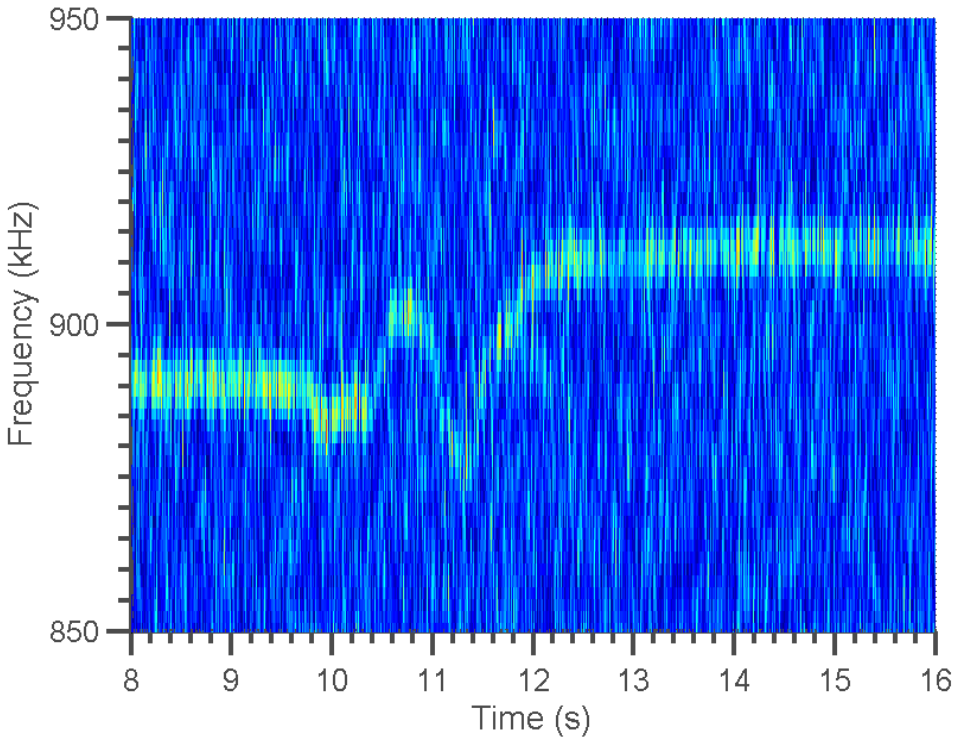

Figure 4.8: Real-time spectrogram of the wirelessly-measured response of the printed Van-Atta reflectarray system to exposure to a short illumination of pure anhydrous ammonia

$5\,\mathrm{m}$ away from the tag, before a few drops of liquid DMMP were sprinkled in its vicinity. The wirelessly-measured response of the tag, shown in fig. 4.9.

4.2.1 Electronic nose configuration

A significant challenge in the detection and discrimination of airborne analytes lies in the general multi-sensitivity of the sensing elements. A strategy used in the animal kingdom–by mammalians–to mitigate these limitations relies on the use of arrays of different sensors whose combined response can be utilized to solve for the complex mixture and the concentration of their chemical environment. This method, brought to popularity by the work of Persaud and Dodd [116], has since benefited from significant attention and related improvements [117]. The method relies on the necessary integration of arrays of co-located sensors. A first step towards the use of such an approach for the backscatter nodes pre-

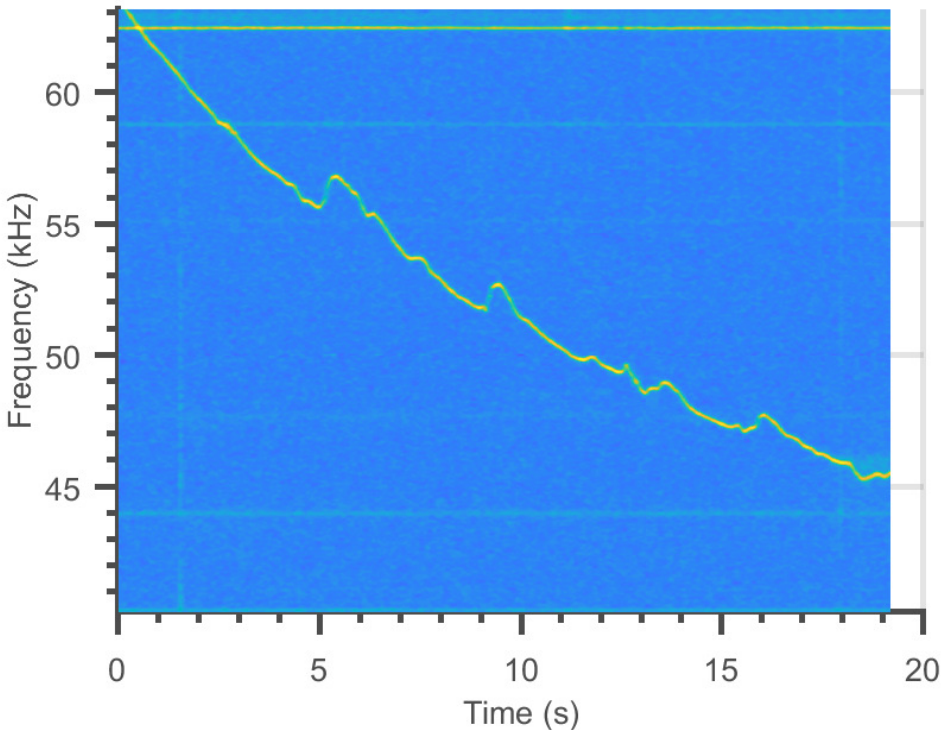

Figure 4.9: Real-time spectrogram of the wirelessly-measured response of the Van-Atta reflectarray system to exposure to a short exposure to ambient DMMP, a nerve agent simulant

sented in this thesis would need to rely on a low-power architecture capable of providing this integration.

Such an architecture was designed and is shown in fig. 4.10. The circuit operates the switching between several resistometric gas sensor using the ultra-low-power NX3L4051 switch, which alternatively connected the 555 timer to each element of the sensors array. The tempo of this switching sequence is controlled by an ultra-low-power oscillator, whose output is translated into a parallel stream of bits by the SN74HC393 counter, thereby implementing the incremental configuration of the switching between the sensors.

Four different sensors were printed onto a PET substrate and connected to a prototype of the circuit schematized in fig. 4.10. The array was constituted of an ammonia and a DMMP sensor—identical to the ones used in section 4.2—and of printed PEDOT:PSS humidity sensors and a reference resistor. The system was exposed to ammonia, using a

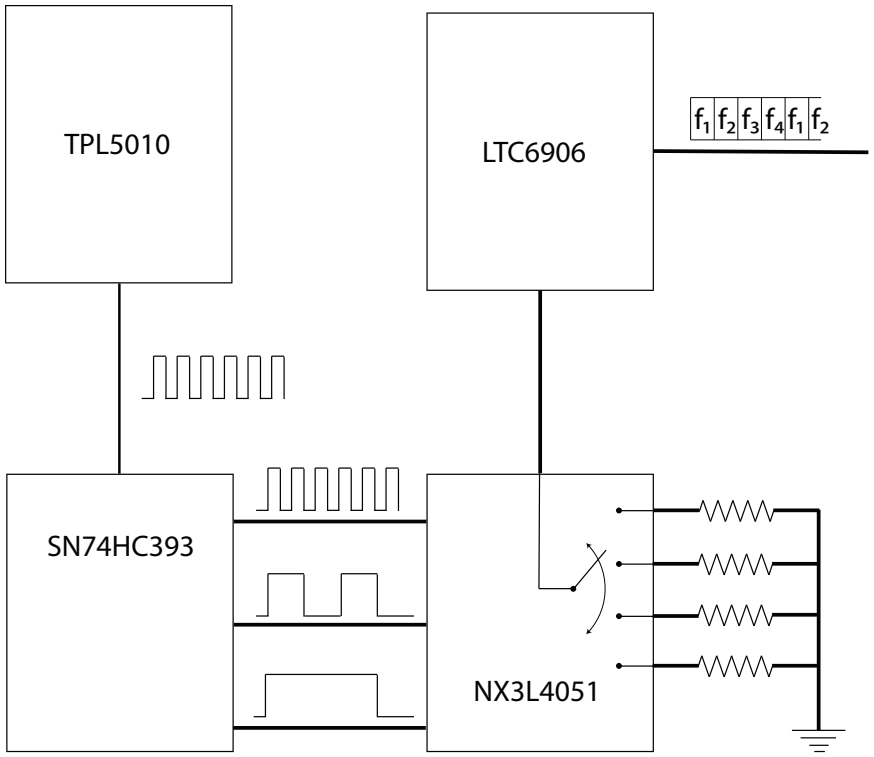

Figure 4.10: Schematic of the electronic-nose-enabling baseband circuitry

similar protocol as the one executed in the experiment leading to the measurement shown in fig. 4.8. The associated response in the response of the baseband circuit is shown in fig. 4.11. The ammonia and DMMP sensors display a sharp response to the exposure to the ammonia, while the other two elements remained rather stable. In fig. 4.11b, it can be seen that the modulation frequency induced by the ammonia sensor crosses that of the DMMP sensor, which is a consequence of its superior sensitivity to the ammonia. This experiment epitomizes the necessity for an electronic nose configuration. A system equipped with nerve-agent sensing capabilities alone—even if only intended to detect such targets—would output a significantly falsely positive response if exposed to ammonia. By adding a sensor with optimal and lackluster ammonia and DMMP sensitivities, sensitivities, the ambiguity can be lifted and, in principle, the extraction of concurrent ammonia and DMMP levels could be achieved.

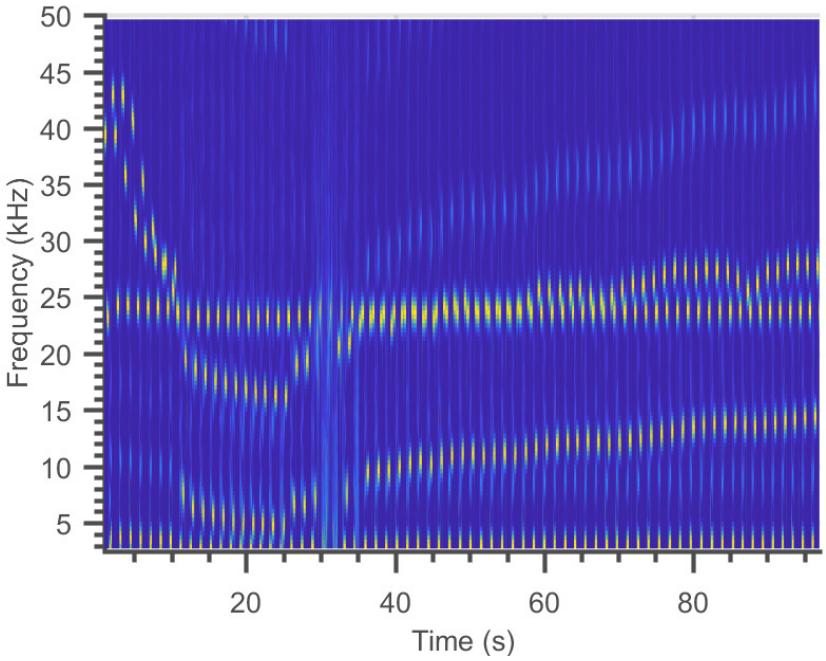

(a)

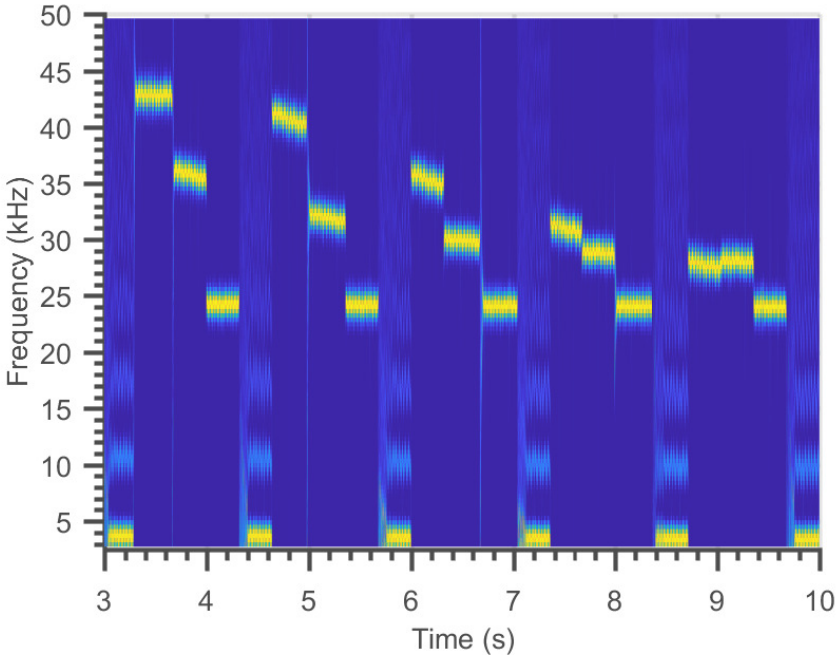

(b)

Figure 4.11: (a) Long and (b) short-time measured output of the baseband timer's modulation

4.3 Long range detection

In order to demonstrate its long-range detection capabilities, the backscatter-modulation reflectarray was set onto a metallic shelf, illuminated with an artificial light source with an illuminance of $900\,\mathrm{lx}$ (more than one order of magnitude less than in average outdoor daylight), to provide sufficient lighting for its constant and stable operation. An interrogator was assembled from laboratory-grade components to form the system schematized in fig. 4.12. The reader used an Anritsu 37369A Vectorial Network Analyzer as the local oscillator for the reader system, due to its availability. A splitter displaying was subsequently added to send half of the power towards an LB-CNH-28-20 conical horn antenna in order for it to be emitted in the direction of the tag. The other half of the power was fed into the LO channel of a ADC2640-1 mixing downconverter from Microwave Dynamics. The response of the tag is received by the RX antenna of the reader, which is cross-polarized with its TX counterpart, and connected to the RF input of the mixer and downconverted. The two antennas were set in the same configuration shown in fig. 3.14 to enhance their gain up to an estimated $30\,\mathrm{dBi}$.

The tag was interrogated at a distance of $80\,\mathrm{m}$, in the configuration shown in fig. 4.13. The emitted power used for the test was on the order of $13\,\mathrm{dBm}$ (with the subtraction of minor cable losses) yielding an EIRP on the order of $40\,\mathrm{dBm}$. Both emitting and receiving antennas, operating within the same lens antenna system, were cross-polarized. It should be noted that this configuration takes advantage of the rare ability of this RFID tag to cross-polarize its reflected signal with respect to the CW impinging from the reader, thus enabling improved self-interference rejection through the use of cross-polarized RX and TX reader channels. The measured signal to noise ratio at this distance, with a signal level of $-114\,\mathrm{dBm}$ shown in the measured spectrum in the inset of fig. 4.13, was on the order of $4\,\mathrm{dB}$ and shows a noticeable astablity of the oscillator, marked by the appearance of two peaks around the expected modulation frequency. The noise floor, using a $50\,\mathrm{Hz}$ sampling

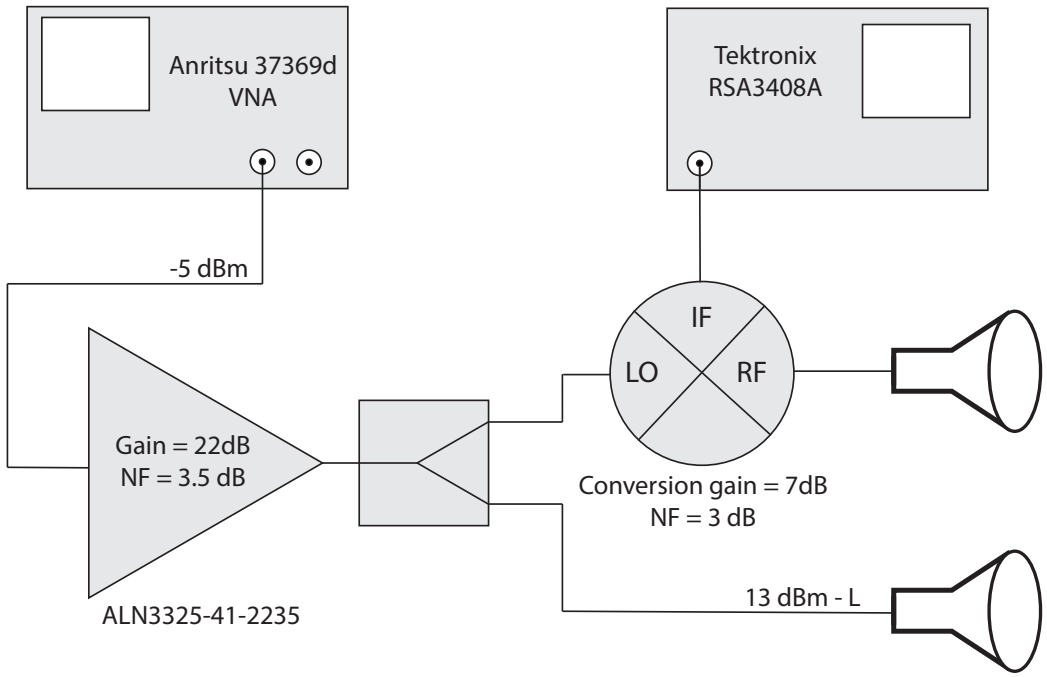

Figure 4.12: Schematic of the custom reader used for the long-range detection test

rate, was measured at a level of $-118\,\mathrm{dBm}$.

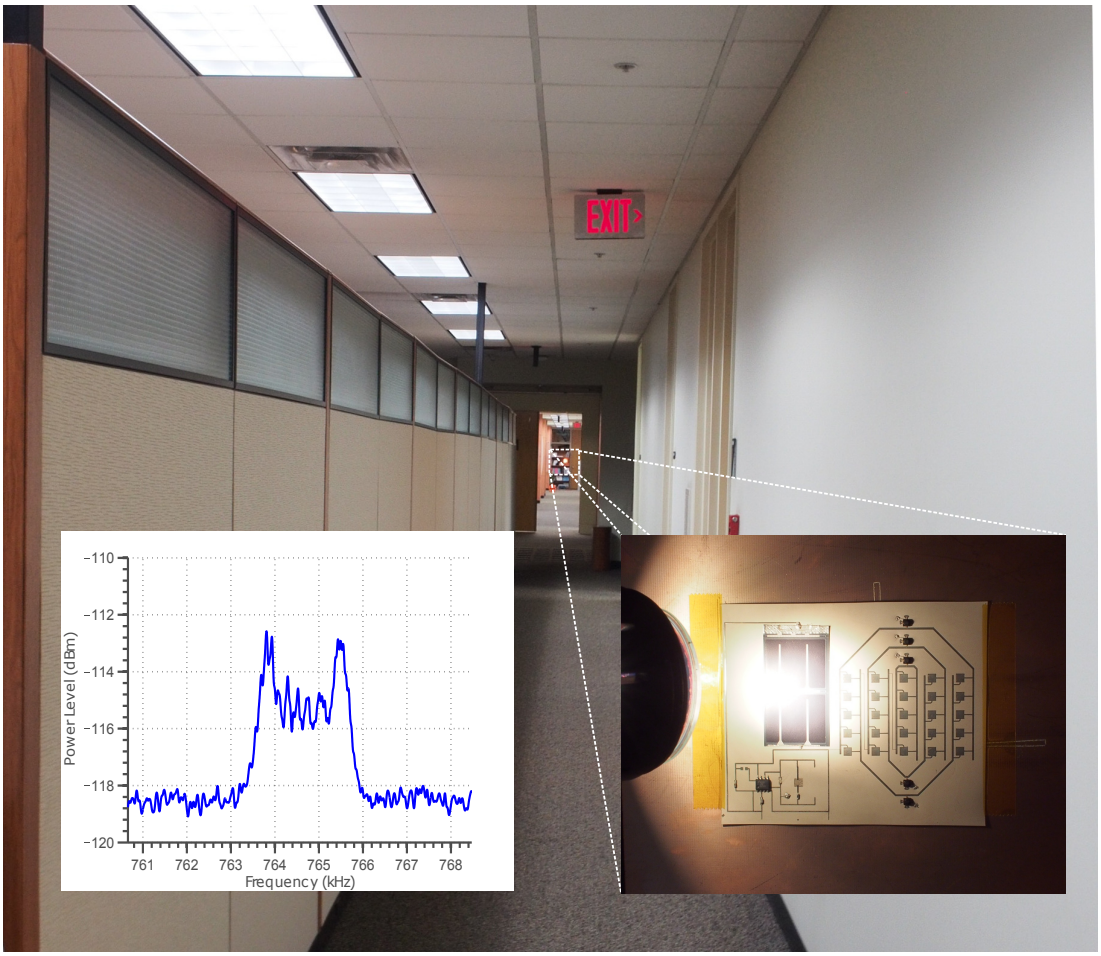

Figure 4.13: Long-range ($80\,\mathrm{m}$) measurement configuration of the Van-Atta reflectarray sensor, and the measured IF spectrum (inset)

CHAPTER 5

READER CAPABILITIES FOR MM-WAVE "SMART SKINS" LONG-RANGE INTERROGATION AND LOCALIZATION

In chapter 4 was presented an ultra-long-range backscatter mm-wave tag architecture, equipped with the ability to sense, in real time, the presence of gases in its vicinity. In addition to the capabilities presented in that chapter, the operation at mm-wave frequencies also translate to interesting and consequential new opportunities and capabilities for backscatter readers. This chapter will focus on identifying the reader properties limiting the reading range of the tags presented in chapter 4 and demonstrate major improvements, and a road-map toward the emergence of multi-km-range mm-wave RFIDs in the 5G bands. Finally, a scheme capable of enabling the precise localization of these retrodirective tags is proposed, simulated, and implemented. The application of this scheme presents, for the first time, a compact and low cost approach for the 2D localization and identification of self-powered mm-wave backscatter tags.

5.1 Improvement of the range

5.1.1 An upgraded reader

The reader system shown in fig. 4.12 displayed a sensitivity of $-142\,\mathrm{dBm\,Hz^{-1}}$ ($-118\,\mathrm{dBm}$ - $7\,\mathrm{dB}$, at $50\,\mathrm{Hz}$ sampling). The sensitivity of the system has, therefore, a potential theoretical gain of $28\,\mathrm{dB}$ to be taken advantage of, before reaching the theoretical noise floor of $-173\,\mathrm{dBm\,Hz}$. In addition, the new mm-wave bands regulated by the FCC open the opportunity for emissions with powers up to, in some cases, $70\,\mathrm{dBm}$ of EIRP. The reader could, consequently and conceptually, increase the depth of its allowable link budget by $50\,\mathrm{dB}$. For backscatter channels, this gain represents a possible increase in the maximum

reading range by a factor of $2^{50/12} = 17.96$. In order to exploit a part of this potential for range improvement, the assembly of an upgraded reader was undertaken. The observation of the reduction of the interference floor upon an increase in the physical separation of the RX and TX antennas led to the conclusion that the main contributor to the observed noise floor was—as is typical is monostatic backscatter reading systems—the coupling between RX and TX channels. In other words, the sensitivity of the reader used in the measurement shown in fig. 4.13 was effectively limited by the high phase noise ($-60\,\mathrm{dBc\,Hz^{-1}}$ at $10\,\mathrm{kHz}$ offset and $20\,\mathrm{GHz}$ center frequency) of the output signal of the Anritsu 37369A, used as the local oscillator for the reader system. As a consequence, the first step in the assembly of an improved reader was an upgrade in its LO source. From the noise properties of this LO, the dimensioning of the system could then be undertaken. Such a component was found in the PLO-2072 from Microwave Dynamic. This PLO, operating at a frequency of $28\,\mathrm{GHz}$ was characterized with a spectrum analyzer and displayed the phase-noise and spurious properties shown in fig. 5.1.

The PLO improves upon the theoretical phase noise level of the Anritsu VNA by more than $50\,\mathrm{dB}$. At offset frequencies of $90\,\mathrm{kHz}$, the PLO generates noise levels of less than $-113\,\mathrm{dBc}$. As shown in fig. 5.2, the PLO outputs $25\,\mathrm{dBm}$ of power, which is then split to be emitted by the TX antenna on the one end, and attenuated down to $13\,\mathrm{dBm}$ to feed the LO port of the downconverting mixer on the other. The RX/TX antenna system was identical to the one used in the experiment described in section 4.3. The signal received on the RX channel is amplified by an LNA with $22\,\mathrm{dB}$ of gain, to be then downconverted. The tag was also slightly upgraded, with the LMC555 timer being replaced with a lower-power CSS555, to bring the total consumption of the system down to $21\,\mu\mathrm{W}$. Due to the relative purity of the LO's spectrum observed between in fig. 5.1 and to the reduced power consumption of lower-frequency-operating timers, a lower modulation frequency of about $50\,\mathrm{kHz}$ was selected for the tag, which enabled this selection of this new timer.

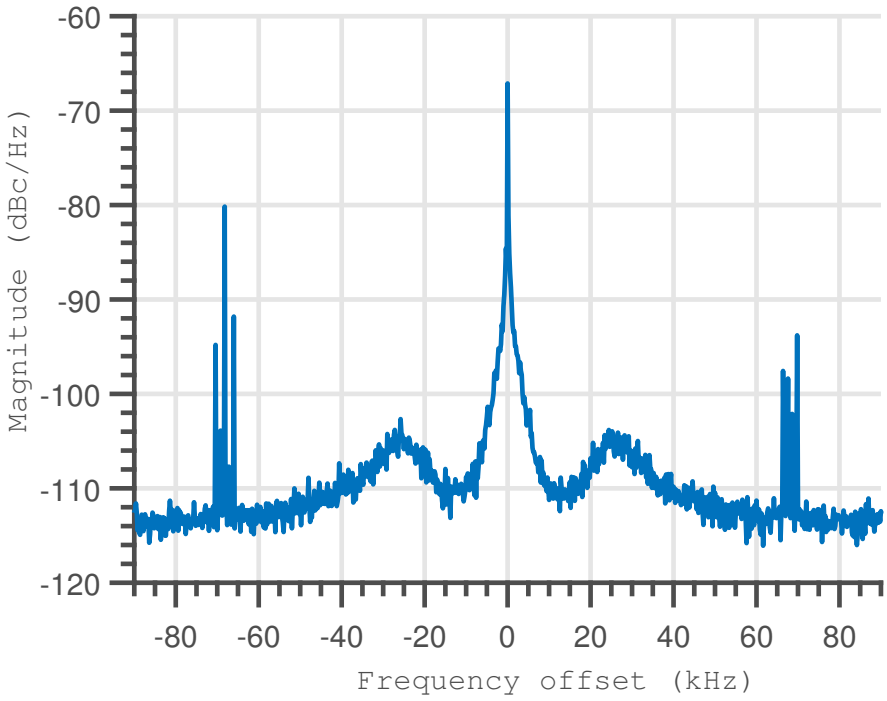

Figure 5.1: Measured spectral purity of the PLO-2072 oscillator, with a center frequency of 28 GHz

5.1.2 Experimental demonstration and performance analysis

The system was set outdoors, in the context shown in fig. 5.3. In these experimental conditions, the tag was easily powered using the ambient solar lighting. The measured response, shown in fig. 5.3, displays a noise floor of $-135\,\mathrm{dBm\,Hz^{-1}}$ ($-122\,\mathrm{dBm\,Hz^{-1}}$ at 20 Hz bandwidth). Taking into account the 22 dB and 7 dB gains of the LNA and of the downconverting mixer, respectively, this translates to an RX sensitivity of $-161\,\mathrm{dBm\,Hz^{-1}}$, compared to the $-142\,\mathrm{dBm\,Hz^{-1}}$ of the setup shown in fig. 4.13. Along with its emitted power of approximately 21 dBm—versus 13 dBm for the last setup—the reader demonstrated an improvement of 27 dB in its allowable link budget, relative to the previous reader. The measurement, shown in fig. 5.3, displays a SNR of nearly 22 dB at 90 m. This translates to a theoretical maximum range of 320 m, at the unity SNR limit.

If the properties of the antenna, the reader, and that of tag front-end shown in fig. 3.6 are used in eq. (3.2), the expected received power (without any of the losses in the system

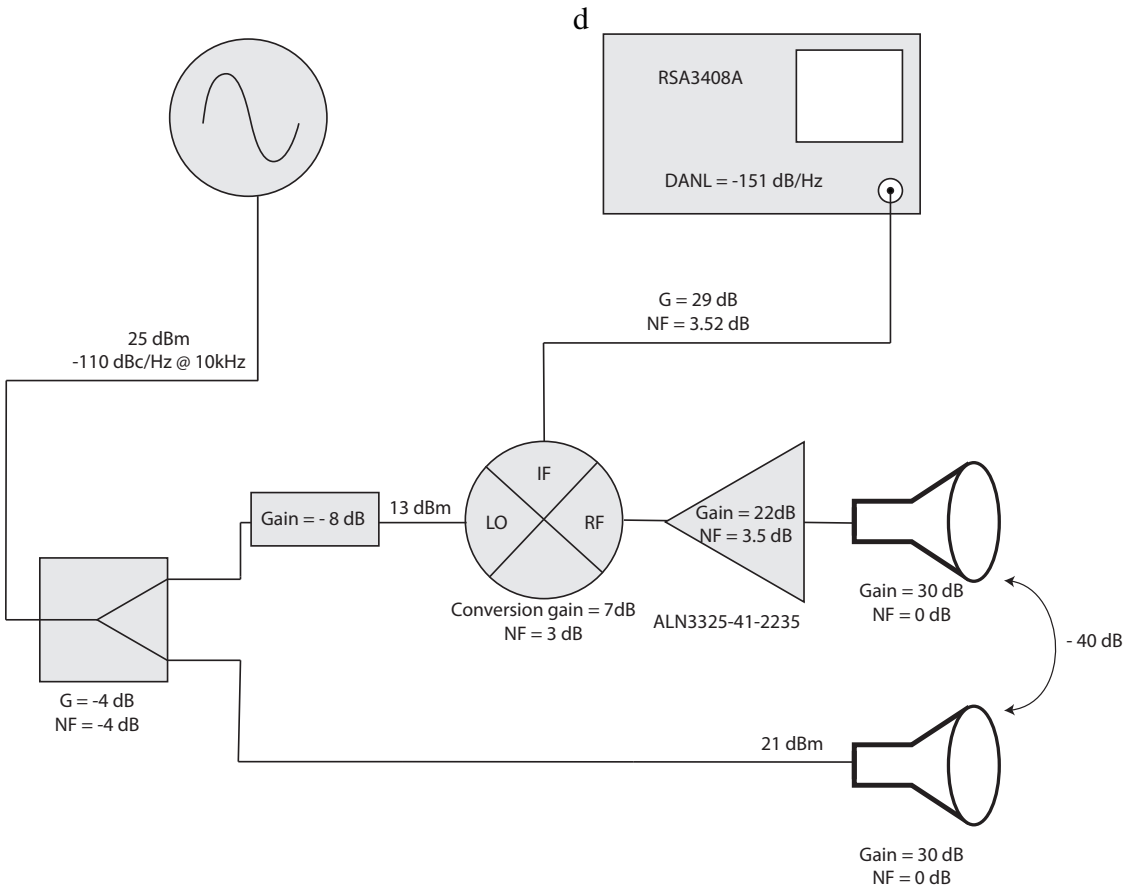

Figure 5.2: Schematic of the upgraded reader system

being considered) is $P_r = -95$dBm, which after the amplification chain in the receiver translates to $-66\,\mathrm{dBm}$. In other words, the measured SNR is missing an approximate $34\,\mathrm{dBm}$, relative to its expected theoretical value. The measurement data also shows a broad peak for the response of the tag. Its FWHM is on the order of $2\,\mathrm{kHz}$. For an equal total power, the fraction of the spectral power encompassed in the $f_0 - \frac{BW}{2}$ and $f_0 + \frac{BW}{2}$ (where BW is the sampling bandwidth and f_0 is the timer's oscillating frequency) can be expressed as:

$$P_{peak} = 1 - \left(1 + \mathrm{erf}\left(\frac{-BW/2}{\sigma\sqrt{2}}\right)\right) \tag{5.1}$$

, where erf is the error function associated with the CDF of the normal distribution. Combined with the eq. (3.8), relating FWHM and σ, it follows that the maximum of the observed

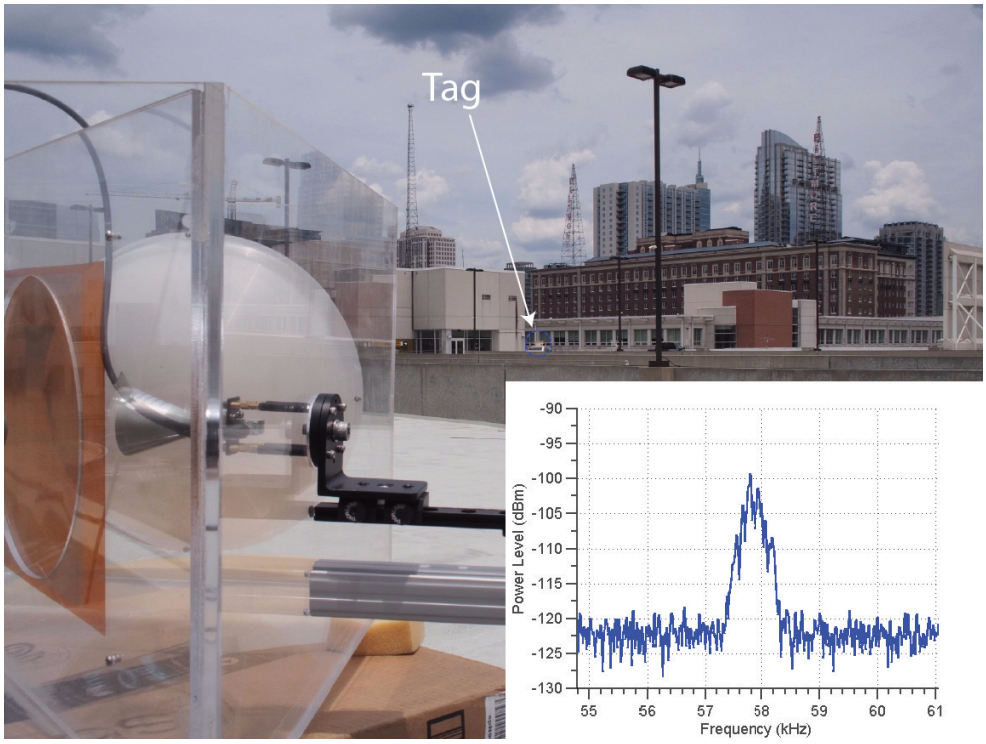

Figure 5.3: Outdoor measurement context and measured spectrum (inset) with the improved reader/tag system

peak is $12\,\mathrm{dB}$ lower than would, ideally, be expected. The SNR of the measurement could, therefore, be improved by $12\,\mathrm{dB}$ if the jitter of the timer could be decreased to a lower level.

A timing component providing both low-power consumption and low jitter could, therefore, theoretically increase the reading range of the system by two-fold, to a maximum of $640\,\mathrm{meter}$ with a sampling rate of $20\,\mathrm{Hz}$. This combination of properties is precisely what the LTC6906 timer from Linear Technologies can offer. The component was integrated into a testing PCB and its spectral output was measured with the spectrum analyzer. The result, shown on fig. 5.4 displays a FWHM of $1\,\mathrm{Hz}$ and could, therefore, provide this gain.

The measured signal level, even once the influence of the jitter is accounted for, $22\,\mathrm{dB}$ still is missing from the link's budget. Much of this can be accounted for by connection losses through the long cables used to connected the different elements of the reader and due to tow-quality interconnects.

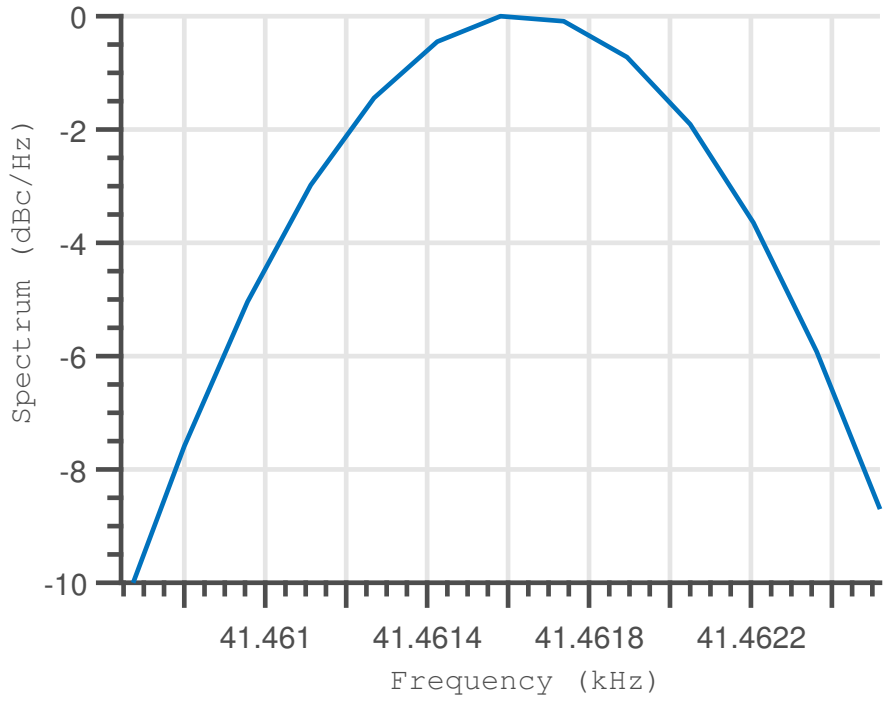

Figure 5.4: Measured spectral output of the LTC6906 timer

The experiments conducted during this project demonstrate the extent of the potential of such approaches for the implementation of ultra-long range RFIDs, using retrodirective Van-Atta backscatter arrays. Through further integration and loss mitigation in the reader, another 2 to 4-fold improvement up to ranges of $1.2\,\mathrm{km}$ and $2.4\,\mathrm{km}$, respectively, at a $20\,\mathrm{Hz}$ sampling rate could be achieved. In addition, if higher modulation frequencies were adopted for the tag, if improved ultra-low-phase-noise sources were used as the LO, or if the RX to TX coupling could be further lowered, the maximum *theoretical* range achievable with such a system—using the full $70\,\mathrm{dBm}$ EIRP allowed in these bands—could reach more than $12\,\mathrm{km}$.

5.2 FMCW-enabled localization

The general localization of passive, semi-passive, or active targets depends on the processing of the magnitude, time-delay and/or phase properties of wireless signals. More specifically, resolution of radial measurements is fundamentally limited—due to the time-

spread of the inverse Fourier transform of the frequency window inevitably induced by the constrained frequency occupation within the band—by the frequency bandwidth of the wireless signal used for the ranging. The accuracy of a wireless localization effort does not suffer from such fundamental limitations but is, generally, practically limited by the ability to accurately measure phases and by the propagation length associated (through the wavelength) with such a phase. Consequently, both the resolution and the accuracy of wireless ranging measurements can greatly benefit from the use of higher-frequency and larger-bandwidth bands. One of the possible schemes used for the implementation of ranging is the FMCW. The processing approach used in chapter 3 used the phase of response at each measured frequency point to extract ranging information.

The passive chipless tag creates a signal that, once received by the RX channel of the VNA/reader, can be expressed as

$$S_{chipless} = A(\omega, x)\cos\left(\omega t - 2k(\omega)x\right) \tag{5.2}$$

, where ω is the frequency generated by the LO of the radar and outputted on its TX channel and $k(\omega) = \frac{2\omega}{c}$ is its propagation constant. The VNA, thanks to an I/Q down-conversion, outputs the following downconverted baseband signal:

$$B_{chipless} = A(\omega, x)\exp\left(-i\frac{2\omega}{c}x\right) \tag{5.3}$$

This phase of the signal, as demonstrated, can be processed to extract $A(\omega, x)$ and, thereby, determine the range of the target. If the phase of this signal could be made linearly time-dependent—the very definition of a frequency—the product of the down-conversion process would generate a frequency. The functional consequence of such a output being generated would be the ability to process the baseband data in real time, with a simple In-phase down-conversion, with a simple FFT over time-spread data.

5.2.1 The angularly-resolved MIMO FMCW process with backscatter targets

Modeling and simulation of the process

This linear variation of $\frac{2\omega}{c}x$ can be achieved by simply making ω linearly time dependent, such as described in eq. (5.4) for an up-slope: this is the fundamental insight behind the FMCW process.

$$\omega_{up}(t) = \omega_{min} + \sigma t \tag{5.4}$$

where ω_{up} is the frequency of the mm-wave signal generated by the LO of the radar and outputted on its TX channel, ω_{min} is the lowest frequency of the used mm-wave band, and σ is the slope of the frequency variation. With such a time-dependent frequency, the phase of the radar's LO signal can be calculated to be:

$$\begin{aligned} \phi_{up}(t) &= \int_0^t \omega_{up}(x)\,dx \\ &= \int_0^t \omega_{min} + \sigma x\,dx \\ &= \omega_{min}t + \sigma\frac{t^2}{2} + \phi_0 \end{aligned} \tag{5.5}$$

, where ϕ_0 is its phase at time $t = 0$.

The generated signal propagates during a time $\frac{\Delta t}{2} = \frac{R}{c}$ before hitting the target/tag—that is placed at a distance R from the radar/reader—and travels back during the same amount of time, before being received by the reader. Using the reference of t as the time at the reception of the signal on the RX channel of the radar, its expression has to take into account the original phase of the signal at time Δt and the phase that it acquired during the propagation. This can be written as:

$$
\begin{aligned}
S_{up} &= A\cos\left(\phi_{up}(t-\Delta t) + \omega_{up}\left(t-\Delta t\right)\times\Delta t - k_{up}\left(t-\Delta t\right)\times 2R\right) \\
&= \cos\left(\phi_{up}(t-\Delta t) + \omega_{up}\left(t-\Delta t\right)\times\Delta t - \omega_{up}\left(t-\Delta t\right)\times\frac{2R}{c}\right) \\
&= \cos\left(\phi_{up}(t-\Delta t)\right)
\end{aligned}
\tag{5.6}
$$

Once the signal is received, it is down-converted by the radar through mixing with the signal generated by the LO. The baseband signal outputted by the process, for a simple in-phase down-conversion, can be written as:

$$
\begin{aligned}
B_{up} &= S\times\cos\left(\phi_{up}\left(t\right)\right) \\
&= A\cos\left(\omega_{min}\times\left(t-\Delta t\right) + \sigma\frac{(t-\Delta t)^2}{2} + \phi_0\right)\times\cos\left(\omega_{min}t + \sigma\frac{t^2}{2} + \phi_0\right) \\
&= \frac{A}{2}\cos\left(\Delta t\,\sigma\,t + \left(\omega_{min} - \frac{\Delta t\,\sigma}{2}\right)\times\Delta t\right) + \text{High frequency, filtered output} \\
&= \frac{A}{2}\cos\left(\omega_b t + \left(\omega_{min} - \frac{\omega_b}{2}\right)\times\Delta t\right)
\end{aligned}
\tag{5.7}
$$

, where $\omega_b = \frac{2R\sigma}{c} = \sigma\Delta t$ is what is commonly referred to as the "beat frequency". This frequency is a parameter that can be extracted from the FFT of B_{up} and, once identified, be straightforwardly translated to the range of the target. For a decreasing frequency slope, the frequency generated by the LO of the radar can be written as:

$$
\omega_{up}\left(t\right) = \omega_{max} - \sigma t \tag{5.8}
$$

Using an identical approach, this translates to a down-converted signal expressed as:

$$
B_{down} = \frac{A}{2}\cos\left(\omega_b t - \left(\omega_{max} + \frac{\omega_b}{2}\right)\times\Delta t\right) \tag{5.9}
$$

The equation previously presented in this section describes the response of the radar to a passive target. The goal of this work is to explore the capabilities of mm-wave FMCW approaches for the detection of tags such as the one presented in chapter 4. Therefore, an expression of the response of such a process to the presence of a tag—a target that is no longer passive—needs to be reached.

For simplicity, we assume that the RCS of the tag ($A_{tag}(t)$) is modulated in a sinusoidal manner, with a frequency of ω_m, as shown in eq. (5.10). It should be noted that this is an approximation in two respects. Firstly, the tag's response can (in our system) only be modulated in magnitude. This cuts the magnitude of the response in half, relative to this ideal calculation, but does not change the nature of the process. Secondly, the signal used to switch the tag's FETs is a square wave. From this alone, and from the inevitable distortion in the conversion between gate voltage and RCS, the RCS is guaranteed to include harmonics which, for the purpose of this model, will be neglected.

$$A_{tag}(t) = \mathcal{A}\cos(\omega_m t + \phi_m) \tag{5.10}$$

, where ϕ_m is the initial phase of the modulation signal. Using this magnitude in eq. (5.7) yields:

$$\begin{aligned} B_{up,tag} &= \frac{\mathcal{A}}{2}\cos\left(\omega_m\left(t-\frac{\Delta t}{2}\right)+\phi_m\right)\times\cos\left(\omega_b t+\left(\omega_{min}-\frac{\omega_b}{2}\right)\times\Delta t\right) \\ &= \frac{\mathcal{A}}{4}\Bigg\{\cos\left[\left(\omega_m+\omega_b\right)t+\Delta t\left(\omega_{min}-\frac{\omega_b+\omega_m}{2}\right)+\phi_m\right] \\ &\quad+\cos\left[\left(\omega_m-\omega_b\right)t+\Delta t\left(-\omega_{min}-\frac{\omega_m-\omega_b}{2}\right)+\phi_m\right]\Bigg\} \end{aligned} \tag{5.11}$$

The result shows the emergence of two frequencies where only one was present with the passive target. The spectrum presents a pair of peaks, centered around ω_m and spaced by $2\omega_b$, at $\omega_m \pm \omega_b$.

With the commoditization of mm-wave MIMO FMCW radars for automotive applica-

tions, the opportunity to use such systems to detect and interrogated backscatter targets presents a large appeal. The use of angle-resolving capabilities through multi-channel reception and digital beam-forming can provide, in addition to ranging and communications, the ability to detect tags in angular space. We can now try to understand how the same signal, concurrently received at different positions by several RX antennas and independently down-converted, can be processed to extract angular position. If the receiver is offset by a distance x, relative to the reference position used in the result of eq. (5.11), the effective range between that receiver and the target changes by a small ΔR. This translates to a small shift in the beat frequency of $\Delta\omega_b(x) = \frac{\Delta R\,\sigma}{c}$. The exact same model could be used if several TX channels were employed, or in full MIMO configuration. Here, for the sake of intelligibility and simplicity, the analysis will remain limited to a single TX position.

The response received by this channel can be written as:

$$
\begin{aligned}
B_{up,tag}\left(x\right) = \frac{\mathcal{A}}{4}\Bigg\{ & \cos\Bigg\{\Bigg[\left(\omega_m+\omega_b+\Delta\omega_b(x)\right)t+\left(\Delta t+\frac{\Delta\omega_b(x)}{\sigma}\right) \\
& \left(\omega_{min}-\frac{\omega_b+\Delta\omega_b(x)+\omega_m}{2}\right)+\phi_m\Bigg]\Bigg\} \\
& +\cos\Bigg\{\Bigg[\left(\omega_m-\omega_b-\Delta\omega_b(x)\right)t+\left(\Delta t+\frac{\Delta\omega_b(x)}{\sigma}\right) \\
& \left(-\omega_{min}-\frac{\omega_m-\omega_b-\Delta\omega_b(x)}{2}\right)+\phi_m\Bigg]\Bigg\} \\
= \frac{\mathcal{A}}{4}\Bigg\{ & \cos\Bigg\{\Bigg[\left(\omega_m+\omega_b\right)t+\Delta\omega_b(x)\left(t-\Delta t+\frac{\omega_{min}-\frac{\omega_m}{2}}{\sigma}\right) \\
& +O\left(\Delta\omega_b^2(x)\right)+\phi_{tot,++}\Bigg]\Bigg\} \\
& +\cos\Bigg\{\Bigg[\left(\omega_m-\omega_b\right)t-\Delta\omega_b(x)\left(t-\Delta t+\frac{\omega_{min}+\frac{\omega_m}{2}}{\sigma}\right) \\
& +O\left(\Delta\omega_b^2(x)\right)+\phi_m\Bigg]\Bigg\} \\
\approx \frac{\mathcal{A}}{4}\Bigg\{ & \cos\left[\left(\omega_m+\omega_b\right)t+k_{min}\times\Delta R(x)+\phi_{tot,+-}\right] \\
& +\cos\left[\left(\omega_m-\omega_b\right)t-k_{min}\times\Delta R(x)+\phi_m\right]\Bigg\}
\end{aligned}
\tag{5.12}
$$

, where k_{min} is the wave number at the frequency ω_{min}, $\phi_{tot,++}=\phi_m+\Delta t\times\left(\omega_{min}-\frac{\omega_b+\omega_m}{2}\right)$, and $\phi_{tot,+-}=\phi_m-\Delta t\times\left(\omega_{min}+\frac{\omega_m-\omega_b}{2}\right)$. The last step of this calculation is justified by the fact that the model only applies during individual slopes. As a consequence, $(t-\Delta t)<T=\frac{2BW}{\sigma}<<\frac{\omega_{min}}{\sigma}$. In addition, $\omega_m<<\omega_{min}$. Therefore, $\left(t-\Delta t+\frac{\omega_{min}-\frac{\omega_m}{2}}{\sigma}\right)\approx\frac{\omega_{min}}{\sigma}$. The expression enables an interesting observation. While four components ($(\omega_m\pm\omega_b)\,t\pm k_{min}\times\Delta R(x)$) could have been expected, only two emerge. If a wave impinges from a target at an approximately infinite range, with an angle θ relative to the x axis in a 2D plane containing the target and the axis, the additional range can be expressed as $\Delta R=x\sin\theta$,

as shown in fig. 5.5.

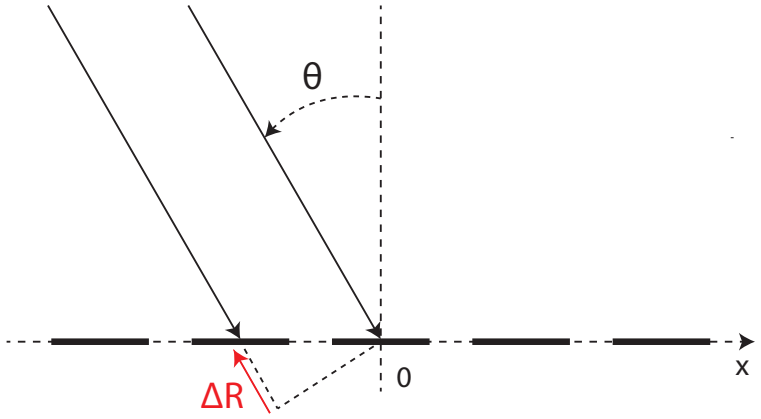

Figure 5.5: Reference schematic used for the calculation of the relative ranges of each receiving antenna, relative to the target

Therefore, in this case, eq. (5.12) can be written as:

$$B_{up,tag}(x) \approx \frac{\mathcal{A}}{4}\Big\{ \cos\left[(\omega_m + \omega_b)\, t + (k_{min} \sin\theta)\, x + \phi_{tot,++}\right] + \cos\left[(\omega_m - \omega_b)\, t - (k_{min} \sin\theta)\, x + \phi_{tot,+-}\right]\Big\} \tag{5.13}$$

The phase of the two components vary linearly over both time and position over the x axis. A 2D FFT should therefore uncover two peaks: one at the frequency of $(\omega_m + \omega_b)$ and seemingly coming from the θ direction, and another at the frequency of $(\omega_m - \omega_b)$ and coming from the $-\theta$ direction.

When the slope of the frequency variation is negative, the received signal can be expressed as:

$$B_{down,tag}(x) \approx \frac{\mathcal{A}}{4}\Big\{ \cos\left[(\omega_m + \omega_b)\, t - (k_{max} \sin\theta)\, x + \phi_{tot,-+}\right] + \cos\left[(\omega_m - \omega_b)\, t + (k_{max} \sin\theta)\, x + \phi_{tot,--}\right]\Big\} \tag{5.14}$$

, where k_{max} is the wave number at the frequency ω_{min}, $\phi_{tot,-+} = \phi_m + \Delta t \times \left(-\omega_{max} - \frac{\omega_b + \omega_m}{2}\right)$, and $\phi_{tot,--} = \phi_m - \Delta t \times \left(-\omega_{max} + \frac{\omega_m - \omega_b}{2}\right)$.

With a decreasing slope, the two peaks in the two remaining quadrants are generated: one at the frequency of $(\omega_m + \omega_b)$ and coming from the $-\theta$ direction, and another at the frequency of $(\omega_m - \omega_b)$ and coming from the θ direction. This process was simulated in Matlab by rudimentarily implementing the multiplication of the three sinusoidal processes—the delayed received signal, the LO, and the modulation of the tag—without using any of the approximations necessary to achieve the closed form results of eq. (5.13) and eq. (5.14). The code, given in chapter B, generated a simulated baseband signal, which was then processed using a 2D FFT, applied over both the time and antenna-number dimensions; the antennas effectively operate a sampling in one spacial dimension. A target placed at a distance of $5\,\mathrm{m}$ at an angle of $30°$, modulating its backscatter reflection at a frequency of $50\,\mathrm{kHz}$—interrogated by an 8-RX-channels FMCW reader using a triangular frequency modulation of $250\,\mathrm{MHz}$ in bandwidth and $200\,\mathrm{ms}$ in period—was simulated. Before the 2D FFT processing, the signal was zero-padded to expand its plotting to 40 angular directions and a 2D Hanning window was added to interpolate the data in both dimensions. The spectrum—a sum of the response over all the angular directions—was plotted and is shown in fig. 5.6. The response shows the couple of peaks predicted by eq. (5.11), centered on the modulation frequency and spaced by twice the beat frequency, ω_b. This allows the extraction of the both the tag's communicated information, as well as its range relative to the reader.

The magnitude of the 2D FFT computed after isolating the positive and negative slopes are plotted in fig. 5.7a and fig. 5.7b, respectively. These each show a single pair of peaks, covering complementary diagonals in the frequency/angle space. As predicted by eq. (5.13) and eq. (5.14), a positive angular slope results in a couple whose higher-frequency component appears to come from the direction of the target ($30°$, here), while that of its negatively-slopped counterpart seems to arrive from the conjugated direction, $-30°$.

Using this approach, it is therefore possible to determine the angle of arrival of the signal and, therefore, the angular direction of the tag. Combined with the spectral information,

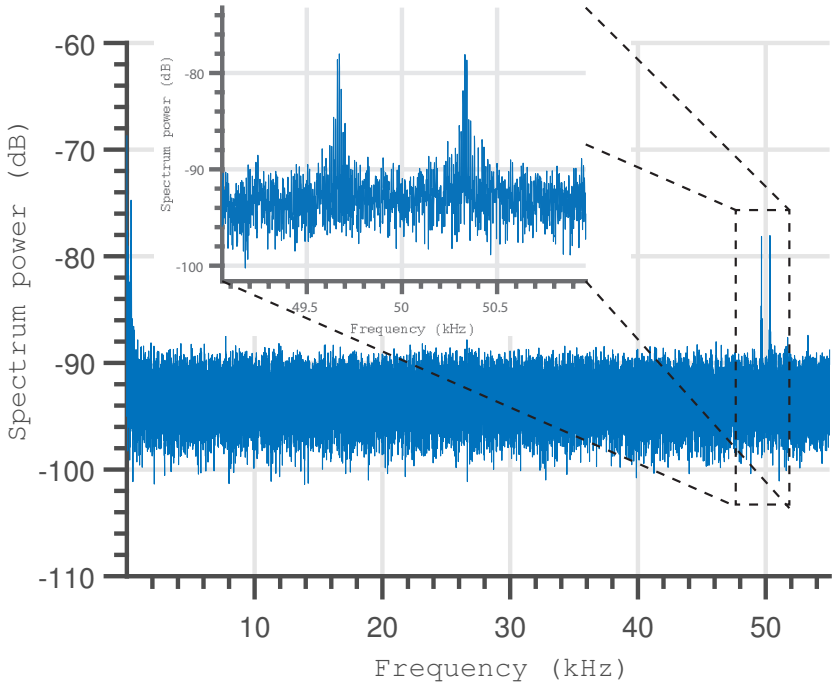

Figure 5.6: Baseband spectrum measured in the $0°$ direction for a broadsight backscatter target

the 2D position of the tag can, therefore, be measured using a single reader, while concurrently enabling its communications. The next section will demonstrate the implementation of this model using a low-cost automotive FMCW radar.

5.2.2 Measuring the position and identity of targets in space

Recent efforts have reported the use of the combination of FMCW schemes and active backscatter-modulating and amplifying targets for localization purposes [118, 119], which can be utilized to enable high-density implementations of dense and spatially-multiplexed tags. Nevertheless, the reported target/tags have remained extremely bulky (several cm in thickness) and power consuming (100s of mW) and the readers were large and costly. By combining the remarkable performance of the ultra-slim and ultra-low-power tags reported in chapter 4 with low-cost FMCW radar modules, the work presented in this section strives to propose an ultra-low-cost approach for the implementation of dense and spatially-localized and multiplexed sensing mm-wave tags.

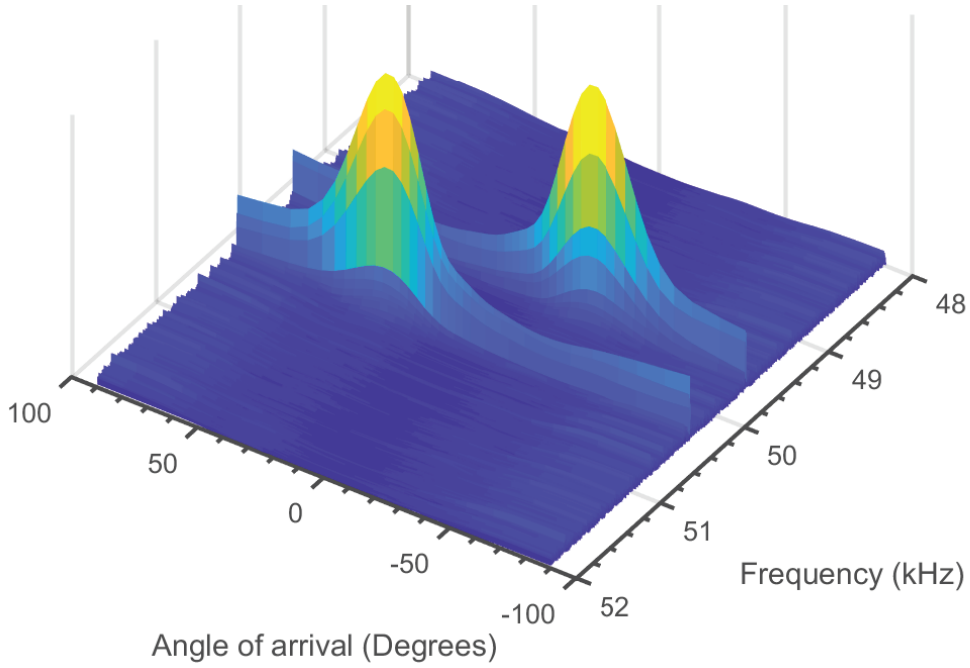

(a)

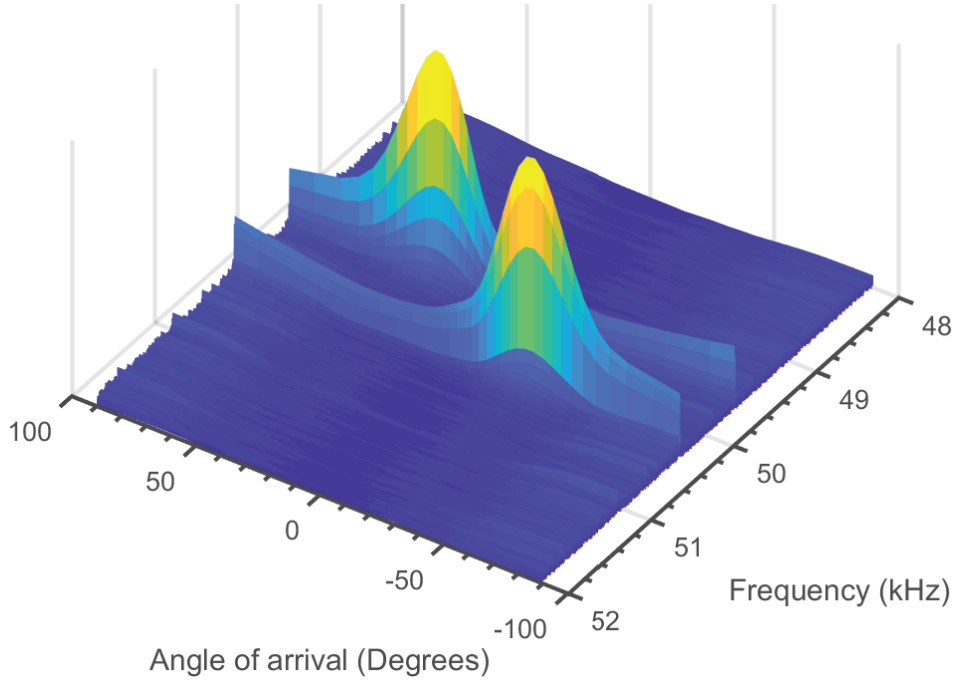

(b)

Figure 5.7: Output of the 2DFFT of the simulated response of the FMCW radar for the (a) positive and (b) negative frequency slope data

The FMCW radar/reader and its tag

FMCW radars were very specialized and expensive pieces of equipment that only a handfull of laboratories could get access to and justify the cost of. Thanks to the demands of automation and of the automotive industry, and to gradual technological advances in this field, it is now possible to acquire mm-wave FMCW radar modules for less than $20. Such a commoditization of this technology, and the associated progress in software-defined radios are opening a new landscape for innovative approaches for communications and the localization of mm-wave nodes.

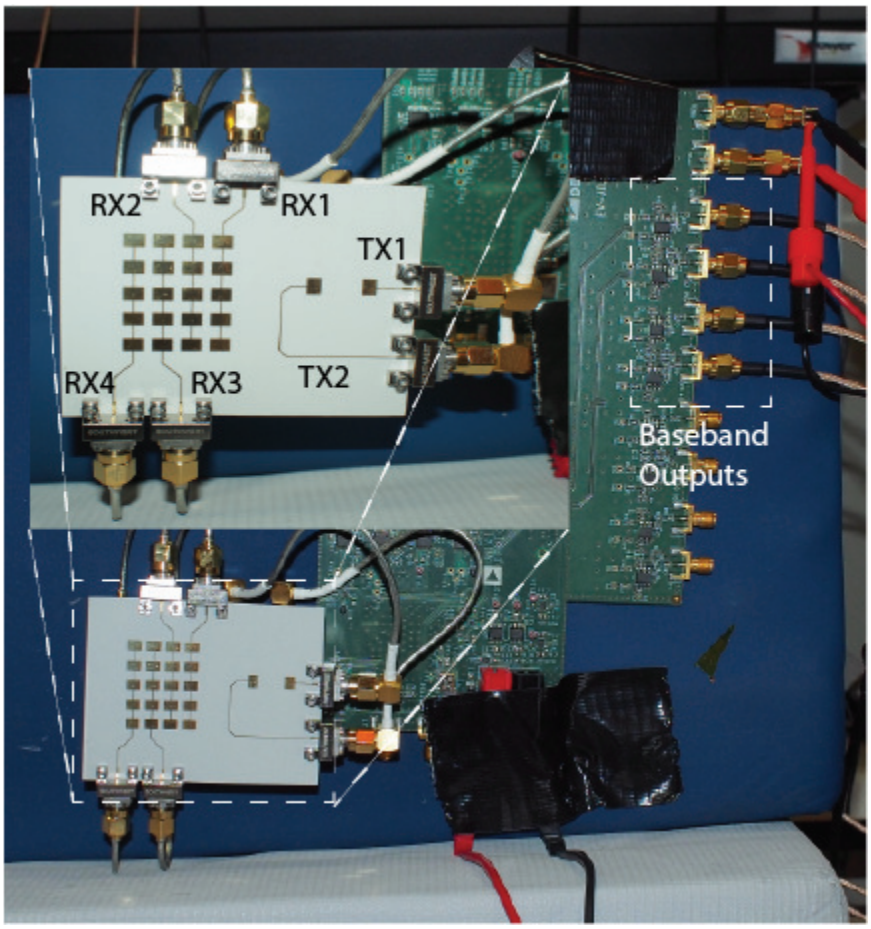

Figure 5.8: Picture of the reader setup used for the detection and identification of the tag/sensors, with a close-up on the custom-designed reader antenna

The reader used for this work is based on a low-cost $24\,\mathrm{GHz}$ chipset from Analog Devices. The $24\,\mathrm{GHz}$ to $24.25\,\mathrm{GHz}$ ISM band was adopted because of the abundant availabil-

ity of affordable radars that it offers, along with its proximity to the 28 GHz frequency used for the work of chapter 4 and, therefore, its compatibility with similar components and approaches where the tags are concerned. The commercially-available EV-RADAR-MMIC2 development board—comprising the ADF4159 PLL, the ADF5901 transmitter used for standard 24 GHz FMCW application, and a 4-channel ADF5904 receiver—was used for detection purposes. The down-converted baseband channels of the receiver were connected to an oscilloscope and the data was saved for processing, as shown in fig. 5.8. A custom array comprised of 4 linear antenna arrays for reception and 2 cross-polarized transmitting patch antennas was designed and fabricated onto a 12-mil-thick Rogers RO4003 substrate.

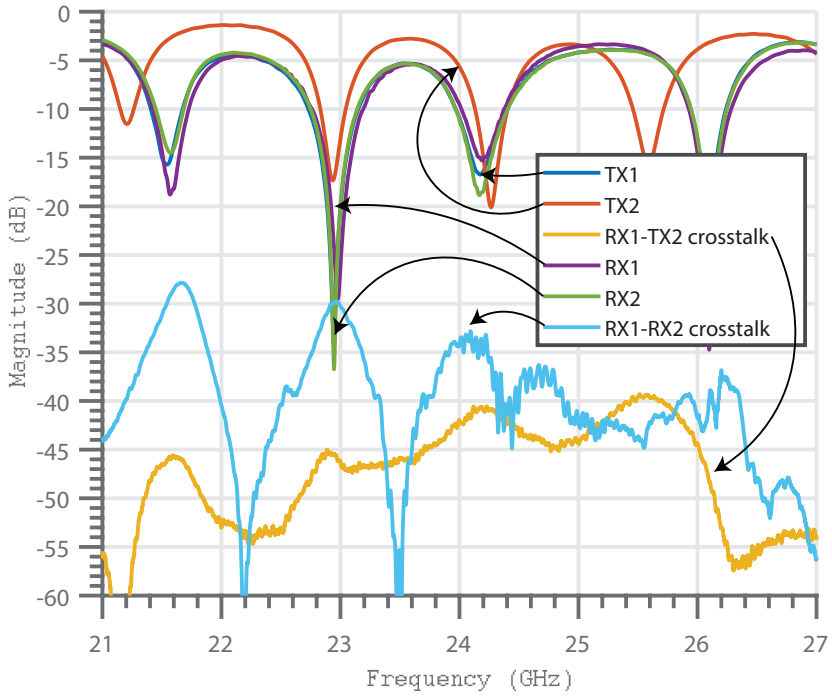

Figure 5.9: Measured S-parameters of the custom 2 by 4 reader antenna

The measured properties of the antenna are shown on fig. 5.9, displaying adequate performance for use in the 24 GHz to 24.25 GHz ISM frequency band. More importantly, the isolation between RX and TX is measured to be at least 40 dB. This rather high isolation, which could still be significantly improved, shows the benefits of the cross-polarizing approach in increasing the sensitivity of this compact reading system. Indeed, the main threat

to the sensitivity of a backscatter reader lies in leakage between the TX output and the RX channels. By cross-polarizing the antenna systems of these ports, their isolation can be enhanced and, consequently, so can the sensitivity of the radar module.

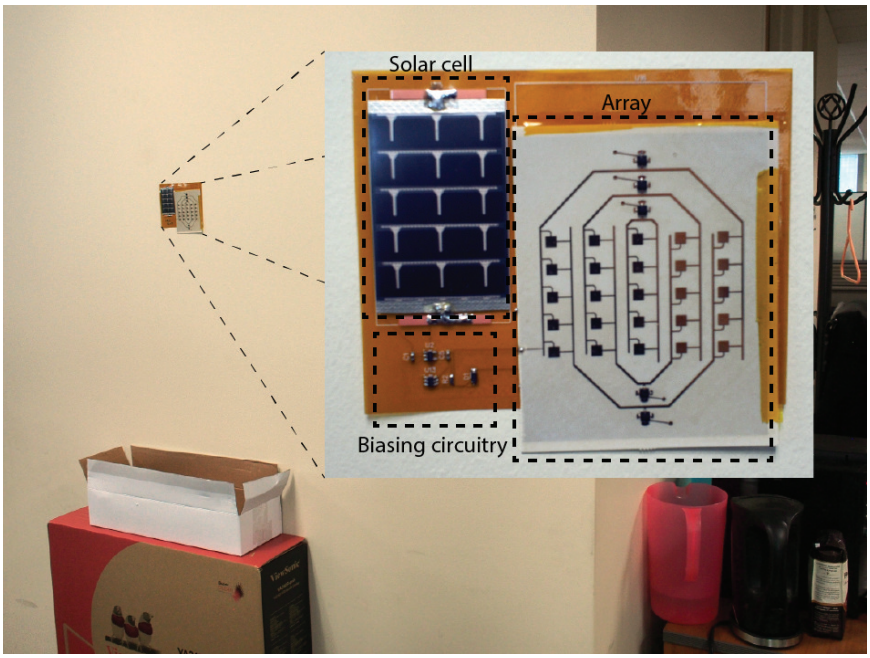

Figure 5.10: Picture of the assembled ultra-low-profile and micro-watt semi-passive Van-Atta $24\,\mathrm{GHz}$ reflectarray sensing tag

The reported semi-passive tag, shown in fig. 5.10, is very similar to that described in chapter 4. An ultra-low-power 555 timer (LTC6906), powered by a flexible amorphous silicon solar cell (MP3-25) inputed into a $1.8\,\mathrm{V}$ LT3009 regulator were used for this design. The baseband of the system was assembled onto a commercial flexible 5-mil-thick polyimide circuit board. The output of the timer was connected to a cross-polarizing retrodirective switchable patch-antenna array fabricated onto a 12-mil-thick Rogers RO4003 substrate and whose operation was centered at a frequency of $24.125\,\mathrm{GHz}$.

Data gathering and processing for AoA and range determination

A tag was placed at a distance of approximately $2\,\mathrm{m}$ and its modulation frequency was set at $40\,\mathrm{kHz}$. The baseband down-converted signals of the four channels of the reader were

fed to a multi-port oscilloscope and saved for a duration of $10\,\mathrm{s}$ at a $200\,\mathrm{kHz}$ sampling rate. A triangular modulation with a period of $10\,\mathrm{ms}$ and a bandwidth of $250\,\mathrm{MHz}$ was used for the FMCW process. The data was then imported into Matlab and arrayed as a 4 by 200000 matrix before zero-padding (252 additional rows, to reach a total of 256 angular samples) was applied in the small dimension of the matrix. The result of this operation was then processed using the same 2D FFT as the one used in the simulation code described in section 5.2.1. This yielded the spectrum shown on fig. 5.11.

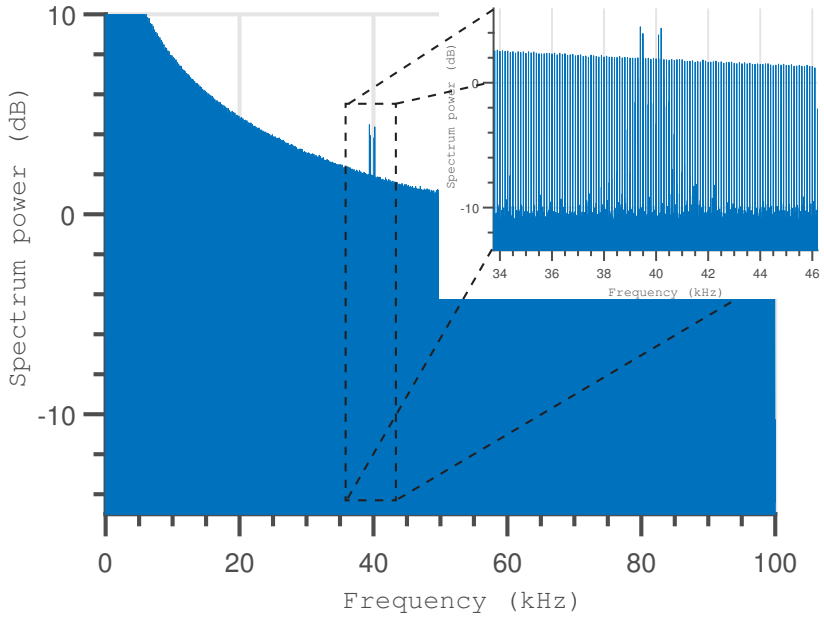

Figure 5.11: Measured spectrum of the tag's response measured by the FMCW reader

At first hand, it appears as if the products of the periodic FMCW triangular modulation are mostly hiding the response of the tag. Nevertheless, these only occupy a discrete set of frequency points ; these are the harmonics of the fundamental frequency of the slope modulation process, $f = \frac{1}{10\times10^{-3}}$. A straightforward solution to this problem would be to increase the modulation frequency of the timer on the tag. However, this is not ideal, as the power consumed by the tag increases with its modulation frequency. An alternative method, which was selected and applied in this work, removes the discrete set of frequency points occupied by the coherent self-interference. This can be applied as long as the tag's

modulation frequency is not closer to any of the reader-generated harmonics than the resolution of the measurement (here, $0.1\,\mathrm{Hz}$) allows. Once this processed was successfully applied, the spectrum shown in fig. 5.12 was extracted.

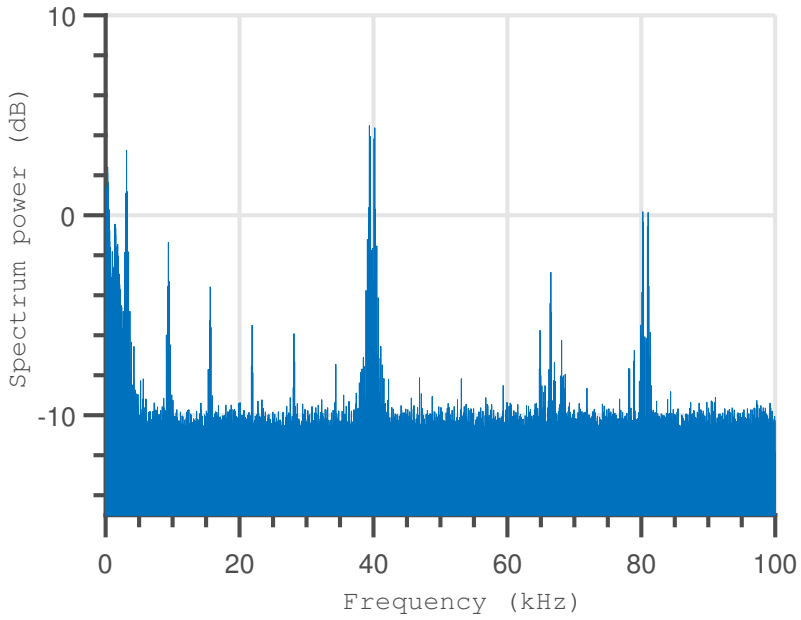

Figure 5.12: Measured spectrum after self-interference mitigation

The response is frequency-offset—both in its absolute value and in its support—from the typical FMCW response by the modulation frequency of the tag, thereby allowing high isolation from the interference from cross-talk and passive targets. In addition, the spectrum displays the expected double peak, their separation being twice the standard beat frequency associated with the range of the tag: $800\,\mathrm{Hz}$, which translates to a measured range of $R = \frac{800/2\times c\times 5\times 10^{-3}}{250\times 10^{6}} = 2.4\,\mathrm{m}$. A measurement at boresight was first taken, and utilized to calibrate the response of the channels. The calibration coefficients were chosen as the complex value of the spectrum measured for each channel at the frequency of the measured tag-created peak, at boresight. The calibration was then applied by dividing the data for each channel of the later measurements by these coefficients. The tag was then moved between different angular direction, at similar ranges. The results of the 2DFFT of these measurements, for the data gathered during positive modulation (according to the terminol-

ogy used in section 5.2.1), for 3 directions, are shown in fig. 5.13. The plots of fig. 5.13a, fig. 5.13c, and fig. 5.13e show 3-dimensional plots of the output of the 2DFFt, while that shown on fig. 5.13b, fig. 5.13d, and fig. 5.13f display a side view of the aforementioned plots, that displays only the data as a function of the extracted AoA.

The data matches perfectly the predictions made by both analytical and simulated approaches. Two peaks—diagonally spaced—emerge from the data. Due to the data being that gathered during positive modulation, the AoA associated with the peak of maximum frequency does, indeed, correspond to the direction of the tag. The FMCW process was, therefore, successfully applied for the localization of the tags described in chapter 4. This work demonstrated the use of a low-cost off-the-shelf FMCW system for the 2D localization of low-cost self-powered mm-wave backscatter tags, thereby opening the door for the emergence of unique RTLSs using the tags described in the previous chapters.

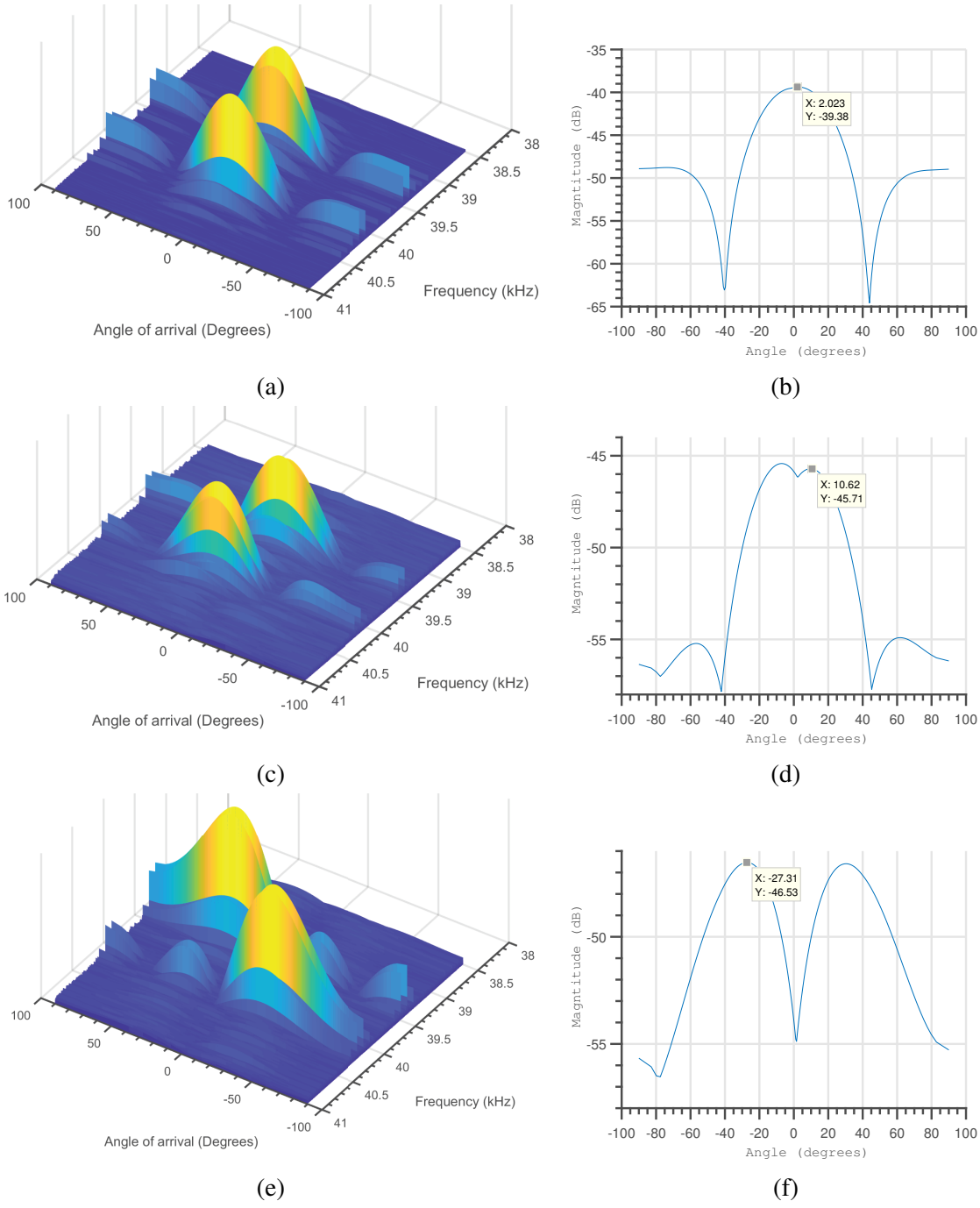

Figure 5.13: Output of the 2DFFT of the measured response of the radar for backscatter tags placed in the (a,d) $0°$, (b,e) $10°$, and (c,f) $-30°$ directions

CHAPTER 6
CONTRIBUTIONS AND FUTURE DIRECTIONS

6.1 Contributions

The goal of the work reported in this thesis was to achieve the implementation of skin-like battery-less gas-sensing devices for ubiquitous gas monitoring, and that of its associated reader infrastructure. The practical challenges set forward by the requirements of such a system were numerous and complex, and required the combination of innovative solutions in fields as disparate as nanomaterials science, additive manufacturing, semiconductor and electromagnetic physics, signal processing, and mm-wave antenna engineering. The results demonstrated by this work carry the mark of cross-fields pollination, enrichment, and synergies that have, holistically, resulted in a class of IoT devices that we have baptized *The Internet of Skins*. These advances can be grouped according to their contribution to the specifications of the skins:

- **Form factor and cost:** The need to develop low-cost skins resulted in the selection of low-cost additive approaches. The analysis presented in this thesis puts forth a strong argument for the selection of printed resistometric sensing approaches for such contexts. Additionally, the work states the need for operations at mm-wave frequencies, to allow the design of metal-backed and, therefore, surface agnostic sensing tags.

- **Sensitivity and consistency:** In the context of the printed resistometric strategy that had been identified, the optimization of these printed sensors for the detection of our target of interest, DMMP, was conducted. During this work, the hypotheses-directed trial and error process of materials selection and testing lead to the downselection of highly-purified semiconducting CNTs and of specific groups for their functionaliza-

tion, as well as to the surprising realization of the foremost importance of the metallic contacts (as opposed to that of the sensing film alone) on the sensitivity of the devices to DMMP ; a realization which subsequently branched out into a collaborative project whose results are reported in [120]. These combined improvements resulted in the increase of the sensitivity of printed nerve agent sensors by more than 400-fold, and consequently demonstrating the most sensitive fully-printed nerve agent sensors in the literature. Finally, the implementation of advanced inkjet-pattering techniques was demonstrated to reduce the variability of the printing process of these sensors down to a level that allowed same-batch sensitivity tolerances of better than $\pm 20\%$, down from orders of magnitude.

- **Range** constitutes one a such a wireless system's most crucial specifications. Indeed, once practically implemented, the density of readers required to cover a given area scales with the inverse squared of the maxiximum reliable communications range between the reader and the node: longer reading ranges translate to supralinear savings in infrastructure costs. This work extended the reading range of RFIDs by more than one order of magnitude. Indeed, motivated by the aforementioned considerations on form factor, mm-wave frequencies were adopted and demonstrated to enable a extension of RFID reading ranges, contrary to what common approximations may have led to believe. This work, as well, later resulted in collaborations which extended its performance and applicational reach [121, 122]. For reasons expanded upon in the next paragraph, the front-end was then implemented in a semi-passive backscatter system to demonstrate, at its time, the longest-ranging monostatic (TX and RX are co-located) unamplified-tag backscatter system ever reported.

- **Read-ability**, the ability to extract the relevant gas-sensing information from the tag, is a basic necessity for the devices at the center of this work. A possible mechanism for the extraction of sensing information from ultra-long-range chipless RFIDs—

by exploiting the humidity-dependent dielectric permittivity of their substrate—was demonstrated. However, this mechanism could not be converted to enable the sensing of the analytes of interest: nerve agents. This failure is fundamentally linked to our inability to engineer sensors whose resistance was small enough to influence passive, radiative structures (close to $377\,\Omega$, the impedance of free space), while preserving their sensitivity. Instead, the gap between the sensing and mm-wave communications work was bridged using the ultra-low-power-timer-enabled semi-passive backscatter scheme inspired by [64]. The scheme was then extended to propose an ultra-low-power baseband circuit capable of arraying several sensors and, for the first time, empower energy-autonomous wireless electronic noses.

- **Localization capabilities and spatial multiplexing**. The remarkable ability to enable ultra-low-cost tags with mm-wave communications abilities allows access to the unique capabilities of existing mm-wave hardware. Amongst these are low-cost mm-wave FMCW radars, which could allow for the developed tags to be localized in space. The work described here reported, for the first time, a low-cost system using self-powered mm-wave tags which can be detected in real time, in both angular and radial dimensions. This localization feature not only presents an applicational end in itself, but also allows the spatial multiplexing of tags, and therefore could increase the number of tags addressable by each reader.

6.2 Future directions

Many future directions can be envisioned, for efforts stemming from the work and results presented in this thesis.

- **Sensors** offer many avenues for improvements and future basic research projects.
  - There is no fundamental reason why low-resistance and sensitive gas sensors could not be printed, which would allow their integration into chipless tag archi-

tectures. More specifically, if the printing of repeatable sub-μm gaps between metal electrodes were achieved, the resistance of the sensors would decrease significantly.

  - The exact influence of the material of electrodes and of their porosity is not yet well quantified, controlled and understood. Basic research efforts in this direction could uncover rather fundamental and generalizable strategies that could be used to significantly enhance the performance of resistometric sensors, and bring about a new generation of ultra-low cost chemical sensors for the IoT.

- **Fully-printed mm-wave RFIDs:** The CNT semiconductors printing processes used and developed in this work for the fabrication of sensors could readily be applied for the design and fabrication of fully-printed semi-passive mm-wave RFIDs. Solution-processed CNTs have been demonstrated to appropriately serve as the semiconductor for FETs displaying operating frequencies in excess of $70\,\mathrm{GHz}$ [123]. If the printing of small electrode gaps and quality gate dielectrics were achieved, components such as mm-wave switches–and, therefore, fully-printed backscatterers—should be within reach.

- **mm-wave RFID:** While the work reported in this thesis has made it eminently clear that high path loss at mm-wave frequencies could be compensated—and even overturned–through the use of retrodirective structures, the emergence of fully-passive mm-wave RFIDs requires the tackling of a similar challenge for mm-wave harvesting. How can a large electrical structure be used to harvest energy in an approximately isotropic fashion? With such a challenge solved, the ultra-high EIRP 5G networks could provide a petri dish for yet impossible and inconcevable 5G-RFID-enabled applications.

- **Localization capabilities.** While more a bi-product of the pursuit of the original ubiquitous sensing goal, the localization capability of the mm-wave and ultra-low-

power backscatter nodes sets this system widely apart from existing commercial wireless RTLS technologies. The operation at mm-wave frequencies promises to provide highly-accurate ranging, while concurrently enabling angular localization abilities in compact low-cost MIMO readers. Combined with their sticker-like form factor and their ultra-low power-consumption, the approach presents an alternative to SOTA technologies (like UWB) that displays energy autonomy (thank to a thousand-fold smaller power consumption), does away with the need for triangulation, and allows conformal mounting (even on metal surfaces). Nevertheless, the following questions need to be addressed

- The limits and trade-offs in terms of reading-range, angular and radial accuracies, number of tags detectable by a single reader, data communication rates, and tag power consumption still need to be explored.
- The properties of retrodirective backscatter mm-wave channels in various environments could benefit from a great deal of study and modeling. These are expected to be very different from their direct, lower-frequency counterparts, and to have a great influence on the ranging performance of the system.

The wireless technology developed and presented in this thesis initially was intended to serve real-time, remote gas sensing applications. Nevertheless its specifications as a real-time localization technology offer striking advantages relative to that of the commercial SOTA, as shown in table 6.1.

Therein lies, arguably, the most attractive appeal of this technology and it is the author's hope that this observation will motivate many to contribute to this promising area of research.

Technology	Reading range (km)	Localization accuracy (cm)	Power consumption (mW)	Minimum number of "readers"	Controlled and consistent connectivity
This technology	1	1	0.02	1	YES
BLE	0.4	100	20	3	YES
UWB	0.3	10	400	3	YES
DGPS	Global	10	4000	4	NO

Table 6.1: Comparing the potential performance of the mm-wave backscatter approach to that of the commercial SOTA

Appendices

APPENDIX A

EXPERIMENTAL EQUIPMENT

A Flexstream gas standard generator from KIN-TEK was used to generate controlled concentrations of analytes in a carrier gas. Here, we used ultra pure nitrogen for that purpose. This system utilizes permeation tubes that have a set permeation rate for the analyte gas:the tube permeates the analyte into the diluent gas. The concentration is therefore controlled by the flow rate—generally given in sccm (Standard Cubic Centimeters per Minute)—inversely proportional to the output flow rate. A custom-made gas chamber (Figure A.1) was fabricated to confine the sensors during the gas exposure tests. The chamber is fed through one end by the output of the Flexstream and the gas is exhausted through a small tube at the other end of the box. Cables are brought into the box in an airtight fashion and connect the leads of the electrodes to an Agilent 34401A digital multimeter.

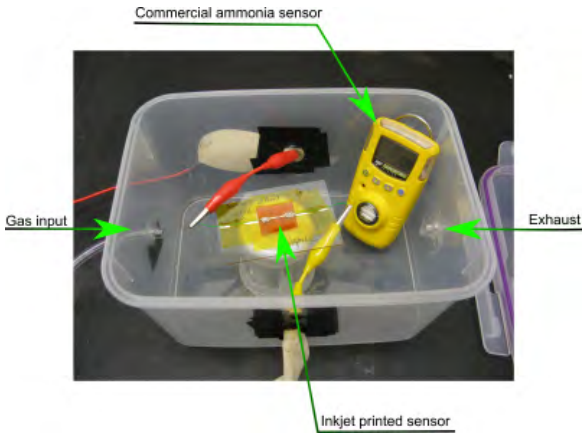

Figure A.1: Test enclosure including the tested inkjet printed sensor and the commercial ammonia reference gas sensor

Later on, a new testing system was assembled, that relies on a PXI system from National Instruments, shown in fig. A.2. The sensor test bench's new feature, relative to that shown in fig. A.2 is its ability to test up to 16 sensors simultaneously and to, therefore, enable the acquisition of very valuable consistency metrics for the printed sensors.

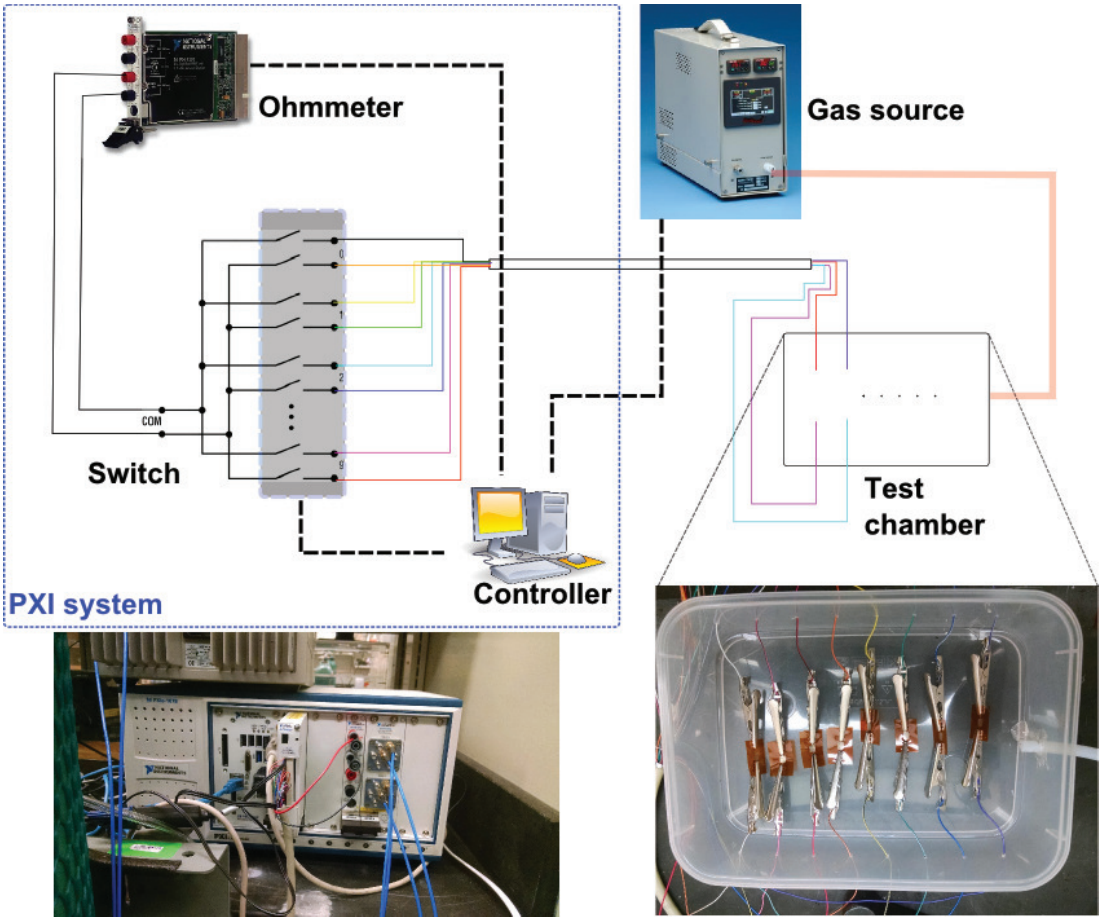

Figure A.2: Improved gas sensors test system enabling the simultaneous characterization of several devices

APPENDIX B

FMCW MODELING MATLAB SCRIPT

The following Matlab script is the one that was used to simulate the MISO FMCW process, and whose results were presented and commented upon in section 5.2.1.

```
close all
clear all
c = 3e8 ; % in m/s

% Reader properties
P_emit = 10^(20/10) ; % Emitted power, in dBm
TX_amplification = 10^(0/10) ; % Additional amplification added at the input of the RX
    channels, in dB
G_reader_antenna = 10^(12/10) ; % Gain of the reader antenna, in dBi
Isolation_1 = 10^(-100/10) ; % Isolation between the TX antenna and its nearest RX antenna
    , in dB
Isolation_increment = 10^(-1) ; % Incremental isolation for each additional antenna, in dB
RX_TX_IC_isolation = 10^(-100/10) ; % ON-chip RX/TX isolation, in dB
d_inter_antennas = 6e-3; % Distance between antennas, in m
N_antennas = 8 ; % Number of RX antennas
fmin = 24e9 ; % Minimum frequency of the band used by the radar, in Hz
fmax = 24.25e9 ; % Maximum frequency of the band used by the radar, in Hz
mu = 0 ; % Phase noise mean of the LO of the radar
sigma = 1e-6 ; % Phase noise standard deviation of the LO of the radar
T_chirp = 100e-3 ; % Period of the total triangular frequency pattern, in s
T_switch = 10e-9 ; % Time taken by the LO to switch from one frequency to another, in s
N_f_steps = 2^14 ; % Number of frequency steps in the slope
Cuttoff_PLL = 1*N_f_steps/T_chirp ;

% Baseband sampling properties
tmax = 1; % Sampling time, in s
sampling_rate = 200e3 ; % Sampling rate of the baseband ADC, in Hz
N_angle_steps = 40 ; % Number of angular points plotted
slope = 'pos' ; % Slope of the data whose 2D FFT is plotted

% Target properties
RCS_tag = 10^(-25/10) ; % RCS of tags, in dBsm
```

```
f_osc_targets = [50]*1e3 ; % Switching frequency of tags, in Hz
R_targets = [10]*1e0; % Range of tags, in m
Angle_targets = [30] ; % Angle of tags, in degrees


% Simulations
% Generate the time
t_period = linspace(0, T_chirp, T_chirp*sampling_rate) ;
time = linspace(0, tmax, tmax*sampling_rate) ;

% Generate phase noise
PN_norm = normrnd(mu,sigma,1,length(time)) ;
PN = cumsum(2*pi*fmin/sampling_rate*PN_norm) ;

% Generate source signal in frequency space
% Generate the LO signal
signal_source_f_period = zeros(1,T_chirp*sampling_rate) ;
for i=1:T_chirp*sampling_rate
   if t_period(i)<T_chirp/2
      if mod(t_period(i),T_chirp./(2*N_f_steps))<(T_chirp/(2*N_f_steps)-T_switch)
         signal_source_f_period(i) = fmin+(fmax-fmin)/N_f_steps*floor(2*N_f_steps*t_period
             (i)/T_chirp);
      else
         x = (mod(t_period(i),T_chirp./(2*N_f_steps))-(T_chirp/(2*N_f_steps)-T_switch))/(
             T_switch) ;
         signal_source_f_period(i) = fmin+((fmax-fmin)/N_f_steps*(floor(2*N_f_steps*
             t_period(i)/T_chirp)+1))*x+((fmax-fmin)/N_f_steps*floor(2*N_f_steps*t_period(
             i)/T_chirp))*(1-x);
      end
   else
      if mod((t_period(i)-T_chirp/2),T_chirp./(2*N_f_steps))<(T_chirp/(2*N_f_steps)-
          T_switch)
         signal_source_f_period(i) = fmax-(fmax-fmin)/N_f_steps*floor(2*N_f_steps*(
             t_period(i)-T_chirp/2)/T_chirp);
      else
         x = (mod(t_period(i),T_chirp./(2*N_f_steps))-(T_chirp/(2*N_f_steps)-T_switch))/(
             T_switch) ;
         signal_source_f_period(i) = fmax-((fmax-fmin)/N_f_steps*(floor(2*N_f_steps*(
             t_period(i)-T_chirp/2)/T_chirp)+1))*x-((fmax-fmin)/N_f_steps*(floor(2*
             N_f_steps*(t_period(i)-T_chirp/2)/T_chirp)))*(1-x);
      end
```

```
   end
end

% Generate source signal in time_domain
signal_source_f = repmat(signal_source_f_period,1,floor(tmax/T_chirp));
signal_source_f = [signal_source_f signal_source_f_period(1:(tmax-T_chirp*floor(tmax/
    T_chirp))*sampling_rate)] ;

% Apply the filtering of the PLL
if Cuttoff_PLL/(sampling_rate/2)<1
   [b,a] = butter(6,Cuttoff_PLL/(sampling_rate/2)) ;
   signal_source_f = filter(b,a,signal_source_f) ;
end

% Generate phase of the signal
phase_f = 2*pi/sampling_rate*cumsum(signal_source_f) ;
signal_source_I = cos(phase_f+pi.*PN) ;
signal_source_Q = sin(phase_f+pi.*PN) ;

% Target modulation signal
modulation = zeros(length(R_targets),length(time));
for i=1:length(f_osc_targets) % Generate modulation for each target
   modulation(i,:) = (ones(1,length(time))+sin(2*pi*f_osc_targets(i)*time))/.2;
end

% Generate received signal
measurement_targets = zeros(N_antennas,length(time)) ;
Propagation_losses = P_emit*RCS_tag*(G_reader_antenna*c./(4*pi*fmin*R_targets.^2)).^2 ;
for j=1:N_antennas % Generate the contribution of the crosstalk, and then that of each
    target
      % Calculate propagation between TX antenna and this RX antenna
      tshift = d_inter_antennas/c*(j-1)*ones(size(time)) ;
      phase_f_shift = interp1(time, phase_f, time-tshift) ; % Applying the delay
      phase_f_shift(1) = phase_f(1) ;
      PN_shift = interp1(time, PN, time-tshift) ;
      PN_shift(1) = PN(1) ;
      Isolation = Isolation_1*Isolation_increment ;
      signal_source_I_shift = cos(phase_f_shift+pi.*PN_shift) ;
      measurement_targets(j,:) = P_emit*signal_source_I*(RX_TX_IC_isolation+Isolation*
          TX_amplification).*signal_source_I_shift; % Self-interference
   for i=1:length(f_osc_targets)
```

```
        % Generate shifted signal for each target
        tshift = 2*R_targets(i)/c*ones(size(time)) ;
        phase_f_shift = interp1(time, phase_f, time-tshift) ;
        phase_f_shift(1) = phase_f(1) ;
        PN_shift = interp1(time, PN, time-tshift) ;
        PN_shift(1) = PN(1) ;
        signal_source_I_shift = cos(phase_f_shift+pi.*PN_shift+2*pi*d_inter_antennas*fmin/c
            *(j-1)*sin(Angle_targets(i)*pi/180)) ;
        signal_target = Propagation_losses(i).*modulation(i,:).*signal_source_I_shift*
            TX_amplification ;
        measurement_targets(j,:) = measurement_targets(j,:)+signal_source_I.*signal_target ;
    end
end
measurement_targets = [measurement_targets ; zeros(N_angle_steps-N_antennas, size(
    signal_source_f,2))] ;


% Determine the value of corresponding Fourrier domains
f = [1:length(signal_source_I)]./(length(signal_source_I))*sampling_rate ; % Frequency
    space
I_plot = f>min(f_osc_targets)/2 & f<1.2*max(f_osc_targets) ; % Determines the plotting
    range
% Angular space
sinTheta = 2*c/((fmax+fmin)*d_inter_antennas)*((1:N_angle_steps+1)./(N_angle_steps)
    -(0.5+1/N_angle_steps)*ones(size(N_angle_steps))) ;
ind = find(sinTheta>1) ;
sinTheta(ind) = 1 ;
ind = find(sinTheta<-1) ;
sinTheta(ind) = -1 ;
Theta = asin(sinTheta)*180/pi,floor(N_angle_steps/2) ;


% Applying the FFTs
% Selecting what slope is processed
if slope=='pos'
    measurement_targets = measurement_targets.*(1+square(2*time/T_chirp*pi))/2 ;
elseif slope=='neg'
    measurement_targets = measurement_targets.*(1+square(2*time/T_chirp*pi-pi))/2 ;
end
% Generating the windows
Hann_f = hann(length(time)); % Hanning window
```

```
Hann_Theta = hann(N_angle_steps); % Hanning window
window = Hann_Theta*Hann_f' ;
% Applying the windows
measurement_targets_frequency = fft2(window.*(measurement_targets+eps*ones(size(
    measurement_targets)))./length(signal_source_I) ;
measurement_targets_frequency = circshift(measurement_targets_frequency,floor((
    N_angle_steps+1)/2),1) ;
measurement_targets_frequency = [measurement_targets_frequency ;
    measurement_targets_frequency(1,:)] ;


% Ploting
% Spectrum
plot(f(I_plot)*1e-3,10*log10(sum(abs(measurement_targets_frequency(:,I_plot)),1)))
hXLabel = xlabel('Frequency (kHz)');
hYLabel = ylabel('Spectrum power (dB)');
set( gca                , ...
   'FontSize' , 13     , ...
   'FontName' , 'Helvetica' );
set([hXLabel, hYLabel], ...
   'FontName' , 'AvantGarde');
set([hXLabel, hYLabel] , ...
   'FontSize' , 13     );
set(gca, ...
  'Box'      , 'off'  , ...
  'TickDir'  , 'out'  , ...
  'TickLength' , [.03 .03] , ...
  'XMinorTick' , 'on' , ...
  'YMinorTick' , 'on' , ...
  'XGrid'    , 'on'   , ...
  'YGrid'    , 'on'   , ...
  'XColor'   , [.3 .3 .3], ...
  'YColor'   , [.3 .3 .3], ...
  'YTick'    , -160:10:0, ...
  'LineWidth' , 2     );
axis([min(f(I_plot)*1e-3) max(f(I_plot)*1e-3) -110 -60])

% 2D FFT in cartesian coordinates
figure
maximum = max(10*log10(abs(measurement_targets_frequency(:,I_plot)))) ;
surface(Theta,f(I_plot)*1e-3,exp(abs(measurement_targets_frequency(:,I_plot)))', '
```

```
    LineStyle', 'none' )
view(2)
hXLabel = ylabel('Frequency (kHz)');
hYLabel = xlabel('Angle of arrival (Degrees)');
set( gca                 , ...
   'FontSize' , 13      , ...
   'FontName' , 'Helvetica' );
set(gca, ...
  'Box'      , 'off'   , ...
  'TickDir'  , 'out'   , ...
  'TickLength' , [.03 .03] , ...
  'XMinorTick' , 'on' , ...
  'YMinorTick' , 'on' , ...
  'XGrid'    , 'on'    , ...
  'YGrid'    , 'on'    , ...
  'XColor'   , [.3 .3 .3], ...
  'YColor'   , [.3 .3 .3], ...
  'LineWidth' , 2     );
ax1 = gca;             % gca = get current axis
ax1.ZAxis.Visible = 'off'; % remove y-axis
view([-1,1.5,2.5])

% 2D FFT in polar coordinates
figure
maximum = max(10*log10(abs(measurement_targets_frequency(:,I_plot)))) ;
[R PHI] = meshgrid(f(I_plot)*1e-3,Theta);
Z = abs(measurement_targets_frequency(:,I_plot)) ;
surf(R.*sin(PHI*pi/180), R.*cos(PHI*pi/180), Z, 'LineStyle', 'none' );
view(2)
set( gca                 , ...
   'FontSize' , 13      , ...
   'FontName' , 'Helvetica' );
set(gca, ...
  'visible'    , 'off'  ,...
  'Box'      , 'off'   , ...
  'TickDir'  , 'out'   , ...
  'TickLength' , [.03 .03] , ...
  'XMinorTick' , 'on' , ...
  'YMinorTick' , 'on' , ...
  'XGrid'    , 'on'    , ...
  'YGrid'    , 'on'    , ...
```

```
'XColor'   , [.3 .3 .3], ...
'YColor'   , [.3 .3 .3], ...
'LineWidth' , 2     );
```

REFERENCES

[1] R. Pride, J. Hodgkinson, M. Padget, B. Van Well, R. Strzoda, C. T. Siemens, and G. Munich, "Implementation of optical technologies for portable gas leak detection," in *Proc. Int. Gas Research Conf., IGRC, Vancouver, Canada*, 2004.

[2] B. van Well, S. Murray, J. Hodgkinson, R. Pride, R. Strzoda, G. Gibson, and M. Padgett, "An open-path, hand-held laser system for the detection of methane gas," *J. Opt. A: Pure Appl. Opt.*, vol. 7, no. 6, S420, May 2005.

[3] J. Hodgkinson and R. P. Tatam, "Optical gas sensing: a review," *Meas. Sci. Technol.*, vol. 24, no. 1, p. 012 004, Nov. 2012.

[4] N. Gopalsami and A. C. Raptis, "Millimeter-wave radar sensing of airborne chemicals," *IEEE Trans. Microw. Theory Tech.*, vol. 49, no. 4, pp. 646–653, 2001.

[5] A. W. Snow, F. K. Perkins, M. G. Ancona, J. T. Robinson, E. S. Snow, and E. E. Foos, "Disordered Nanomaterials for Chemielectric Vapor Sensing: A Review," *IEEE Sens. J.*, vol. 15, no. 3, pp. 1301–1320, Mar. 2015.

[6] S. Kim, R. Vyas, J. Bito, K. Niotaki, A. Collado, A. Georgiadis, and M. M. Tentzeris, "Ambient RF Energy-Harvesting Technologies for Self-Sustainable Standalone Wireless Sensor Platforms," *IEEE_J_PROC*, vol. 102, no. 11, pp. 1649–1666, Nov. 2014.

[7] C. Gomez, J. Oller, and J. Paradells, "Overview and Evaluation of Bluetooth Low Energy: An Emerging Low-Power Wireless Technology," *Sensors*, vol. 12, no. 9, pp. 11 734–11 753, Aug. 2012.

[8] J. Kimionis and M. M. Tentzeris, "Pulse shaping: The missing piece of backscatter radio and RFID," *IEEE Trans. Microw. Theory Tech.*, vol. 64, no. 12, pp. 4774–4788, 2016.

[9] D. Dcshank. (2012). Double side printed circuit board process flow chart, (visited on 03/15/2019).

[10] J. G. Hester, S. Kim, J. Bito, T. Le, J. Kimionis, D. Revier, C. Saintsing, W. Su, B. Tehrani, A. Traille, *et al.*, "Additively manufactured nanotechnology and origami-enabled flexible microwave electronics," *Proceedings of the IEEE*, vol. 103, no. 4, pp. 583–606, 2015.

[11] R. Gonçalves, S. Rima, R. Magueta, P. Pinho, A. Collado, A. Georgiadis, J. Hester, N. B. Carvalho, and M. M. Tentzeris, "Rfid-based wireless passive sensors utilizing cork materials," *IEEE Sensors Journal*, vol. 15, no. 12, pp. 7242–7251, 2015.

[12] J. S. Chang, A. F. Facchetti, and R Reuss, "A Circuits and Systems Perspective of Organic/Printed Electronics: Review, Challenges, and Contemporary and Emerging Design Approaches," *IEEE Journal on Emerging and Selected Topics in Circuits and Systems*, vol. 7, no. 1, pp. 7–26, Mar. 2017.

[13] P. Lecourt. (2012). Thinfilm, https://flic.kr/p/obkyke, (visited on 03/15/2019).

[14] D. Baran, R. S. Ashraf, D. A. Hanifi, M. Abdelsamie, N. Gasparini, J. A. Röhr, S. Holliday, A. Wadsworth, S. Lockett, M. Neophytou, C. J. M. Emmott, J. Nelson, C. J. Brabec, A. Amassian, A. Salleo, T. Kirchartz, J. R. Durrant, and I. McCulloch, "Reducing the efficiency–stability–cost gap of organic photovoltaics with highly efficient and stable small molecule acceptor ternary solar cells," *Nat. Mater.*, vol. 16, p. 363, Nov. 2016.

[15] B. Derby, "Inkjet Printing of Functional and Structural Materials: Fluid Property Requirements, Feature Stability, and Resolution," *Annu. Rev. Mater. Res.*, vol. 40, no. 1, pp. 395–414, Jun. 2010.

[16] J. R. Stetter and J. Li, "Amperometric gas sensors a review," *Chemical reviews*, vol. 108, no. 2, pp. 352–366, 2008.

[17] J. Fouletier, "Gas analysis with potentiometric sensors. a review," *Sensors and Actuators*, vol. 3, pp. 295–314, 1983.

[18] S. Heinze, J. Tersoff, R. Martel, V. Derycke, J. Appenzeller, and P. Avouris, "Carbon nanotubes as schottky barrier transistors," *Physical Review Letters*, vol. 89, no. 10, p. 106 801, 2002.

[19] S. Patel, T. Mlsna, B Fruhberger, E Klaassen, S Cemalovic, and D. Baselt, "Chemicapacitive microsensors for volatile organic compound detection," *Sensors and Actuators B: Chemical*, vol. 96, no. 3, pp. 541–553, 2003.

[20] E. Snow, F. Perkins, E. Houser, S. Badescu, and T. Reinecke, "Chemical detection with a single-walled carbon nanotube capacitor," *Science*, vol. 307, no. 5717, pp. 1942–1945, 2005.

[21] W. H. Brattain and J. Bardeen, "Surface properties of germanium," *Bell System Technical Journal*, vol. 32, no. 1, pp. 1–41, 1953.

[22] N. Yamazoe, "New approaches for improving semiconductor gas sensors," *Sensors and Actuators B: Chemical*, vol. 5, no. 1-4, pp. 7–19, 1991.

[23] J. G. Hester and M. M. Tentzeris, "Inkjet-printed van-atta reflectarray sensors: A new paradigm for long-range chipless low cost ubiquitous smart skin sensors of the internet of things," in *Microwave Symposium (IMS), 2016 IEEE MTT-S International*, IEEE, 2016, pp. 1–4.

[24] W. Chu, V Leonhard, H Erdmann, and M Ilgenstein, "Thick-film chemical sensors," *Sensors and Actuators B: Chemical*, vol. 4, no. 3-4, pp. 321–324, 1991.

[25] J. R. Stetter, E. F. Stetter, D. Ebeling, M. Findlay, and V. Patel, *Printed gas sensor*, US Patent App. 12/953,672, 2010.

[26] K. Wallgren and S. Sotiropoulos, "Oxygen sensors based on a new design concept for amperometric solid state devices," *Sensors and Actuators B: Chemical*, vol. 60, no. 2, pp. 174–183, 1999.

[27] J. Zhao, Y. Yu, B. Weng, W. Zhang, A. T. Harris, A. I. Minett, Z. Yue, X.-F. Huang, and J. Chen, "Sensitive and selective dopamine determination in human serum with inkjet printed nafion/MWCNT chips," *Electrochemistry Communications*, vol. 37, pp. 32–35, 2013.

[28] Y. Jung, H. Park, J.-A. Park, J. Noh, Y. Choi, M. Jung, K. Jung, M. Pyo, K. Chen, A. Javey, *et al.*, "Fully printed flexible and disposable wireless cyclic voltammetry tag," *Scientific reports*, vol. 5, 2015.

[29] J. G. Hester, M. M. Tentzeris, and Y. Fang, "Inkjet-printed, flexible, high performance, carbon nanomaterial based sensors for ammonia and DMMP gas detection," in *Microwave Conference (EuMC), 2015 European*, IEEE, 2015, pp. 857–860.

[30] ——, "UHF lumped element model of a fully-inkjet-printed single-wall-carbon-nanotube-based inter-digitated electrodes breath sensor," in *IEEE 2016 Antennas and Propagation Society International Symposium (APSURSI)*, IEEE, 2016.

[31] K. Skucha, Z. Fan, K. Jeon, A. Javey, and B. Boser, "Palladium/silicon nanowire schottky barrier-based hydrogen sensors," *Sensors and Actuators B: Chemical*, vol. 145, no. 1, pp. 232–238, 2010.

[32] H. J. Yoon, J. H. Yang, Z. Zhou, S. S. Yang, M. M.-C. Cheng, *et al.*, "Carbon dioxide gas sensor using a graphene sheet," *Sensors and Actuators B: Chemical*, vol. 157, no. 1, pp. 310–313, 2011.

[33] J. Jang, J. Ha, and J. Cho, "Fabrication of water-dispersible polyaniline-poly (4-styrenesulfonate) nanoparticles for inkjet-printed chemical-sensor applications," *Advanced Materials*, vol. 19, no. 13, pp. 1772–1775, 2007.

[34] V. Dua, S. P. Surwade, S. Ammu, S. R. Agnihotra, S. Jain, K. E. Roberts, S. Park, R. S. Ruoff, and S. K. Manohar, "All-organic vapor sensor using inkjet-printed reduced graphene oxide," *Angewandte Chemie International Edition*, vol. 49, no. 12, pp. 2154–2157, 2010.

[35] P. Qi, O. Vermesh, M. Grecu, A. Javey, Q. Wang, H. Dai, S. Peng, and K. Cho, "Toward large arrays of multiplex functionalized carbon nanotube sensors for highly sensitive and selective molecular detection," *Nano letters*, vol. 3, no. 3, pp. 347–351, 2003.

[36] C. Bittencourt, A. Felten, E. Espinosa, R. Ionescu, E. Llobet, X. Correig, and J.-J. Pireaux, "WO 3 films modified with functionalised multi-wall carbon nanotubes: Morphological, compositional and gas response studies," *Sensors and Actuators B: Chemical*, vol. 115, no. 1, pp. 33–41, 2006.

[37] Y. Lu, J. Li, J. Han, H.-T. Ng, C. Binder, C. Partridge, and M Meyyappan, "Room temperature methane detection using palladium loaded single-walled carbon nanotube sensors," *Chemical Physics Letters*, vol. 391, no. 4, pp. 344–348, 2004.

[38] J. Novak, E. Snow, E. Houser, D Park, J. Stepnowski, and R. McGill, "Nerve agent detection using networks of single-walled carbon nanotubes," *Applied physics letters*, vol. 83, no. 19, pp. 4026–4028, 2003.

[39] J. Li, Y. Lu, Q. Ye, M. Cinke, J. Han, and M Meyyappan, "Carbon nanotube sensors for gas and organic vapor detection," *Nano letters*, vol. 3, no. 7, pp. 929–933, 2003.

[40] K. A. Mirica, J. M. Azzarelli, J. G. Weis, J. M. Schnorr, and T. M. Swager, "Rapid prototyping of carbon-based chemiresistive gas sensors on paper," *Proceedings of the National Academy of Sciences*, vol. 110, no. 35, E3265–E3270, 2013.

[41] Y. Lu, C. Partridge, M Meyyappan, and J. Li, "A carbon nanotube sensor array for sensitive gas discrimination using principal component analysis," *Journal of Electroanalytical Chemistry*, vol. 593, no. 1, pp. 105–110, 2006.

[42] A. Star, V. Joshi, S. Skarupo, D. Thomas, and J.-C. P. Gabriel, "Gas sensor array based on metal-decorated carbon nanotubes," *The Journal of Physical Chemistry B*, vol. 110, no. 42, pp. 21 014–21 020, 2006.

[43] J. R. Windmiller and J. Wang, "Wearable electrochemical sensors and biosensors: A review," *Electroanalysis*, vol. 25, no. 1, pp. 29–46, 2013.

[44] C. B. Jacobs, M. J. Peairs, and B. J. Venton, "Review: Carbon nanotube based electrochemical sensors for biomolecules," *Analytica Chimica Acta*, vol. 662, no. 2, pp. 105–127, 2010.

[45] D. Lochun, E. Zeira, and R. Menize, "Reel-to-reel manufacturability of flexible electrical interconnects and radio-frequency identification structures," in *52nd Electronic Components and Technology Conference 2002. (Cat. No.02CH37345)*, ieeexplore.ieee.org, 2002, pp. 686–689.

[46] L. Yang, A. Rida, R. Vyas, and M. M. Tentzeris, "RFID Tag and RF Structures on a Paper Substrate Using Inkjet-Printing Technology," *IEEE Trans. Microw. Theory Tech.*, vol. 55, no. 12, pp. 2894–2901, Dec. 2007.

[47] B. Tehrani, J. R. Cooper, and M. M. Tentzeris, "Multilayer inkjet printing of millimeter-wave proximity-fed patch arrays on flexible substrates," *IEEE Antennas Wirel. Propag. Lett.*, 2013.

[48] B. S. Cook, J. R. Cooper, and M. M. Tentzeris, "Multi-Layer RF Capacitors on Flexible Substrates Utilizing Inkjet Printed Dielectric Polymers," *IEEE Microwave Compon. Lett.*, vol. 23, no. 7, pp. 353–355, Jul. 2013.

[49] G. McKerricher, M. Vaseem, and A. Shamim, "Fully inkjet-printed microwave passive electronics," *Microsystems &Amp; Nanoengineering*, vol. 3, p. 16 075, Jan. 2017.

[50] S. Kim, H. Aubert, and M. M. Tentzeris, "An inkjet-printed flexible broadband coupler in substrate integrated waveguide (SIW) technology for sensing, RFID and communication applications," in *2014 IEEE MTT-S International Microwave Symposium (IMS2014)*, Jun. 2014, pp. 1–4.

[51] R. Sandhu, J. Hester, M. S. Goorsky, and J. Tice, "Printable Materials for the Realization of High Performance RF Components: Challenges and Opportunities," *International Journal of*, 2018.

[52] J. Li, Y. Zhao, H. S. Tan, Y. Guo, C.-A. Di, G. Yu, Y. Liu, M. Lin, S. H. Lim, Y. Zhou, H. Su, and B. S. Ong, "A stable solution-processed polymer semiconductor with record high-mobility for printed transistors," *Sci. Rep.*, vol. 2, p. 754, Oct. 2012.

[53] F. Schwierz, "Graphene transistors," *Nat. Nanotechnol.*, vol. 5, no. 7, pp. 487–496, Jul. 2010.

[54] K. I. Bolotin, K. J. Sikes, Z Jiang, M Klima, G Fudenberg, J Hone, P Kim, and H. L. Stormer, "Ultrahigh electron mobility in suspended graphene," *Solid State Commun.*, vol. 146, no. 9, pp. 351–355, Jun. 2008.

[55] T. Dürkop, S. A. Getty, E. Cobas, and M. S. Fuhrer, "Extraordinary Mobility in Semiconducting Carbon Nanotubes," *Nano Lett.*, vol. 4, no. 1, pp. 35–39, Jan. 2004.

[56] F. Torrisi, T. Hasan, W. Wu, Z. Sun, A. Lombardo, T. S. Kulmala, G.-W. Hsieh, S. Jung, F. Bonaccorso, P. J. Paul, D. Chu, and A. C. Ferrari, "Inkjet-printed graphene electronics," *ACS Nano*, vol. 6, no. 4, pp. 2992–3006, Apr. 2012.

[57] P. H. Lau, K. Takei, C. Wang, Y. Ju, J. Kim, Z. Yu, T. Takahashi, G. Cho, and A. Javey, "Fully printed, high performance carbon nanotube thin-film transistors on flexible substrates," *Nano Lett.*, vol. 13, no. 8, pp. 3864–3869, Aug. 2013.

[58] C. Cao, J. B. Andrews, A. Kumar, and A. D. Franklin, "Correction to Improving Contact Interfaces in Fully Printed Carbon Nanotube Thin-Film Transistors," *ACS Nano*, vol. 11, no. 4, p. 4374, Apr. 2017.

[59] M. Ha, J.-W. T. Seo, P. L. Prabhumirashi, W. Zhang, M. L. Geier, M. J. Renn, C. H. Kim, M. C. Hersam, and C. D. Frisbie, "Aerosol jet printed, low voltage, electrolyte gated carbon nanotube ring oscillators with sub-5 μs stage delays," *Nano Lett.*, vol. 13, no. 3, pp. 954–960, Mar. 2013.

[60] P. M. Grubb, H. Subbaraman, S. Park, D. Akinwande, and R. T. Chen, "Inkjet Printing of High Performance Transistors with Micron Order Chemically Set Gaps," *Sci. Rep.*, vol. 7, no. 1, p. 1202, Apr. 2017.

[61] H. Stockman, "Communication by means of reflected power," *Proceedings of the IRE*, 1948.

[62] A. Molnar, B. Lu, S. Lanzisera, B. W. Cook, and K. S. J. Pister, "An ultra-low power 900 MHz RF transceiver for wireless sensor networks," in *Custom Integrated Circuits Conference, 2004. Proceedings of the IEEE 2004*, ieeexplore.ieee.org, 2004, pp. 401–404.

[63] C. Chetvorno. (2016). Superheterodyne receiver block diagram 2, (visited on 03/15/2019).

[64] E. Kampianakis, J. Kimionis, K. Tountas, C. Konstantopoulos, E. Koutroulis, and A. Bletsas, "Wireless environmental sensor networking with analog scatter radio and timer principles," *IEEE Sensors Journal*, vol. 14, no. 10, pp. 3365–3376, 2014.

[65] V. Liu, A. Parks, V. Talla, S. Gollakota, D. Wetherall, and J. R. Smith, "Ambient Backscatter: Wireless Communication out of Thin Air," *SIGCOMM Comput. Commun. Rev.*, vol. 43, no. 4, pp. 39–50, Aug. 2013.

[66] J. D. Griffin and G. D. Durgin, "Complete link budgets for backscatter-radio and RFID systems," *IEEE Antennas and Propagation*, 2009.

[67] J. Gao, J. Siden, H Nilsson, and M. Gulliksson, "Printed humidity sensor with memory functionality for passive RFID tags," *Sensors Journal, IEEE*, vol. 13, no. 5, pp. 1824–1834, 2013.

[68] J. Virtanen, L. Ukkonen, T. Björninen, A. Z. Elsherbeni, and L. Sydanheimo, "Inkjet-printed humidity sensor for passive UHF RFID systems," *Instrumentation and Measurement, IEEE Transactions on*, vol. 60, no. 8, pp. 2768–2777, 2011.

[69] L. Yang, R. Zhang, D. Staiculescu, C. Wong, and M. M. Tentzeris, "A novel conformal RFID-enabled module utilizing inkjet-printed antennas and carbon nanotubes for gas-detection applications," *Antennas and Wireless Propagation Letters, IEEE*, vol. 8, pp. 653–656, 2009.

[70] C. Occhiuzzi, A. Rida, G. Marrocco, and M. Tentzeris, "Rfid passive gas sensor integrating carbon nanotubes," *Microwave Theory and Techniques, IEEE Transactions on*, vol. 59, no. 10, pp. 2674–2684, 2011.

[71] S. Kim, Y. Kawahara, A. Georgiadis, A. Collado, and M. M. Tentzeris, "Low-cost inkjet-printed fully passive RFID tags using metamaterial-inspired antennas for capacitive sensing applications," in *Microwave Symposium Digest (IMS), 2013 IEEE MTT-S International*, IEEE, 2013, pp. 1–4.

[72] P. V. Nikitin and K. Rao, "Antennas and propagation in UHF RFID systems," *Challenge*, vol. 22, p. 23, 2008.

[73] Y. Ling, H. Zhang, G. Gu, X. Lu, V. Kayastha, C. S. Jones, W.-S. Shih, and D. C. Janzen, "A printable CNT-based FM passive wireless sensor tag on a flexible substrate with enhanced sensitivity," *Sensors Journal, IEEE*, vol. 14, no. 4, pp. 1193–1197, 2014.

[74] A. P. Sample, D. J. Yeager, P. S. Powledge, and J. R. Smith, "Design of a passively-powered, programmable sensing platform for UHF RFID systems," in *RFID, 2007. IEEE International Conference on*, IEEE, 2007, pp. 149–156.

[75] T. Le, V. Lakafosis, Z. Lin, C. Wong, and M. Tentzeris, "Inkjet-printed graphene-based wireless gas sensor modules," in *Electronic Components and Technology Conference (ECTC), 2012 IEEE 62nd*, IEEE, 2012, pp. 1003–1008.

[76] N. Cho, S.-J. Song, S. Kim, S. Kim, and H.-J. Yoo, "A 5.1-μw UHF RFID tag chip integrated with sensors for wireless environmental monitoring," in *Solid-State Circuits Conference, 2005. ESSCIRC 2005. Proceedings of the 31st European*, IEEE, 2005, pp. 279–282.

[77] J. F. Salmerón, F. Molina-Lopez, A. Rivadeneyra, A. V. Quintero, L. F. Capitán-Vallvey, N. F. de Rooij, J. B. Ozáez, D. Briand, and A. J. Palma, "Design and development of sensing rfid tags on flexible foil compatible with epc gen 2," *IEEE Sensors Journal*, vol. 14, no. 12, pp. 4361–4371, 2014.

[78] A. Ramos, D. Girbau, A. Lazaro, A. Collado, and A. Georgiadis, "Solar-powered wireless temperature sensor based on UWB RFID with self-calibration," *Sensors Journal, IEEE*, vol. 15, no. 7, pp. 3764–3772, 2015.

[79] A. P. Sample, J. Braun, A. Parks, and J. R. Smith, "Photovoltaic enhanced UHF RFID tag antennas for dual purpose energy harvesting," in *RFID (RFID), 2011 IEEE International Conference on*, IEEE, 2011, pp. 146–153.

[80] A. Collado and A. Georgiadis, "Conformal hybrid solar and electromagnetic (em) energy harvesting rectenna," *Circuits and Systems I: Regular Papers, IEEE Transactions on*, vol. 60, no. 8, pp. 2225–2234, 2013.

[81] S. B. Darling and F. You, "The case for organic photovoltaics," *Rsc Advances*, vol. 3, no. 39, pp. 17 633–17 648, 2013.

[82] F. C. Krebs, "Fabrication and processing of polymer solar cells: A review of printing and coating techniques," *Solar energy materials and solar cells*, vol. 93, no. 4, pp. 394–412, 2009.

[83] V. Subramanian, J. M. Fréchet, P. C. Chang, D. C. Huang, J. B. Lee, S. E. Molesa, A. R. Murphy, D. R. Redinger, and S. K. Volkman, "Progress toward development of all-printed RFID tags: Materials, processes, and devices," *Proceedings of the IEEE*, vol. 93, no. 7, pp. 1330–1338, 2005.

[84] R. B. Green, "The general theory of antenna scattering," PhD thesis, The Ohio State University, 1963.

[85] R. Hansen, "Relationships between antennas as scatterers and as radiators," *Proceedings of the IEEE*, vol. 77, no. 5, pp. 659–662, 1989.

[86] S. Shrestha, M. Balachandran, M. Agarwal, V. V. Phoha, and K. Varahramyan, "A chipless RFID sensor system for cyber centric monitoring applications," *Microwave Theory and Techniques, IEEE Transactions on*, vol. 57, no. 5, pp. 1303–1309, 2009.

[87] H. Aubert, F. Chebila, M. M. Jatlaoui, T. Thai, H. Hallil, A. Traille, S. Bouaziz, A. Rifai, P. Pons, P. Menini, *et al.*, "Wireless sensing and identification of passive electromagnetic sensors based on millimetre-wave FMCW RADAR," in *IEEE RFID Technology & Applications*, 2012, 5p.

[88] D. Girbau, Á. Ramos, A. Lázaro, S. Rima, and R. Villarino, "Passive wireless temperature sensor based on time-coded UWB chipless RFID tags," *Microwave Theory and Techniques, IEEE Transactions on*, vol. 60, no. 11, pp. 3623–3632, 2012.

[89] A. Vena, L. Sydanheimo, M. M. Tentzeris, and L. Ukkonen, "A novel inkjet printed carbon nanotube-based chipless RFID sensor for gas detection," in *Microwave Conference (EuMC), 2013 European*, IEEE, 2013, pp. 9–12.

[90] E. M. Amin, M. S. Bhuiyan, N. C. Karmakar, and B. Winther-Jensen, "Development of a low cost printable chipless RFID humidity sensor," *Sensors Journal, IEEE*, vol. 14, no. 1, pp. 140–149, 2014.

[91] B. Kubina, C. Mandel, M. Schussler, M. Sazegar, and R. Jakoby, "A wireless chipless temperature sensor utilizing an orthogonal polarized backscatter scheme," in *Microwave Conference (EuMC), 2012 42nd European*, IEEE, 2012, pp. 61–64.

[92] T. Le, V. Lakafosis, M. M. Tentzeris, Z. Lin, Y. Fang, K. H. Sandhage, and C.-p. Wong, "Novel techniques for performance enhancement of inkjet-printed graphene-based thin films for wireless sensing platforms," in *2013 European Microwave Conf. (EuMC)*, IEEE, 2013, pp. 17–20.

[93] V. Dua, S. P. Surwade, S. Ammu, S. R. Agnihotra, S. Jain, K. E. Roberts, S. Park, R. S. Ruoff, and S. K. Manohar, "All-organic vapor sensor using inkjet-printed reduced graphene oxide," *Angewandte Chemie International Edition*, vol. 49, no. 12, pp. 2154–2157, 2010.

[94] P. Qi, O. Vermesh, M. Grecu, A. Javey, Q. Wang, H. Dai, S. Peng, and K. Cho, "Toward large arrays of multiplex functionalized carbon nanotube sensors for highly sensitive and selective molecular detection," *Nano Letters*, vol. 3, 2003.

[95] S. C. Davis, V. C. Sheppard, G. Begum, Y. Cai, Y. Fang, J. D. Berrigan, N. Kröger, and K. H. Sandhage, "Rapid Flow-Through Biocatalysis with High Surface Area, Enzyme-Loaded Carbon and Gold-Bearing Diatom Frustule Replicas," *Adv. Funct. Mater.*, vol. 23, no. 36, pp. 4611–4620, 2013.

[96] Y. Fang, V. W. Chen, Y. Cai, J. D. Berrigan, S. R. Marder, J. W. Perry, and K. H. Sandhage, "Biologically Enabled Syntheses of Freestanding Metallic Structures Possessing Subwavelength Pore Arrays for Extraordinary (Surface Plasmon-Mediated) Infrared Transmission," *Adv. Funct. Mater.*, vol. 22, no. 12, pp. 2550–2559, 2012.

[97] G. Wang, Y. Fang, P. Kim, A. Hayek, M. R. Weatherspoon, J. W. Perry, K. H. Sandhage, S. R. Marder, and S. C. Jones, "Layer-By-Layer Dendritic Growth of Hyperbranched Thin Films for Surface Sol–Gel Syntheses of Conformal, Functional, Nanocrystalline Oxide Coatings on Complex 3D (Bio) silica Templates," *Adv. Funct. Mater.*, vol. 19, no. 17, pp. 2768–2776, 2009.

[98] J. G. D. Hester, M. M. Tentzeris, and Y Fang, "Inkjet-printed, flexible, high performance, carbon nanomaterial based sensors for ammonia and DMMP gas detection," in *Microwave Conference (EuMC), 2015 European*, 2015, pp. 857–860.

[99] S. Heinze, J. Tersoff, R. Martel, V. Derycke, J Appenzeller, and P. Avouris, "Carbon nanotubes as Schottky barrier transistors," *Phys. Rev. Lett.*, vol. 89, no. 10, p. 106 801, 2002.

[100] J. Vitaz, A. Buerkle, M. Sallin, and K. Sarabandi, "Enhanced detection of on-metal retro-reflective tags in cluttered environments using a polarimetric technique," *Antennas and Propagation, IEEE Transactions on*, vol. 60, no. 8, pp. 3727–3735, 2012.

[101] B. Kubina, C. Mandel, M. Schüßler, M. Sazegar, and R. Jakoby, "A wireless chipless temperature sensor utilizing an orthogonal polarized backscatter scheme," in *Microwave Conference (EuMC), 2012 42nd European*, IEEE, 2012, pp. 61–64.

[102] M. Zomorrodi and N. C. Karmakar, "Novel MIMO-based technique for em-imaging of chipless RFID," in *2015 IEEE MTT-S International Microwave Symposium*, IEEE, 2015, pp. 1–4.

[103] L. C. Van Atta, "Electromagnetic reflector," pat. 2 908 002, Oct. 1959.

[104] P. Nikitin and K. Rao, "Theory and measurement of backscattering from RFID tags," *Antennas and Propagation Magazine, IEEE*, vol. 48, no. 6, pp. 212–218, 2006.

[105] D. Girbau, A. Ramos, A. Lazaro, S. Rima, and R. Villarino, "Passive wireless temperature sensor based on time-coded UWB chipless RFID tags," *Microwave Theory and Techniques, IEEE Transactions on*, vol. 60, no. 11, pp. 3623–3632, 2012.

[106] D. L. Jones and T. W. Parks, "A resolution comparison of several time-frequency representations," *IEEE Transactions on Signal Processing*, vol. 40, no. 2, pp. 413–420, 1992.

[107] S. Preradovic, I. Balbin, N. C. Karmakar, and G. F. Swiegers, "Multiresonator-based chipless RFID system for low-cost item tracking," *IEEE Transactions on Microwave Theory and Techniques*, vol. 57, no. 5, pp. 1411–1419, 2009.

[108] I. Recommendation, "Attenuation by atmospheric gases," *ITU-R P. 676*, vol. 8, 2009.

[109] J. G. Hester and M. M. Tentzeris, "Inkjet-printed van-atta reflectarray sensors: A new paradigm for long-range chipless low cost ubiquitous smart skin sensors of the internet of things," in *2016 IEEE MTT-S International Microwave Symposium*, IEEE, 2016, pp. 1–4.

[110] J. Virtanen, L. Ukkonen, T. Bjorninen, A. Elsherbeni, and L. Sydanheimo, "Inkjet-printed humidity sensor for passive UHF RFID systems," *Instrumentation and Measurement, IEEE Transactions on*, vol. 60, no. 8, pp. 2768–2777, 2011.

[111] D. Henry, J. G. Hester, H. Aubert, P. Pons, and M. M. Tentzeris, "Long range wireless interrogation of passive humidity sensors using van-atta cross-polarization effect and 3d beam scanning analysis," in *Microwave Symposium (IMS), 2017 IEEE MTT-S International*, IEEE, 2017, pp. 816–819.

[112] ——, "Long-range wireless interrogation of passive humidity sensors using van-atta cross-polarization effect and different beam scanning techniques," *IEEE Transactions on Microwave Theory and Techniques*, vol. 65, no. 12, pp. 5345–5354, 2017.

[113] M. Alhassoun, F. Amato, and G. D. Durgin, "A multi-modulation retrodirective feed network for backscatter communications," in *Personal, Indoor, and Mobile Radio Communications (PIMRC), 2017 IEEE 28th Annual International Symposium on*, IEEE, 2017, pp. 1–5.

[114] P. V. Nikitin, K. Rao, and R. D. Martinez, "Differential rcs of rfid tag," *Electronics Letters*, vol. 43, no. 8, pp. 431–432, 2007.

[115] J. D. Griffin and G. D. Durgin, "Complete link budgets for backscatter-radio and rfid systems," *IEEE Antennas and Propagation Magazine*, vol. 51, no. 2, pp. 11–25, 2009.

[116] K. Persaud and G. Dodd, "Analysis of discrimination mechanisms in the mammalian olfactory system using a model nose," *Nature*, vol. 299, no. 5881, p. 352, 1982.

[117] F. Röck, N. Barsan, and U. Weimar, "Electronic nose: Current status and future trends," *Chemical reviews*, vol. 108, no. 2, pp. 705–725, 2008.

[118] A. Strobel, C. Carlowitz, R. Wolf, F. Ellinger, and M. Vossiek, "A millimeter-wave low-power active backscatter tag for fmcw radar systems," *IEEE Transactions on Microwave Theory and Techniques*, vol. 61, no. 5, pp. 1964–1972, 2013.

[119] K. Wang, J.-F. Gu, F. Ren, and K. Wu, "A multitarget active backscattering 2-d positioning system with superresolution time series post-processing technique," *IEEE Transactions on Microwave Theory and Techniques*, vol. 65, no. 5, pp. 1751–1766, 2017.

[120] Y. Fang, M. Akbari, J. G. Hester, L. Sydänheimo, L. Ukkonen, and M. M. Tentzeris, "Sensitivity enhancement of flexible gas sensors via conversion of inkjet-printed

silver electrodes into porous gold counterparts," *Scientific reports*, vol. 7, no. 1, p. 8988, 2017.

[121] D. Henry, J. G. Hester, H. Aubert, P. Pons, and M. M. Tentzeris, "Long range wireless interrogation of passive humidity sensors using van-atta cross-polarization effect and 3d beam scanning analysis," in *2017 IEEE MTT-S International Microwave Symposium (IMS)*, IEEE, 2017, pp. 816–819.

[122] ——, "Long-range wireless interrogation of passive humidity sensors using van-atta cross-polarization effect and different beam scanning techniques," *IEEE Transactions on Microwave Theory and Techniques*, vol. 65, no. 12, pp. 5345–5354, 2017.

[123] Y. Cao, G. J. Brady, H. Gui, C. Rutherglen, M. S. Arnold, and C. Zhou, "Radio frequency transistors using aligned semiconducting carbon nanotubes with current-gain cutoff frequency and maximum oscillation frequency simultaneously greater than 70 ghz," *ACS nano*, vol. 10, no. 7, pp. 6782–6790, 2016.